NORTHWESTERN UNIVERSITY

X-Ray Standing Wave Imaging of Metal Atoms on Semiconductor and Oxide Surfaces

A DISSERTATION

SUBMITTED TO THE GRADUATE SCHOOL
IN PARTIAL FULLFILLMENT OF THE REQUIREMENTS

for the degree

DOCTOR OF PHILOSOPHY

Field of Materials Science and Engineering

By

Anthony Atilano Escuadro

EVANSTON, ILLINOIS

December 2005

ABSTRACT

X-Ray Standing Wave Imaging of Metal Atoms

on Semiconductor and Oxide Surfaces

Anthony Atilano Escuadro

The 1/3 monolayer (ML) Sn/Si(111)-($\sqrt{3}$ x $\sqrt{3}$)R30° surface structure has been extensively studied using x-ray standing waves (XSW). The summation of several XSW measured *hkl* Fourier components results in a three-dimensional, model-independent direct-space image of the Sn atomic distribution. While the image demonstrates that the Sn atoms are located at Si(111) T_4-adsorption sites, it alone cannot determine whether the Sn atomic distribution is flat or asymmetric. However, conventional XSW analysis can make this distinction, concluding that one-third of the Sn atoms are located 0.26 Å higher than the remaining two-thirds. This "one up and two down" distribution is consistent with the vertical displacements predicted by a dynamical fluctuations model. A second sample prepared in a slightly different manner exhibits the same long-range surface symmetry, but a direct space image clearly reveals that a significant fraction of the Sn atoms in the second surface have substituted for Si atoms in the bottom of the Si surface bilayer.

In addition, the electronic and atomic-scale structure of 1/2 ML V on α-Fe_2O_3(0001) as a function of the vanadium oxidation state has also been investigated using x-ray photoemission spectroscopy (XPS) and XSW direct-space imaging. The

XSW data is used to generate a direct-space image of the vanadium distribution as the surface is oxidized and reduced using atomic oxygen and hydrogen. The direct-space atomic density profile shows the average adsorption height of the V atoms is increased by 0.39 Å after the vanadium is oxidized, which suggests the oxidized vanadium is arranged in VO_4 units. The direct-space image also shows a secondary V position, which can be explained by the chemical interaction between these VO_4 units. These structural changes can be understood in light of recent XPS results, which suggest the exposure of the vanadium adlayer to atomic oxygen converts the vanadium into a V_2O_5 film and reoxidizes the hematite at the film-substrate interface. The current XSW results also suggest the oxidation of the supported vanadium is a reversible process; by exposing the submonolayer vanadia to atomic hydrogen, the oxidized vanadium is reduced and the geometry of the as-deposited surface is restored.

Approved:

_____

Professor Michael J. Bedzyk

Department of Materials Science and Engineering

Northwestern University

Evanston, Illinois

ACKNOWLEDGEMENTS

First of all, I would like to show my appreciation to the various sources of research funding that helped make the research detailed here possible. I would first like to recognize the Walter P. Murphy Fellowship that supported my studies during my initial year at Northwestern. The research I conducted in subsequent years was supported by two research centers: the Northwestern University Materials Research Science and Engineering Center (NU-MRSEC), which is funded by the National Science Foundation (NSF), and the Institute for Environmental Catalysis (IEC), which was established with funding from the NSF and is currently funded by the U.S. Department of Energy.

I would also like to acknowledge all the numerous people that have helped and encouraged me during my graduate studies here at Northwestern. First of all, I would like to acknowledge all the former members of Prof. Michael Bedzyk's research group who helped me get my start in graduate school, including Drs. Likwan Cheng, William Rodrigues, Brad Tinkham, Zhan Zhang, Joseph Libera, Don Walko, and especially Dr. John Okasinski, whose help with the UHV apparatus and direct-space imaging analysis proved invaluable for my thesis work.

I would also like to thank all the current members of the Bedzyk group, especially Dr. Yongseong Choi, Duane Goodner, and Dr. Chang-Yong Kim. It is hard to overstate the importance of the advice and assistance that Chang-Yong and Duane provided during our many beamtimes; without their time and energy, much of the work

detailed here would not have been possible. Thanks also to the DND-CAT staff for all their support during our beamtime preparations, especially Dr. Denis Keane. I also appreciate the time Prof. Laurie Marks, Prof. Mark Hersam, Prof. Peter Stair, and Prof. Paul Lyman have dedicated to serving on my thesis committee, as well as their helpful advice they have provided throughout my graduate career.

Of course, I must also express my gratitude to my thesis advisor, Prof. Bedzyk, whose guidance, expertise, and encouragement helped me to learn how to become a good scientist. I also thank him for the patience and support he has extended to me since the very beginning of my time here at Northwestern.

On a personal note, I must express my thanks to the two families that have supported me in so many ways as I progressed towards my degree: my dad Ramon, my aunt Cory, and my siblings Francis and Nicole in California, as well as my wife's family Eugene, Lina, and Eugene Jr. here in Chicago. Both of these families have helped shape me into the person I am today. I would also like to give a special thanks to my mother Maridol, who I sorely miss and will always be part of my life.

Last, but certainly not least, I cannot thank enough my wife Liza, whose understanding, sacrifice, and support throughout my graduate studies made this achievement possible. I owe her a tremendous debt, for I cannot imagine having been able to complete this accomplishment without her at my side.

TABLE OF CONTENTS

LIST OF FIGURES

LIST OF TABLES

Chapter 1: Introduction

One of the main tenets of materials science is the need to understand the relationship between the microstructure of a material and its electrical, mechanical, or chemical properties. Nowhere is this relationship more obvious than in the field of surface science, for the properties of surfaces or interfaces can undergo profound changes as surface atoms shift their positions by as little as hundredths of nanometers. Therefore, as the critical length scale of devices shrink ever smaller, there is a growing need for more precise analytical tools for probing increasingly complex atomic-scale structures. The x-ray standing wave (XSW) method is one such response to this call for more sophisticated and powerful surface science techniques.

With regards to surface and interface studies, there are two overriding advantages that the XSW method provides. First, because the XSW technique is inherently element specific, achieving the necessary surface sensitivity can be relatively straightforward since the signal collected from surface adatoms can be distinct and easily separated from the signal from the bulk. Furthermore, what separates the XSW technique from other diffraction methods is that it does not suffer from the famous phase problem of X-ray diffraction. While it has been recognized for over twenty years that the XSW technique yields information regarding both the amplitude and phase of atomic distribution functions [1], it is only recently that this advantage has been fully exploited by the direct transformation of XSW data into a real space image of an unknown atomic distribution. Because it is possible to assemble this real space image in

a model independent way, this becomes an extremely powerful technique for determining the complex atomic distributions commonly found at surfaces and interfaces.

The focus of the work presented here is the application of this unique experimental technique to two distinctly different material systems: the 1/3 monolayer (ML) of Sn on the Si(111) surface, and the oxidation and reduction of submonolayer V on the Fe_2O_3(0001) surface. These two surfaces have little in common with each other with regards to their technological applications, yet it demonstrates the versatility of the XSW method in that we can acquire atomic-scale structural information from these two disparate systems using the XSW technique.

A brief review of the Sn/Si(111) surfaces is presented in Chapter 2, which will include a short overview of the structural characteristics of both the clean Si(111) surface and the various surface reconstructions formed with the adsorption of Sn on Si(111). However, the main focus of this chapter will be on the 1/3 ML Sn/Si(111)-($\sqrt{3}$ x $\sqrt{3}$)R30° surface, which is a familiar adsorption system that has been the basis of several surface structural studies. However, while it was believed that the atomic geometry of this surface had been reasonably well-established, the recent developments regarding a controversial surface phase transition on the related Sn/Ge(111) surface and its puzzling absence on the Sn/Si(111) surface have renewed much of the scientific interest on these particular material systems. The goal of this chapter is not only to

describe these latest findings, but also convince the reader that the XSW technique can provide an important contribution to the current understanding of this unique surface behavior.

A short introduction to the V on α-Fe_2O_3(0001) surface is given in Chapter 3. In addition to reviewing the structural properties of the iron and vanadium oxides studied in this thesis, the "monolayer catalysis" effect will also be discussed. This mechanism refers to the phenomenon where the catalytic behavior of supported metal oxide layers is affected by the properties of the metal oxide support. The driving force behind this phenomenon is not well understood, which provides the motivation for much of the current research interest on supported metal oxide catalysts. Most of the surface investigations devoted to this "monolayer catalysis" effect have typically concentrated on the electronic and catalytic properties of vanadium oxide catalysts supported on TiO_2 or Al_2O_3 substrates. Therefore, this chapter will hopefully convey the uniqueness of the investigation presented here, as we have attempted to characterize both the electronic and geometric structure of vanadium layers supported on hematite, which is an important metal oxide for various catalytic processes.

A detailed description of the XSW technique is presented in Chapter 4. This chapter demonstrates how the XSW method combines both x-ray scattering and x-ray interference and results in a powerful analytical tool for the surface studies explained here. While a more conventional method of XSW analysis is reviewed in this chapter,

the highlight of this chapter is the recently developed XSW direct space imaging technique. Using a few examples that are particularly relevant to the surface studies detailed in this thesis, it is demonstrated how the simple methodology for producing the direct space images from XSW data allows the direct visualization of complex atomic distributions. Most importantly, the real space image is generated in an element-specific and model-independent way.

Both XSW experiments on the Sn/Si(111) and V/Fe_2O_3(0001) surfaces have an stringent set of requirements with regards to ultra-high vacuum (UHV) sample preparation, data collection, and x-ray conditioning. Therefore, an important component of these experiments involves the use of specialized equipment for preparing and characterizing these surfaces in an UHV environment. The design and operation of this equipment is the subject of Chapter 4. Each surface described in this document was characterized at a separate experimental station at the Advanced Photon Source, so the common capabilities and the important differences of the two experimental stations are highlighted.

In Chapter 6 the results of the XSW experiments on the 1/3 ML Sn/Si(111)-($\sqrt{3}$ x $\sqrt{3}$)R30° surface are detailed. By acquiring a considerable amount of XSW data over a large region in reciprocal space, it becomes possible to generate XSW direct space images of the Sn atomic density distribution. The atomic density map generated from the Sn/Si(111) surface reveals some structural details of the Sn

distribution, but is unable to resolve the more intriguing question of whether the $\sqrt{3}$ symmetry hides an underlying superstructure. Therefore, a traditional approach to XSW analysis is employed to extract the atomic-scale details of the Sn atomic distribution and address the controversial behavior of the Sn/Si(111) surface. The direct-space image derived from another Sn/Si(111) surface prepared under slightly different annealing conditions reveals that the Sn atomic density distribution undergoes an unexpected change. This shift involves the migration of Sn adatoms below the Si(111) surface, which is a surprising result that would have been difficult to determine using conventional XSW analysis.

The experimental results of the 1/2 ML V/Fe_2O_3(0001) system are described in Chapter 7. Once again the results of the acquired XSW data are presented in the form of Fourier-derived XSW direct space images. Instead of probing a single surface preparation as in the Sn/Si(111) study, multiple instances of the V/Fe_2O_3(0001) surface were prepared by exposing the as-deposited vanadium to oxidizing and reducing agents in the UHV chamber. Therefore, the XSW direct space images reveal in a model-independent way the evolution of the atomic-scale structure of the vanadium adatoms as a function of their oxidation state. The last chapter, Chapter 8, contains a summary of the results from the two XSW investigations presented here, as well as provides an outlook for future surface studies involving other experimental techniques or surface interactions.

Chapter 2: Background on the 1/3 ML Sn/Si(111) Surface

2.1 Introduction

This chapter will present some background information related to the atomic-scale structure and electronic behavior of the 1/3 ML Sn/Si(111) surface. In Section 2.2 the structural characteristics of the bulk-terminated Si(111)-(1 x 1) surface will be briefly reviewed. In Section 2.3 a short overview of previous structural and electronic investigations of the Sn/Si(111)-($\sqrt{3}$ x $\sqrt{3}$)R30° surface will be provided. Because interest in this particular surface is motivated by the unique observations made for the related 1/3 ML Sn/Ge(111) surface, a brief synopsis of the Sn/Ge(111) system and its controversial phase transition will be also presented.

2.2 The Si(111) Surface Structure

The atomic-scale structure of the topmost Si(111) surface layer can be described as two alternating rows of Si atoms as shown in Figure 2.1. This figure demonstrates how the two offsetting rows of Si are arranged to form the bulk-terminated Si(111) surface. This arrangement can be described by the hexagonal surface unit cell depicted in Figure 2.1; the in-plane lattice parameter of this surface unit cell is equal to the lattice spacing between the Si{110} atomic planes, or a_{surf} = 3.84 Å. The side view of the Si(111) surface shown in Figure 2.2 also highlights how the Si atoms are configured in bilayers that are laterally offset from one another. The two layers of Si atoms that make up the bilayer are separated from each other by a distance equal to 1/4 of the d_{111}

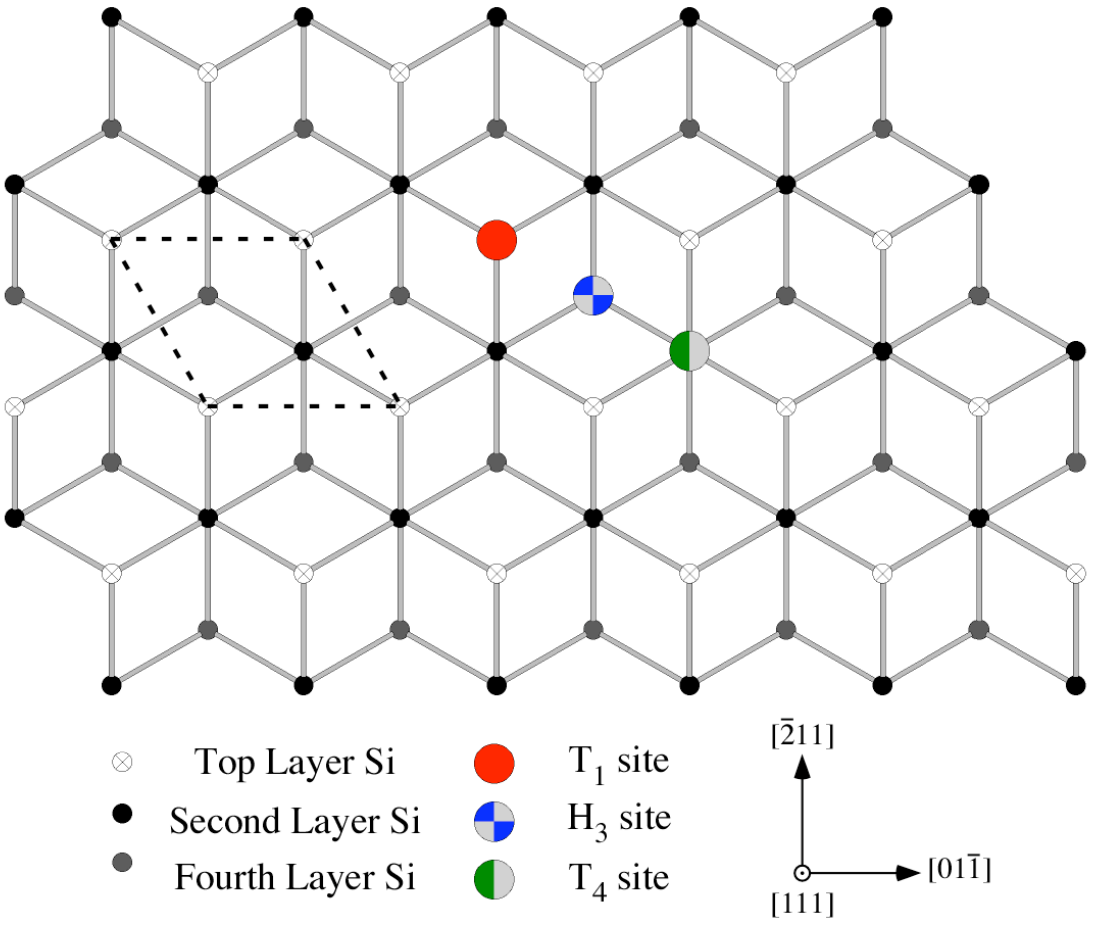

Figure 2.1: Top view of the Si(111) surface showing the three high-symmetry adsorption sites. The Si (1 x 1) surface unit cell is also outlined.

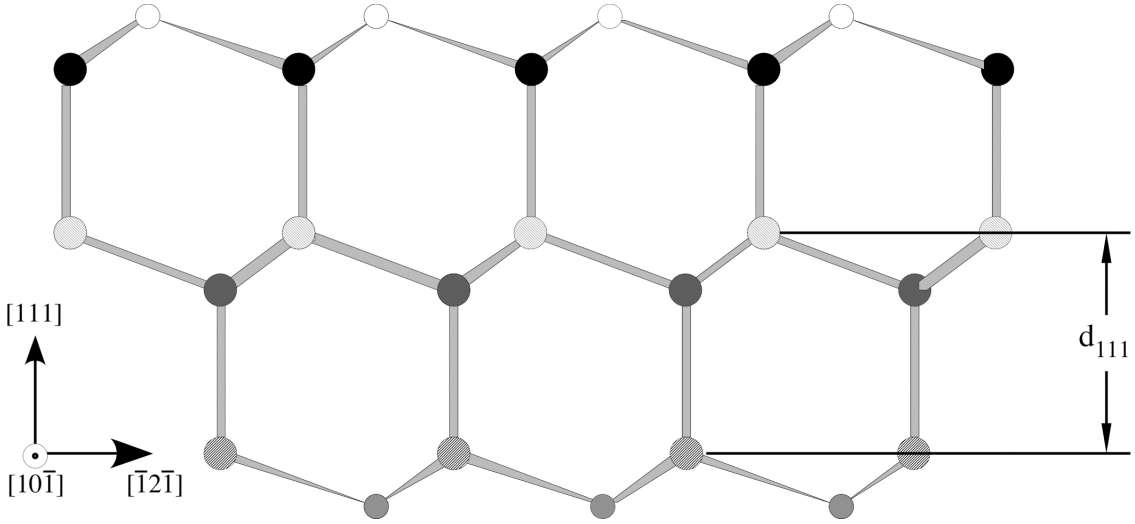

Figure 2.2: Side view projection of the Si(111) structure along the [10 $\bar{1}$] direction. The stacking of Si atoms in the [111] direction consists of Si bilayers. The lattice spacing of the (111) atomic planes (d_{111} = 3.136 Å) is also shown.

spacing, or 0.78 Å.

The hexagonal arrays of Si atoms and the resulting three-fold symmetry of the Si(111) surface defines three unique high-symmetry adsorption sites for the bulk-terminated Si(111)-(1 x 1) surface: the T_1 or "on-top" site, the H_3 site, and the T_4 site, which are all depicted in Figure 2.1. The T_1 site is situated directly above the Si atoms in the top of the Si(111) surface bilayer. Both the H_3 and T_4 sites lie equidistant from three Si atoms within the top Si(111) layer, but the T_4 site lies above the Si atom in the second Si layer while the H_3 site lies above the Si atom in the fourth Si layer. As indicated by their notation, the H_3 site has three neighboring Si atoms while the T_4 site has four Si neighbors.

The lowest energy structure for the clean Si(111) surface is the (7 x 7) surface phase. After several years of study of this surface reconstruction, the surface model that has been accepted is the dimer-adatom-stacking fault (DAS) model proposed by Takayanagi *et al* [2]. The top view of the (7 x 7) surface is shown in Figure 2.3, which shows how the structure is made up of a two-layer surface reconstruction covered by an adatom layer. The two-layer structure consists of a stacking-fault layer composed of triangular atomic units with a (1 x 1) structure and a dimer layer that surround the triangular subunits of the stacking-fault layer. In the DAS model, the (7 x 7) unit cell contains only 19 dangling bonds, which explains why this particular model has the lowest surface energy of all the proposed structures for the (7 x 7) surface [3].

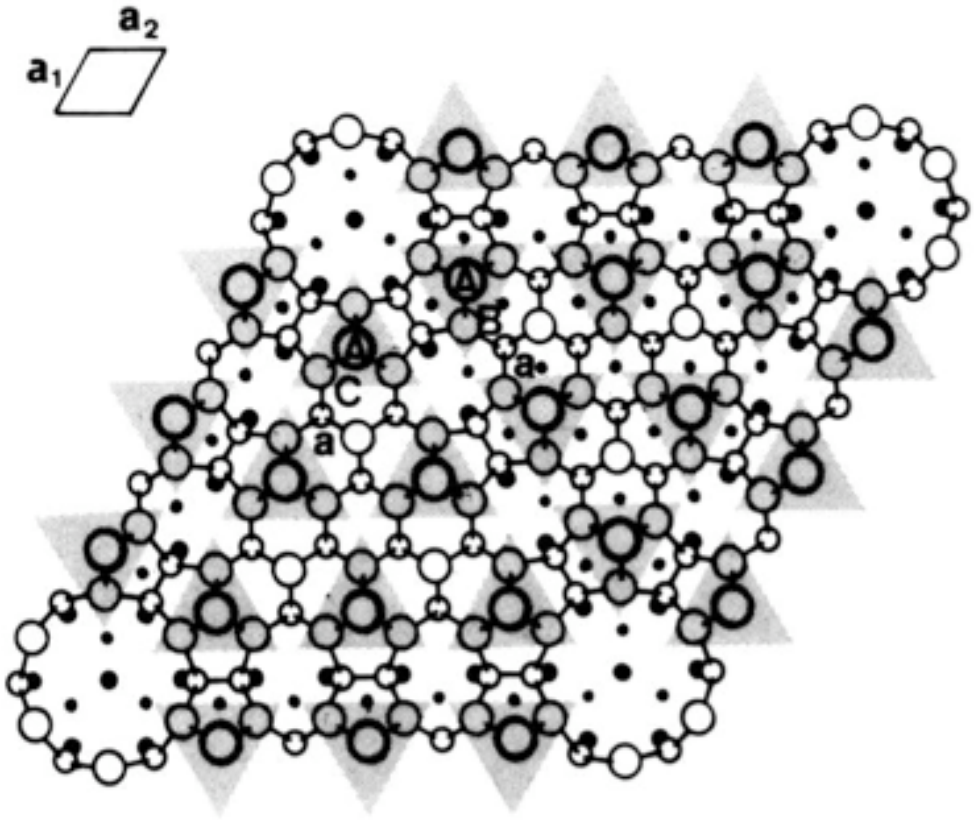

Figure 2.3: Top view of the Si(111)-(7 x 7) unit cell. The shaded triangles denote the adatom clusters that form the adatom layer. The figure is reproduced from reference [4].

2.3 Sn/Si(111) Surfaces

2.3.1 The Sn/Si(111) phase diagram

The adsorption of Sn on Si has long presented a rich opportunity for surface science, in part because of the chemical similarities between the adsorbate and the semiconductor substrate. This attribute typically results in an atomically abrupt interface between the Sn adlayer and the underlying Si substrate, which leads to the possibility for interesting and well-characterized metal/semiconductor interface studies. One such example is the study of the behavior of Sn as a surfactant for the epitaxial growth of Si on Si(111) [5].

The surface phase map of the high temperature growth of Sn on the Si(111) surface is shown in Figure 2.4. At low coverages of Sn, a (7 x 7) surface phase that is structurally similar to the clean Si(111)-(7 x 7) coexists with domains of the (√3 x √3) surface structure. At higher submonolayer coverages, the (√3 x √3)R30° phase is the predominant surface structure; further details regarding this surface phase will be given in the literature review presented in Section 2.3.3. Of note, however, is the wide area of coverage-temperature space where the (√3 x √3) surface phase is observed. This is because, unlike for the case of the (√3 x √3) surface of Sn/Ge(111), the (√3 x √3) structure can be stabilized by Si defects that populate the adatom layer and are structurally equivalent to the adsorbed Sn. Therefore, the Sn/Si(111)-(√3 x √3) surface phase in the coverage range depicted in Figure 2.4 is more accurately termed a

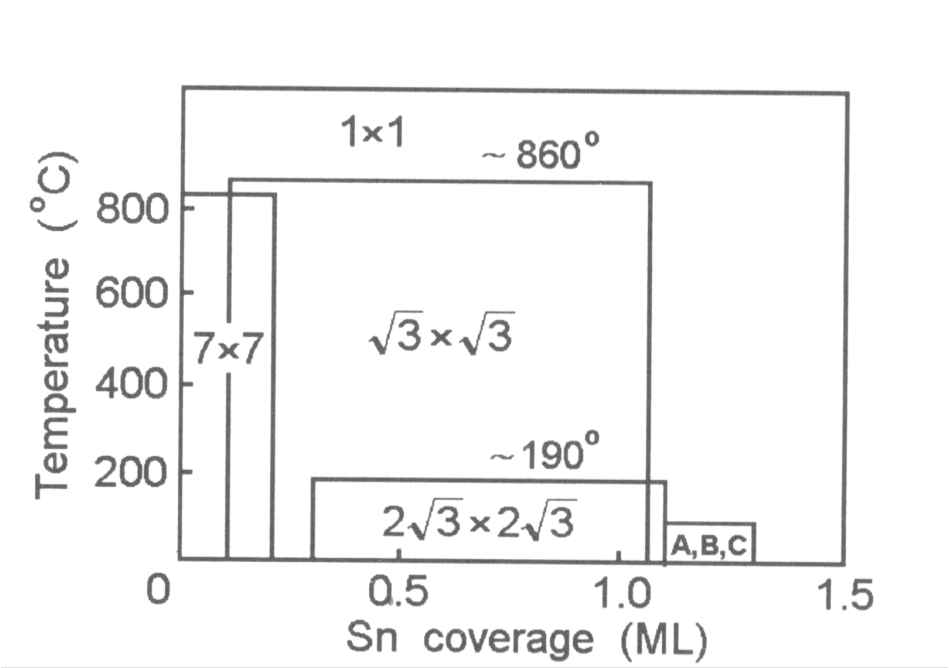

Figure 2.4: Surface phase map as determined by RHEED during the high temperature annealing of Sn deposited on the Si(111) surface. Reprinted from reference [6], Copyright 2005, with permission from Elsevier.

$Sn_{(1-x)}Si_x$/Si(111) alloy, where x=0 corresponds to the ideal α phase at 1/3 ML of Sn and x=0.5 corresponds to the γ (or mosaic) phase with equal proportions of Sn and Si adatoms.

2.3.2 Dynamical fluctuations and the 1/3 ML Sn/Ge(111) surface

The atomic scale structure of the 1/3 ML Sn/Si(111)-(√3 x √3)R30° surface (also referred to as "√3" surface) has recently attracted attention because of its structural and electronic similarities to the 1/3 ML Sn on Ge(111) surface, which also forms a √3 structure at room temperature (RT). It is generally accepted that the main feature of this atomic configuration is the adsorption of 1/3 ML of Sn at the T_4-adsorption sites, as depicted in Figure 2.5. Scanning tunneling microscopy (STM) images of the Sn/Ge(111) surface show that all the Sn adatoms at the T_4 sites appear equivalent at RT, which suggests a flat structure in which all the Sn atoms are situated at the same height above the Ge surface. However, when the Sn/Ge(111) surface is cooled below RT, it displays a change to a (3 x 3) reconstruction; the transition temperature for this phase transition is about 210 K [7]. The (3 x 3) phase is seen in STM images as a vertical "rippling" of the Sn atoms, in which one of the three Sn atoms in the (3 x 3) unit cell appear different than the other two [7]. This phase transition has been attributed to a variety of phenomena, including surface charge density waves [7, 8], Ge substitutional defects [9-13], and temperature dependent

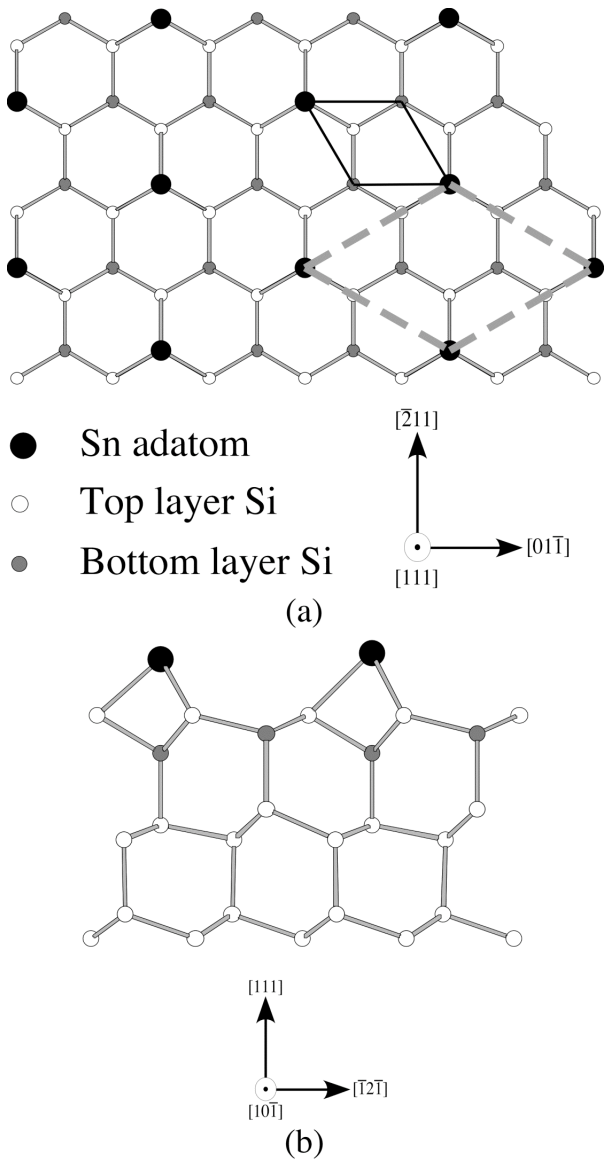

Figure 2.5: Ball-and-stick diagram of the 1/3 ML Sn/Si(111) surface. (a) Sn adatoms occupy one-third of the T_4 adsorption sites. The (1 x 1) surface unit cell is inscribed in a solid black line and the ($\sqrt{3}$ x $\sqrt{3}$)-R30° surface unit cell is inscribed in a dashed grey line. (b) Side view of the Sn/Si(111) surface. Si atoms are displaced from their bulk-like positions according to the calculated atomic displacements of Ref. [18].

dynamical fluctuations [14-17], yet there is little agreement on the dominant driving force for the low temperature (LT) (3 x 3) reconstruction.

A recent XSW study on the 1/3 ML Sn/Ge(111) surface concluded that the time-averaged Sn atomic distribution (as projected into the Ge primitive unit cell) remains constant at RT and LT despite the different surface reconstructions observed with low energy electron diffraction (LEED) and STM [19]. For the RT $\sqrt{3}$ phase, it was determined that the Sn local configuration was incompatible with the expected symmetric distribution, but instead was indicative of the asymmetric LT (3 x 3) atomic distribution. It was determined that both the RT and LT surface structure consists of three Sn atoms in a (3 x 3) unit cell occupying two distinct positions in a regular "one up, two down" configuration. This observation lends support to the dynamical fluctuations model for the Sn/Ge(111) surface, in which the three Sn atoms in the (3 x 3) unit cell rapidly fluctuate in a correlated manner between two distinct vertical positions at RT, but are frozen into a (3 x 3) configuration at LT (i.e., a 2D order-disorder phase transition). Evidence for this model is also found in core-level photoemission spectra of (3 x 3) and $\sqrt{3}$ Sn/Ge(111) [20-22], in which both surface phases display a Sn 4d line shape that is composed of two components with an intensity ratio of approximately 2:1. This Sn 4d core-level spectrum is reproduced in Figure 2.6. Valence-band photoemission studies on Sn/Ge(111) [20-22] also indicate the RT phase exhibits a surface band splitting that is unexpected for a symmetric $\sqrt{3}$ structure. These

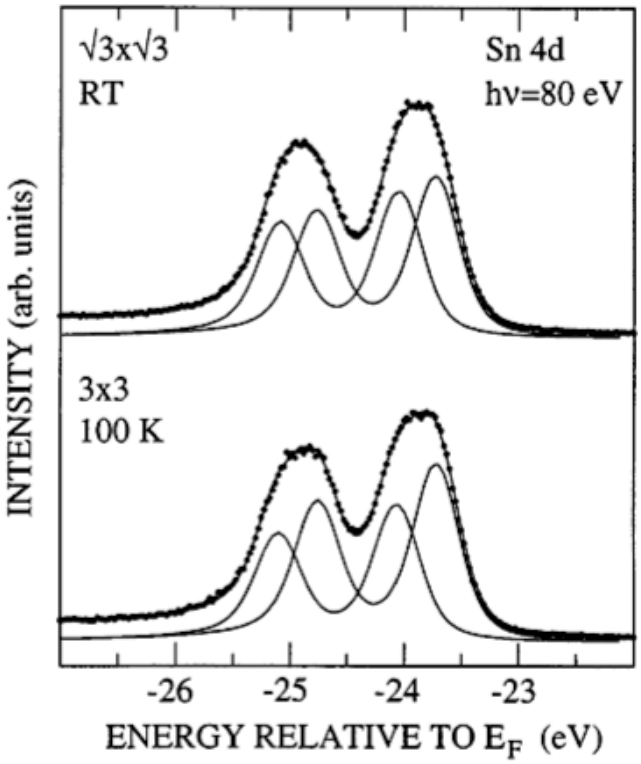

Figure 2.6: Sn 4d core-level spectra of the RT √3 and LT (3 x 3) Sn/Ge(111) surface phases. The presence of the two components suggests both surface reconstructions are composed of two types of Sn adatoms. Reprinted with permission from reference [22]. Copyright 2005 by the American Physical Society.

electronic results suggest two types of Sn are present in each of the two surface reconstructions, with each type having a unique chemical and atomic environment. The fact that both types of Sn are present at both LT and RT can be naturally explained with the dynamical fluctuations model. Further details of this dynamical fluctuations model and its implications for the related 1/3 ML Sn/Si(111) surface will be presented in Section 2.3.3.

2.3.3 The 1/3 ML Sn/Si(111)-(√3x√3)R30° surface

With regards to the 1/3 ML Sn/Si(111)-√3 surface, it was commonly accepted that Sn adatoms were situated at a single height above the Si substrate. Conway *et al.* used surface x-ray diffraction (SXRD) to determine that the adatoms are located at the T_4 adsorption sites in a single layer above the Si surface; it was also determined that the adsorption of Sn stabilize significant surface relaxations within the Si substrate [18].

However, with the increased attention devoted to the 1/3 ML Sn/Ge(111) system due to the unique temperature-dependent phase transition, the structural and electronic details of the Sn/Si(111)-√3 surface have come under increased scrutiny. Because of the similarity between Ge and Si, it is possible that the 1/3 ML Sn/Si(111) surface would also follow a similar dynamical fluctuations model. Interestingly, while the (3 x 3) phase is readily observed on the Sn/Ge(111) surface at lowered temperatures, the long-range ordering of a (3 x 3) structure on the Sn/Si(111) at LT has

not been observed via any previous structural investigations. One STM study conducted by Ottaviano *et al*. found no indications of a phase transition down to 120 K. It was pointed out that localized domains with (3 x 3) symmetry were identified centered at defect sites [23]. In an another STM and LEED investigation of 1/3 ML Sn/Si(111), Morikawa *et al*. found no evidence of any (3 x 3) symmetry at temperatures as low as 6 K and proposed the dynamical fluctuations model could not be correctly applied to the Sn/Si(111) system based on this result [24].

In one of the few structural studies of this surface, Yamanaka *et al*. used the electron standing wave (ESW) method to probe the 1/3 ML Sn/Si(111) surface; while the original ESW analysis only considered a single layer of adsorbed Sn, the ESW data was also compatible with an atomic arrangement composed of multiple Sn heights [25]. Another study investigated the structural properties of the √3 surface with full-potential linearized augmented plane wave (FLAPW) calculations and concluded the adsorbed Sn was located at a single position that was in good agreement with the earlier SXRD and ESW studies [26]. In another theoretical investigation, Profeta *et al*. used density functional theory calculations to conclude the ground state of the ideal 1/3 ML Sn/Si(111) surface presents a √3 symmetry that does exhibit distortions that lead to a (3 x 3) structure [27].

However, these results are difficult to reconcile with recent electronic structural measurements of the 1/3 ML Sn/Si(111)-√3 surface. These measurements are similar to

those conducted on the Ge(111) surface in that they suggest there are two unique types of Sn are present on the RT surface. For example, the core-level and valence band photoelectron spectra of the Sn/Si(111)-√3 surface collected by Uhrberg *et al*. [28] display many of the same features that are suggestive of the (3 x 3) structure of the Sn/Ge(111) system. This is demonstrated in Figure 2.7, which shows the two components of the core-level spectra that point to multiple site occupation and the dynamical fluctuations model. However, it should be pointed out that the smaller component appears on the low binding-energy of the large component for Sn/Si(111), which is the opposite behavior of the Sn/Ge(111) surface. A recent core-level photoemission study probed the nature of these two components by dosing the surface with electron and hole donors, which revealed the relationship between the bimodal nature of the core level spectra and two well-defined states of unlike charge [29]. In presenting these results, Davila *et al*. related their findings to the theoretical results of Ballabio *et al*., which proposed a different type of dynamical model in which different Sn structural configurations beyond a "one up, two down" arrangement are driven by strain but are obscured by thermal fluctuations [30]. It was suggested that these configurations represent a charge disproportionation phenomenon, and the Sn/Si(111) surface may represent a case of dynamical valence fluctuation, in which a classical fluctuating state or a quantum fluctuating state can exist.

Further evidence of dynamical fluctuations is found in the angle-resolved

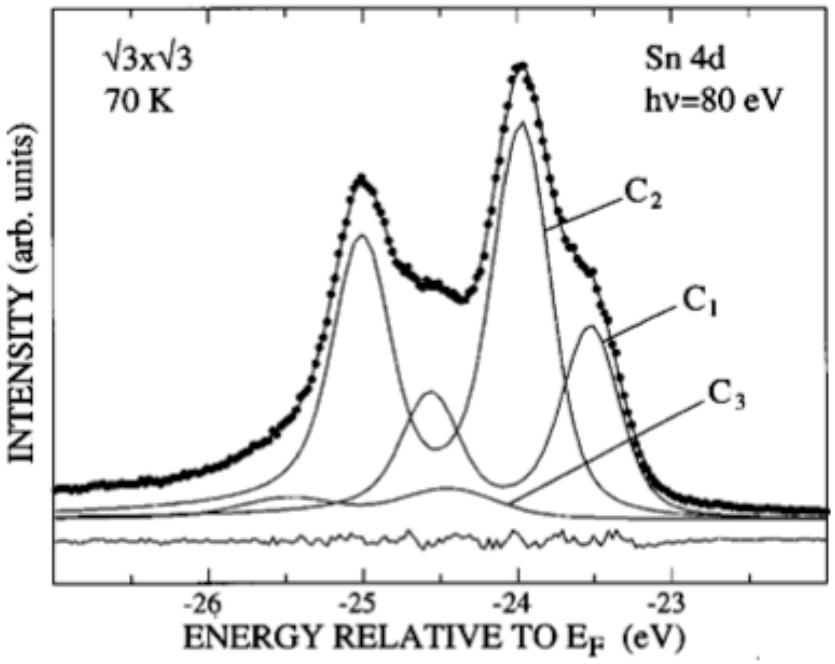

Figure 2.7: Sn 4d core-level spectra of the LT √3 Sn/Si(111) surface reconstruction. The two component spectrum appears quite similar to the core-level spectra acquired from the LT and RT Sn/Ge(111) surface. Reprinted with permission from reference [28]. Copyright 2005 by the American Physical Society.

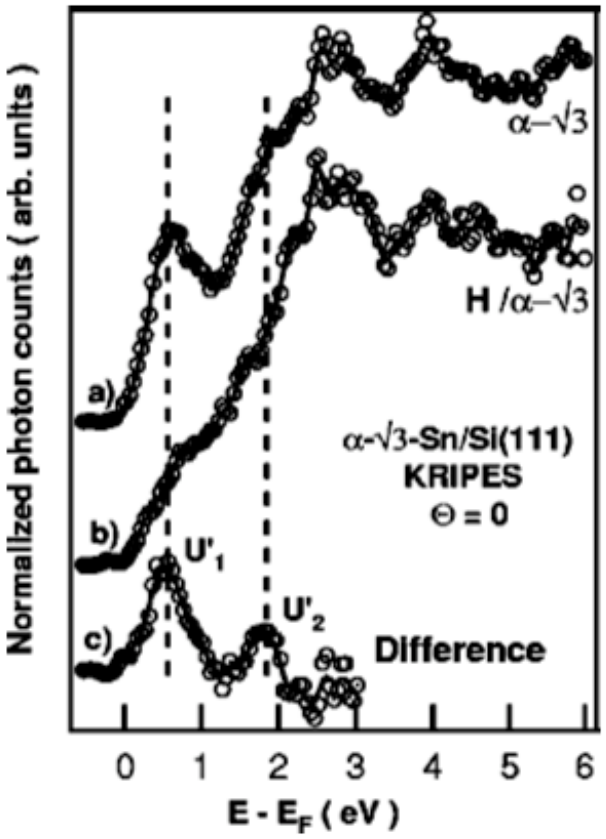

Figure 2.8: $k_{//}$-resolved inverse photoemission spectroscopy (KRIPES) spectra of the √3 Sn/Si(111) surface phase before and after exposure to atomic hydrogen. The difference curve reveals the presence of two adsorption-sensitive surface states, which suggest multiple adatom states for the RT surface. Reprinted with permission from reference [31]. Copyright 2005 by the American Physical Society.

inverse photoemission (KRIPES) results of Charrier *et al*., a portion of which is shown in Figure 2.8 [31]. The observation of the two surface states (U'_1 and U'_2 in Figure 2.8) again points to the presence of more than one type of Sn adatom in the Sn/Si(111) surface, which is in direct conflict with the STM and LEED observations presented earlier. Angle-resolved photoemission was also used to investigate the electronic character of the surface as a function of Sn coverage; this study concluded that a splitting in the surface band, which is characteristic of an underlying (3 x 3) symmetry, is present within a range of Sn coverage (0.23–0.33 ML) [32].

While the discrepancy between the existing electronic and structural results has a convincing explanation in the dynamical fluctuation model, this model as presented does not fully explain why the (3 x 3) symmetry observed by the electronic measurements has not been observed by other structural techniques, even at temperatures as low as 6 K. Using density functional theory calculations, Perez *et al*. considered the dynamical fluctuations model as the manifestation of a surface soft phonon which is stabilized by the rehybridization of the Sn dangling bond. As shown in the calculated phonon dispersion curves for the Sn/Ge(111) and Sn/Si(111) surfaces in Figure 2.9, the Sn/Ge(111) surface exhibits a zero-frequency mode at a $\bar{k}$ vector that corresponds to a (3 x 3) periodicity, so a (3 x 3) structure is expected to be a stable state for the Ge case. The Si case, however, only exhibits a minimum in the phonon dispersion curve at the K point, which represents a partial softening of the surface

phonon and explains why a static (3 x 3) periodicity is not observed for the Sn/Si(111) surface.

Despite the differences in the behavior of the surface phonons for the two surfaces, the surface structures found on Si and Ge are similar at room temperature. This observation can be understood from the energy calculations for the two surfaces presented in Figure 2.10, which shows the total energy change as a function of adatom displacement. Because of the flat energy surfaces exhibited by both surfaces, there is only a minimal energy penalty for large atomic displacements, which manifest themselves as the correlated vibrations observed at room temperature for both the Sn/Ge(111) and Sn/Si(111) surfaces [17].

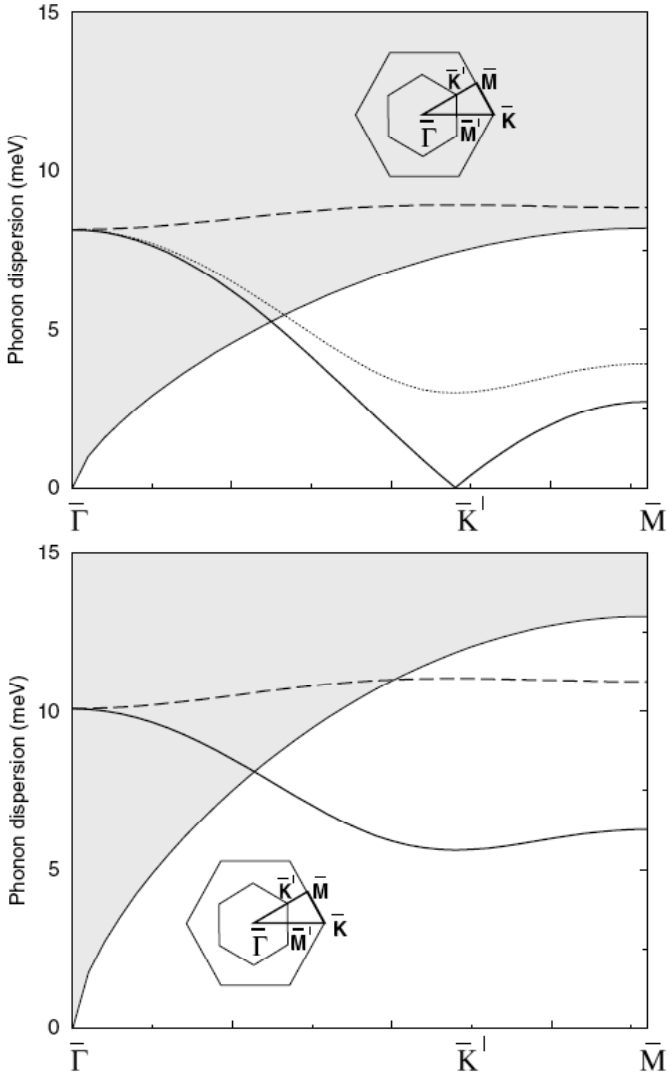

Figure 2.9: Phonon dispersion curves for the (top) Sn/Ge(111) and (bottom) Sn/Si(111) $\sqrt{3}$ surfaces. The solid lines refer to the Sn terminated surface, while the dashed lines refer to the H-saturated Sn/Ge(Si) surfaces. Shaded areas represent the projection of the corresponding phonon bulk band structure. While the Sn/Ge(111) surface exhibits a zero-frequency mode at the $\overline{K}'$ point, the Si surface only displays a minimum in the phonon dispersion curve. The dotted line for the Sn/Ge surface represents the renormalization of the frequency of the soft phonon mode at room temperature. Reprinted with permission from reference [17]. Copyright 2005 by the American Physical Society.

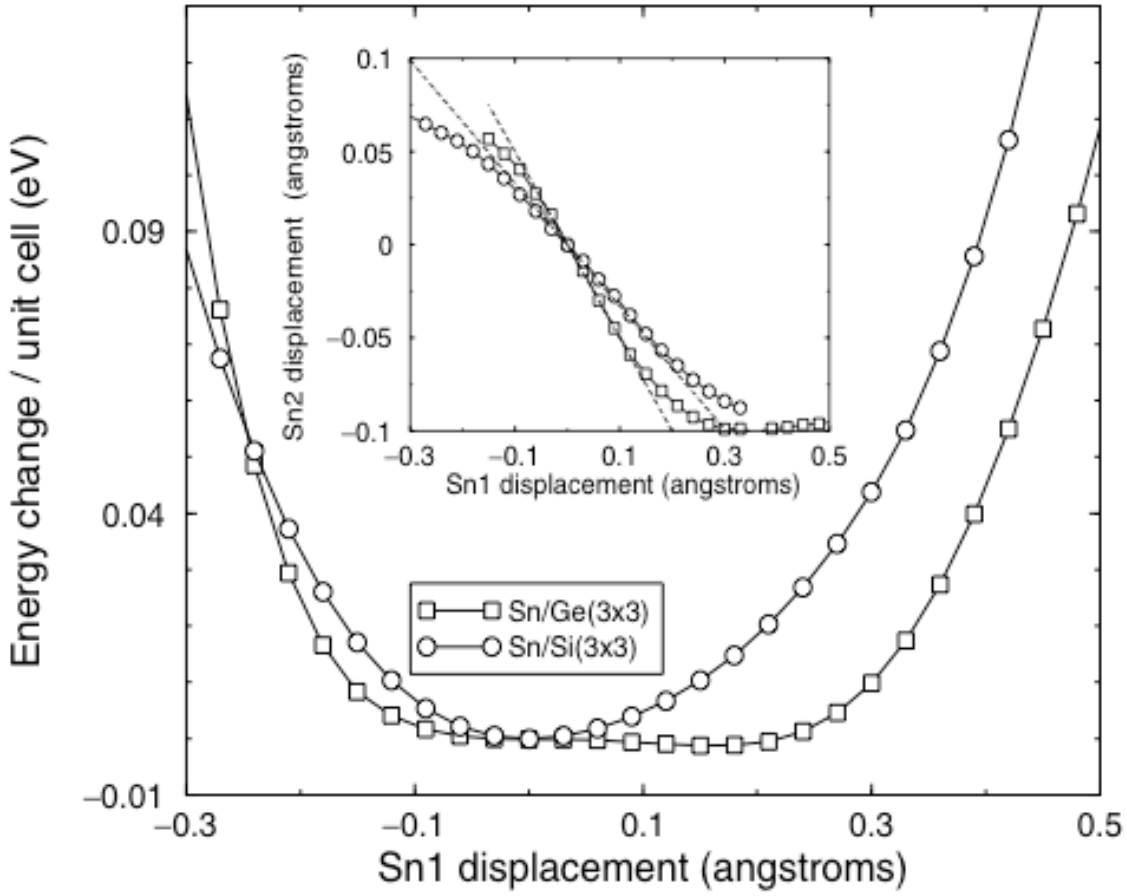

Figure 2.10: Calculated total energy of the Sn/Si and Sn/Ge surfaces as a function of the displacement of one of the Sn adatoms in the (3 x 3) surface unit cell. The inset demonstrates the relationship between the vertical displacements of the three Sn atoms in the (3 x 3) unit cell. Reprinted with permission from reference [17]. Copyright 2005 by the American Physical Society.

Chapter 3: Background on the V/α-Fe_2O_3(0001) Surface

3.1 Introduction

In this chapter a overview of the structural and electronic properties of the V/α-Fe_2O_3(0001) surface will be presented. In Section 3.2 some background material on the bulk structural characteristics of hematite will be given. The following section (Section 3.3) will detail some examples in the literature to prepare and characterize the structure of the α-Fe_2O_3(0001) surface. Later sections will focus on the catalytic role of vanadium and its assorted oxides when supported on various metal oxide substrates. A short review of the properties of some of the relevant vanadium oxides, namely V_2O_5 and V_2O_3, will be given in Section 3.4. Previous experimental investigations focused on the growth and oxidation of vanadium thin films on metal oxide supports will be reviewed in Section 3.5. While most of these studies have dealt with the case of vanadium oxide supported on the TiO_2(110) surface, our research group has recently investigated the interaction between submonolayer amounts of vanadium and the α-Fe_2O_3(0001) surface using X-ray photoelectron spectroscopy (XPS). This study will be reviewed in further detail in Section 3.6.

3.2 Crystal Structure of Bulk Fe_2O_3

Iron oxides are abundant materials that are commonly found in nature and easily synthesized in laboratory or industrial environments. Because iron oxides are so prevalent in the all aspects of the global system, from iron ore in the terrestrial

environment to precipitates in the marine environment, it is not surprising that the study of iron oxide is an important field in geology, mineralogy, and geochemistry. However, iron oxides have an important role in other disciplines as well, such as industrial and environmental chemistry, which includes catalytic research, and even medicinal and biological research. The oldest known of the iron oxides is hematite (α-Fe_2O_3), which is a stable oxide that is used as pigmentation and for magnetic recording [33]. However, it is the importance of hematite in applications of heterogeneous catalysis, photoelectrolysis, corrosion, and gas sensing that has motivated much of the effort to understand the atomic and electronic structure of the hematite surface.

Like all iron oxides, hematite consists of close packed arrays of oxygen anions in which the interstitial sites are occupied by Fe cations. In the case of hematite, the Fe and O atoms crystallize in the corundum structure (space group $R\bar{3}c$), in which the oxygen O^{2-} ions are arranged in a hexagonal close packed (hcp) array, and the interstices of the hcp array are partially filled by trivalent Fe. This arrangement forms octahedra, which consist of the central Fe^{3+} anion and the surrounding anion ligands, as shown in the depiction of the hematite hexagonal unit cell in Figure 3.1. More specifically, the Fe^{3+} cations occupy two-thirds of the sites in an ordered arrangement, where two adjacent sites in the (0001) plane are filled followed by an empty site. Because the cations are slightly larger than the octahedral sites formed by the anion close packing, the anion packing in the [0001] direction is slightly irregular and the

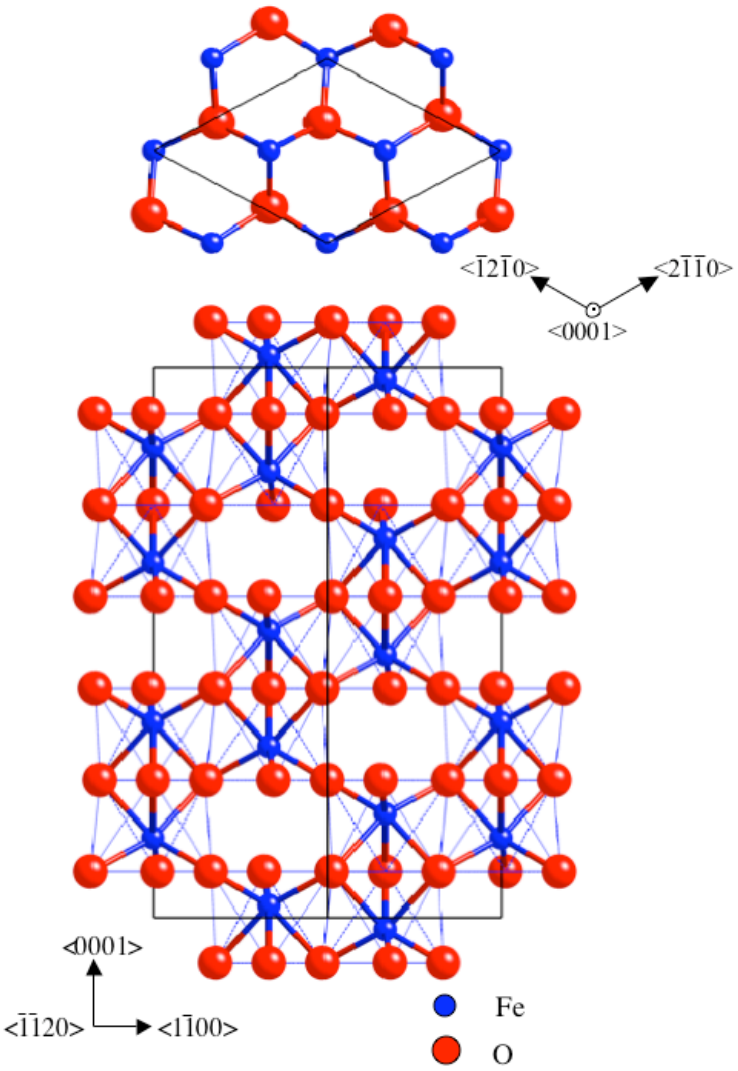

Figure 3.1: Top and side views of the α-Fe_2O_3(0001) hexagonal unit cell. The top view represents the structure of the hematite surface terminated with a complete layer of Fe cations. The side view shows the crystal structure as seen along the $<\bar{1}\ \bar{1}20>$ direction. The octahedra formed by the arrangement of Fe and O ions are also emphasized. See Appendix A for the coordinates for the Fe and O atoms.

$Fe(O)_6$ octahedra that are formed are somewhat distorted. There is also a distortion in the cation sublattice from the ideal structure, which will be briefly explained below.

Part of what distinguishes the various structures of the different iron oxides is how these octahedra are arranged with respect to each other, i.e. whether the octahedra are linked to each other by sharing corners, faces, edges, or a combination of all three. In hematite, the arrangement of vacant and occupied octahedral sites results in pairs of $Fe(O)_6$ octahedra, configured so that octahedrons in adjacent planes along the [0001] direction share a single face. The aforementioned irregularities in the oxygen anion and iron cation packing arise from this face-sharing configuration. The Fe cations contained within the octahedra are shifted away from the shared face and move along the [0001] direction closer to the unshared faces in order to minimize the electrostatic repulsion between the Fe^{3+} ions. Furthermore, the distance between O anions within the shared face is only 2.669 Å while the corresponding distance for the unshared face is 3.035 Å; this disparity results in the trigonally distorted octahedra that make up the hematite structure. The face-sharing configuration is commonly described as a "Fe-O_3-Fe" triplet, which describes the stacking sequence of the iron and oxygen planes along the [0001] direction. Within the basal plane, there is also edge sharing between the octahedron unit and three of its $Fe(O)_6$ neighbors [33].

This entire atomic configuration can be described by a hexagonal unit cell with lattice constants of a = 5.038 Å and c = 13.772 Å. As demonstrated in Figure 3.1, the

in-plane lattice parameter of the hexagonal unit cell corresponds to the interatomic distance between Fe cations within a single layer of the Fe bilayer. Six formula units comprise the nonprimitive hexagonal unit cell. The primitive bulk hematite structure can also be described using the rhombohedral unit cell, which has a lattice parameter of a_{rh} = 5.427 Å and α = 55.3°; there are two formula units per unit cell in the rhombohedral system.

3.3 Preparation and Characterization of the α-Fe_2O_3(0001) Surface

As previously mentioned, the importance of metal oxides such as hematite for heterogeneous catalysis and gas sensing applications motivates the desire to understand the atomic scale surface structure of the oxide, since much of the chemical or catalytic properties are determined by its atomic arrangement at the surface. However, obtaining the necessary structural information from a metal oxide surface such as the α-Fe_2O_3(0001) surface can be a complicated endeavor for a number of reasons.

First of all, several structural investigations of the hematite surface have found that the manner in which the surface is prepared can result in several different surface phases or morphologies. A common surface treatment for producing a clean hematite surface is Ar^+ ion sputtering; however, Kurtz *et al*. has shown that ion sputtering can preferentially remove oxygen from the surface layers and produce a reduced surface [34]. Replacing the lost surface oxygen by annealing in an oxygen environment can fill

the vacancies caused by sputtering, but the recovery of the ideal surface can be strongly dependent on the annealing conditions. One early LEED and XPS structural study of the α-Fe_2O_3(0001) surface suggested that the sputtering process transforms part of the hematite surface into a thin layer of metallic Fe^0 that lies above a thicker reduced iron oxide layer [34]. Similar investigations have suggested that it is the annealing temperature (and not the annealing environment) that primarily governs the extent of re-oxidation of the surface overlayers. It has been proposed that the choice of annealing temperature also determines whether the re-oxidized surface region consists solely of hematite or if a magnetite (Fe_3O_4) layer is produced by the removal of oxygen anions from the underlying Fe_2O_3 [35]. However, other investigations have found that after a surface layer of magnetite is formed during sputtering, annealing under an increased oxygen pressure allows the Fe_3O_4 to be reoxidized at a lower annealing temperature [36]. Finally, in an STM study, Condon *et al*. reinterpreted some of these conclusions as the result of a phenomenon called *biphase ordering*, in which islands of α-Fe_2O_3 and FeO(111) coexist on the hematite surface and form an extended superlattice [37, 38]. STM images of this unique overlayer structure are shown in Figure 3.2.

An extensive surface x-ray diffraction (SXRD) investigation on the α-Fe_2O_3(0001) surface encountered all these aforementioned iron oxide phases as the oxygen-deficient hematite surface was recovered to the stoichiometric (1 x 1) surface [39]. Unlike the electron-based surface techniques that probe only the first few atomic

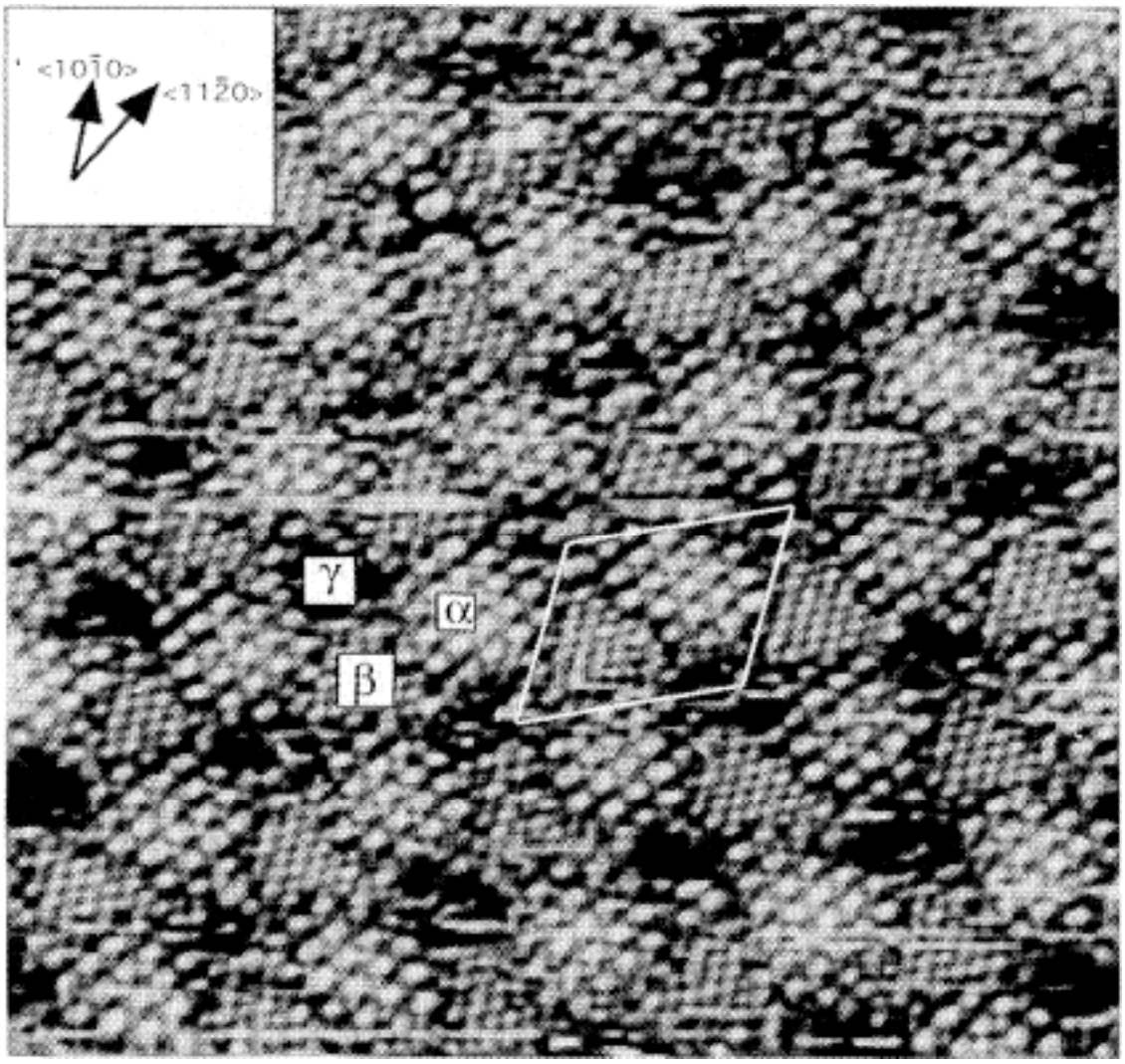

Figure 3.2: A 200 Å x 200 Å STM image of biphase ordering on the α-Fe_2O_3(0001) surface. The overlayer consists of α-Fe_2O_3(0001) and FeO(111) islands arranged to form a periodic superstructure. Reprinted with permission from reference [38]. Copyright 2005 by the American Physical Society.

layers of the surface, the x-ray scattering provides structural information from both the surface and subsurface regions. It was determined that after annealing the reduced surface in a molecular oxygen environment, the uppermost surface layers can be recovered to the stoichiometric Fe_2O_3 phase, but a remnant magnetite layer remains below the recovered oxide surface. By slightly increasing the oxygen annealing temperature (from 1008K to 1018K in this particular study), the subsurface magnetite can be converted to hematite, but the previously stoichiometric surface is simultaneously transformed into the non-stoichiometric biphase ordered surface. The topmost biphase layer can finally be converted to Fe_2O_3 by annealing in an atomic oxygen environment. This elaborate surface history is a telling example of some of the complexities that can arise when preparing and characterizing the stoichiometric α-Fe_2O_3(0001) surface.

Furthermore, even if the stoichiometric structure can be recovered from the oxygen deficient surface using oxygen annealing, the question of what is the chemical composition of the α-Fe_2O_3(0001) surface remains. Because of the "Fe-O_3-Fe" stacking sequence of the bulk hematite structure, it is possible that the α-Fe_2O_3(0001) surface can consist of a terminal layer of either Fe cations or O anions. In addition, the hematite surface can be expected to undergo significant atomic relaxations, which are in part driven by the tendency of the surface cations to increase their oxygen coordination. A detailed theoretical study employing a variety of periodic slab models and

computational methods found a large relaxation effect for the two outermost surface layers of a Fe-terminated α-Fe_2O_3(0001) surface. These substantial relaxations were attributed to the reduced coordination of the surface atoms [40]. In one spin-density functional theory (DFT) study, Wang *et al*. calculated the surface energies of various α-Fe_2O_3(0001) surface terminations as a function of the oxygen chemical potential. From the results of these calculations (which are summarized in Figure 3.3), it was determined that both a Fe-terminated (Fe-O_3-Fe) and an O-terminated (O_3-Fe-Fe) surface can be stabilized if they were accompanied with significant atomic interlayer relaxations. The presence of both surface terminations was observed using STM [41]. Another STM study [42] also observed the significant dependence of the hematite surface structure on the ambient oxygen pressure detailed in Ref. [41]. In another DFT investigation of the α-Fe_2O_3(0001) surface, several Fe- and O-terminated hematite surfaces were explored, including an additional surface phase involving a single O atom bonded on top of a reactive surface Fe atom; this structure stabilizes as the surface is allowed to relax in an oxygen-rich environment, as shown in the calculated surface phase energy plot shown in Figure 3.4 [43].

However, these results were somewhat disputed by Chambers *et al*. in a XPD and STM investigation of α-Fe_2O_3(0001) surfaces grown by oxygen-plasma-assisted molecular beam epitaxy. This study suggested that the Fe-terminated surface is the most stable surface even under highly-oxidizing conditions [44]. These experimental

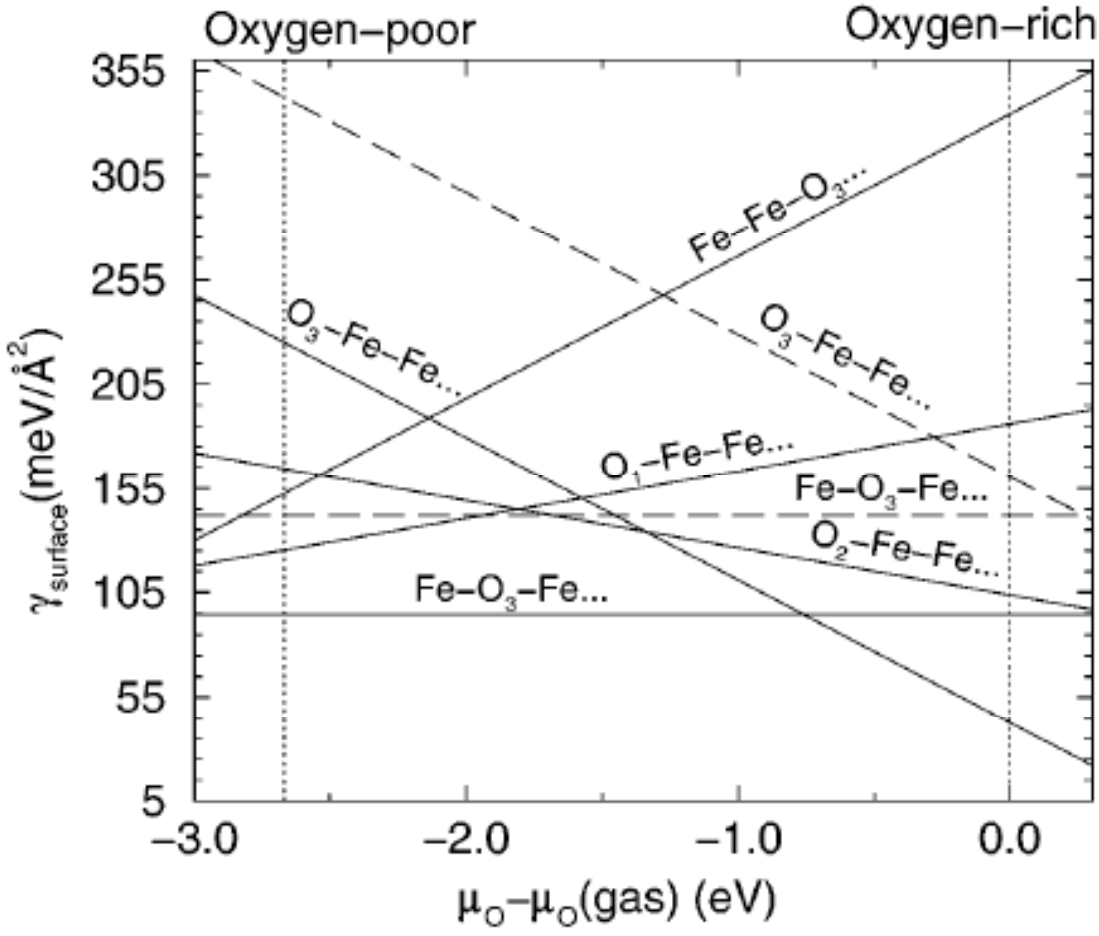

Figure 3.3: Calculated surface energies of various α-Fe_2O_3(0001) surface terminations as a function of the chemical potential per oxygen atom of molecular O_2. The solid lines represent relaxed geometries, while the dashed lines represent unrelaxed surfaces. As the diagram shows, it was predicted a relaxed oxygen termination would be stable in oxygen-rich conditions. Reprinted with permission from reference [41]. Copyright 2005 by the American Physical Society.

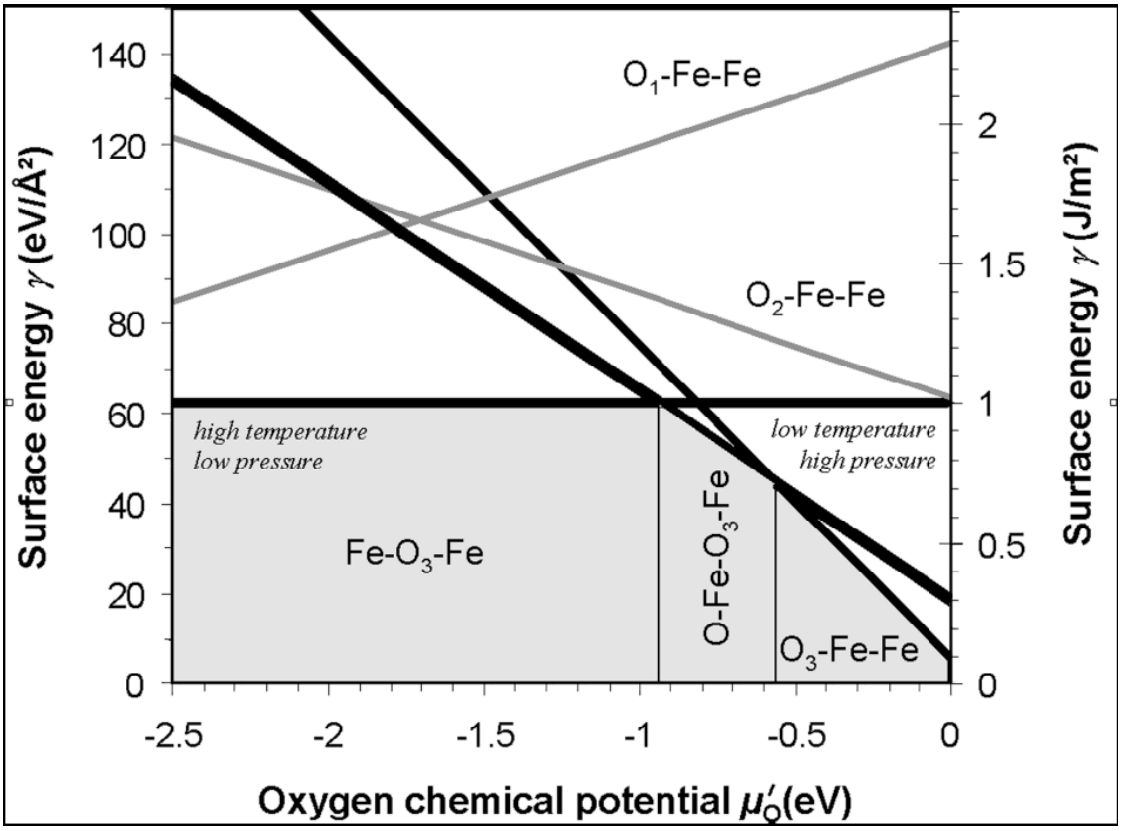

Figure 3.4: Calculated surface energies of various α-Fe_2O_3(0001) surface terminations as a function of oxygen chemical potential. The full oxygen termination (O_3-Fe-Fe) is thermodynamically stable at high oxygen potentials; the ferrate-like surface termination (O-Fe-O_3-Fe) is stable at intermediate oxygen potentials. Reprinted with permission from reference [43]. Copyright 2005 by the American Physical Society.

results were supported by an *ab initio* theoretical study, which included electron correlation effects within a density functional description. By including the strong correlation effects, it was determined that a Fe-terminated surface is the most stable surface over the allowable range of oxygen chemical potentials; the proposed surface model consists of a partially occupied Fe layer in which half of the octahedral sites are vacant [45]. An earlier X-ray photoelectron diffraction (XPD) experiment also found this particular structure to be the most stable surface phase and found no evidence of a possible O-termination [46]. The authors of this study suggested that since the partially occupied Fe termination layer fully autocompensates the hematite surface due to charge transfer from the Fe dangling bonds to the O dangling bonds, it is not surprising that the Fe-termination surface model provided the best fit to the PED spectra [47].

Finally, for some catalytic investigations the presence of surface point defects may be desirable, since oxygen vacancies can result in a redistribution of charge and a reduction of surface cations, which can help promote the adsorption and dissociation of foreign molecules. A surplus of cations in the form of Fe interstitials is another form of non-stoichiometry that can also contribute to the catalytic activity. Therefore, there is a need to characterize non-ideal hematite surfaces in order to more accurately model real-world catalytic processes. In a theoretical study of the defect chemistry of the α-Fe_2O_3(0001) surface, Warschkow *et al*. found that at the hematite surface, the energy required to form an oxygen vacancy is markedly smaller than in the bulk [48].

Furthermore, the same investigation determined a lowering of some of the transition barriers to oxygen vacancy migration within the uppermost oxygen layers near the hematite surface. However, there are few experimental studies on the formation of defects and their effect on the properties of the α-Fe_2O_3(0001) surface.

3.4 Overview of the Oxides of Vanadium

The study of supported vanadium-based oxides and their interaction with the supporting material represents one of the most active fields of catalytic research. This reflects the significance of vanadium oxide-based catalysts in many important industrial processes, such as the production of sulfuric acid and phthalic anhydride, and in the reduction of environmental byproducts, such as the selective reduction of nitrogen oxides from the flue gas of power plants [49]. Two reasons have been mentioned for the importance of vanadium for metal oxide catalysis: the variety of oxidation states (from +2 to +5) and the assortment of structural geometries that are available for vanadium oxides. Because of the variability of atomic arrangements that are present in vanadium oxides, the surface oxygen anions can have a number of possible coordination geometries, which in turn has a strong effect on the oxides' catalytic properties.

When employed as a catalyst, the vanadium oxide is typically distributed on a supporting material, either by impregnation, adsorption from solution, a deposition

method such as chemical vapor deposition, or by co-precipitation [50]. The original intent of using a support material was to enhance the catalytic activity of the vanadium oxide by increasing its mechanical strength, surface area, thermal stability, and endurance. However, recent studies have demonstrated that the catalytic properties of supported metal oxides, especially vanadium oxides, are enhanced by the properties of the support itself. This phenomenon has been termed the "metal oxide-support" or "monolayer catalysis" effect; Bond *et al.*, Weckhuysen *et al.*, and Surnev *et al.*, in preparing extensive reviews of this mechanism, have focused on the role of supported vanadium oxides. While these reviews examine the properties of both the principal vanadium oxides and mixed valency oxides in many different molecular configurations (such as an isolated vanadium oxide species, two-dimensional vanadium oxide chains, or three-dimensional crystals of vanadium oxide), this thesis will present only a brief overview of the pentoxide V_2O_5 and the sesquioxide V_2O_3 as they have been studied in various supported metal oxide investigations [49-51].

The geometric structure of V_2O_5 can be described as edge-sharing units of VO_5 that form double chains along the b-direction. The VO_5 oxide units form square pyramids, but because the chains are connected at the corners and stacked on top of each other in the c-direction, the vanadium oxide unit is actually a distorted VO_6 octahedron. There are three distinct V–O bond distances within this octahedron. The V=O double bond along the c-direction is 1.58 Å in length, while the V–O bond

directly opposite the double bond is 2.79 Å. The four V–O bonds involving the bridging oxygens in the basal plane have a length of 1.83 Å [49]. A ball-and-stick model of the orthorhombic unit cell of V_2O_5 is shown in Figure 3.5. As for the electronic state of the pentoxide, V_2O_5 has a formal oxidation state of +5 and has the d^0 electronic configuration. Therefore, V_2O_5 cannot gain any additional oxygen and would not be expected to be an active catalyst in its stoichiometric state [52]. However, supported layers of V_2O_5 can be activated with high temperature reducing environments in order to produce a variety of surface oxidation states; this enables the vanadium oxide to participate in subsequent catalytic reactions. The material supporting the vanadium oxide and the reducing species can also influence the distribution of vanadium oxidation states and oxygen coordination geometries that are present after reduction [49].

Unlike V_2O_5, bulk V_2O_3 (which crystallizes in the corundum structure, similar to α-Fe_2O_3) or its clean surfaces have received much less attention with regards to their catalytic properties. However, there are several surface investigations of vanadia deposition on metal oxides such as α-Al_2O_3 or TiO_2 where it was determined the deposited vanadium oxide layer has the characteristics of V_2O_3. Some examples of such surface studies will be given in the following section.

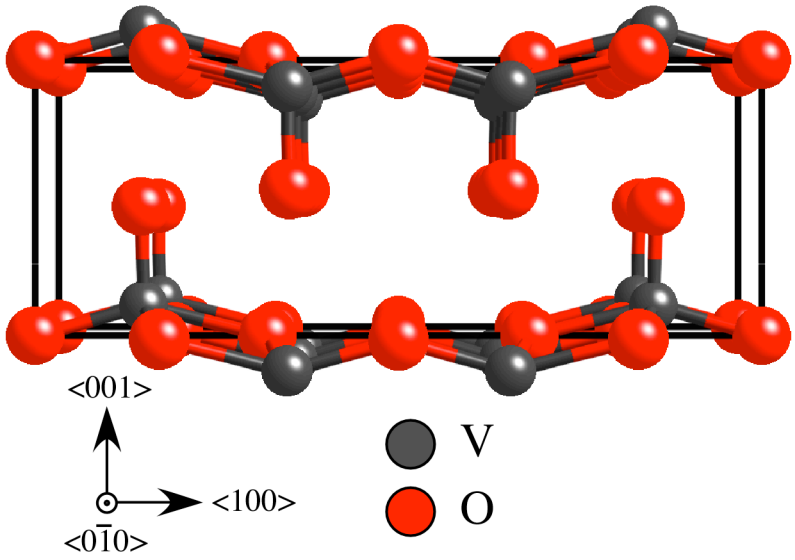

Figure 3.5: Orthorhombic unit cell of the bulk V_2O_5 crystal structure. The unit cell shown consists of two V_2O_5 layers that are weakly bound to each other. The crystallographic data used to produce the figure originates from reference [53].

3.5 Vanadium Oxide Films Supported on Oxide Substrates

When a transition metal such as vanadium is deposited on a metal oxide substrate, there can be a complex interaction between the adsorbed metal and the oxide substrate. Because of the various oxidation states that are available to transition metals, especially in the case of vanadium, the transition metal can assume any of several electronic configurations depending on the availability of charge carriers in the substrate and the magnitude of the surface potential at the adsorption site [52]. The characteristics of the bonding between metal and metal oxide can be complicated as well due to the partially-filled and localized d orbitals that govern the chemistry of the adsorbed transition metal; in addition to an ionic component of the bonding due to charge transfer between the adsorbate and the substrate, there may also be some direct overlap between the d orbitals of the two atomic species that leads to a metallic type of chemical bond [52]. Finally, the adsorption of the metal can disturb the metal oxide surface in a significant way by reacting with the lattice oxygen. Vanadium, in particular, has a relatively large oxygen affinity (based on its heat of formation of the stable vanadium oxide), so it would be expected that adsorbed vanadium could be particularly effective in reducing a hematite substrate and forming a surface layer of vanadium oxide.

While the focus of this thesis is the interaction of submonolayer amounts of vanadium and the α-Fe_2O_3(0001) surface, there has been a wealth of surface

investigations on the structural, electronic, and catalytic properties of vanadium oxide films on TiO_2(110) and, to a lesser extent, α-Al_2O_3(0001). This overview will present some of the most recent results of various vanadium oxides at the TiO_2(110) surface; because α-Al_2O_3 is isostructural with hematite, it will be useful to review the findings of the surface studies of vanadium oxide on alumina as well.

In one early investigation of the interaction of vanadium and vanadium oxide with TiO_2(110), Zhang *et al*. recognized that because of the strong oxygen affinity of both V and Ti, the competition between the two transition metals for the lattice O^{2-} ions would result in an interesting system [54]. When vanadium is deposited on the stoichiometric TiO_2(110) surface at submonolayer coverages in ultra-high vacuum (UHV) conditions, Zhang *et al*. found an immediate reduction of the titania surface as charge is transferred from Ti^{4+} cations to V adatoms to form a thin, disordered Ti–O–V layer. This strong interaction between vanadium and the substrate was not present when deposited on reduced TiO_2(110) surfaces. Further vanadium deposition beyond 1 monolayer (ML) produced a metallic V layer above the disordered Ti–O–V compound. In a later surface investigation also conducted in UHV, Biener *et al*. determined the TiO_2 substrate is reduced upon vanadium deposition, and both V^{2+} and V^{3+} as well as Ti^{3+} cations are produced. This charge-transfer process is not limited to the initial surface layers; rather, subsurface lattice oxygen cations migrate toward and partially oxidize the vanadium overlayer [55].

When vanadium is deposited in a molecular oxygen environment (1 x 10^{-7} Torr) on stoichiometric TiO_2(110), a weakly interacting and disordered vanadium oxide forms with a composition similar to V_2O_3 or VO_2 [54]. In a separate XPD study of room temperature (RT) deposition of V followed by a mild annealing, Sambi *et al.* proposed that the adsorbed V atoms occupy a well-defined atomic site that corresponded to a Ti bulk-like substitutional site within the first surface layer. There was no diffraction evidence of diffusion of the vanadium before the initial surface layer. It was suggested the mild annealing provided the necessary energy for bulk oxygen to diffuse to the TiO_2 surface and fully oxidize the surface Ti and V atoms [56]. The same researchers also reported on the growth of several monolayers of epitaxial VO_2 on the TiO_2(110) surface. The VO_2 oxide layer was prepared with successive depositions of vanadium; after each deposition step, the TiO_2 surface was annealed in an oxygen environment. This growth process was described as "deposition under thermodynamic control," in which the post-deposition annealing process was intended to enhance the order and oxidation of the surface. It was determined that the resulting vanadium oxide layer was well-ordered and pseudomorphic to the TiO_2(110) substrate [57, 58].

In another extensive surface investigation employing LEED, Auger electron spectroscopy (AES), XPS, and near edge X-ray absorption fine structure spectroscopy (NEXAFS), Biener *et al.* proposed that if vanadium is deposited on the TiO_2 substrate

at RT in an oxygen ambient, the vanadium does not reduce the TiO_2 surface. Instead, it is suggested that a disordered layer of V_2O_3 forms via a simultaneous growth mode, in which the vanadia grow as islands that eventually combine to form the complete V_2O_3 layer [59]. Sambi *et al*. conducted a similar surface study using XPS, AES, and XPD and determined that while the vanadium oxide grown in an oxygen environment may have an electronic structure typical of V_2O_3, the atomic-scale structure of the oxide is actually isomorphic to the rutile lattice of the TiO_2 substrate below [57, 60]. The authors suggested that the unique way the thin layers of vanadia adopted the underlying structure of the TiO_2 substrate might have a role in the oxide's catalytic activity. Instead of performing the vanadium deposition at RT, Guo *et al*. attempted to form a vanadium oxide thin film by depositing vanadium on the TiO_2(110) surface at 570K in an oxygen ambient [61]. This surface study also observed the formation of a vanadium oxide layer characteristic of V_2O_3 when the vanadium coverage was above one monolayer equivalent (MLE). However, at lower vanadium coverages, both core-level XPS spectra and electron energy loss spectra (EELS) suggested that both V^{3+} and V^{4+} were present at the vanadia-titania interface.

Finally, there have been some successful efforts to prepare thin layers of V_2O_5 supported on TiO_2 by codosing the titania surface with $VOCl_3$ and water vapor at RT, then annealing the vanadium-covered surface in an oxygen environment (2×10^{-6} Torr). At submonolayer coverages, the vanadia layers consisted of vanadium cations with a

+5 oxidation state, while at larger coverages some V^{4+} cations are present [62]. The resulting V_2O_5 adlayers could be repeatedly reduced to lower oxidation states and reoxidized with exposure to the appropriate gaseous species [63]; the vanadium 5+ oxidation state also resulted in the vanadia surface exhibiting an increased catalytic activity for the partial oxidation of methanol to formaldehyde, especially at a coverage of one monolayer [62]. Wong *et al*. also prepared V_2O_5 films on the TiO_2(110) surface using vapor-deposited vanadium and oxidizing at a relatively high oxygen partial pressure (1×10^{-3} Torr of O_2) [64]. The catalytic properties of these V_2O_5 films are somewhat different than the properties of the films generated through the hydrolysis of $VOCl_3$; it was proposed that these variations might result from differences in the atomic-scale structure of the two vanadia films.

The aforementioned surface studies have demonstrated the strong interaction between vanadium and the TiO_2(110) support; the interaction with vanadium and the α-Al_2O_3(0001) surface has also garnered its share of scientific attention. Because α-Al_2O_3 and TiO_2 are quite different with regards to their crystal structure and their reducibility, it might be expected that the vanadium oxides supported on these two metal oxides would be somewhat dissimilar. For example, Bäumer *et al*. explored the growth and reactivity of submonolayer vanadium deposited in UHV on a thin Al_2O_3 film; their XPS and NEXAFS results demonstrated that that the electronic structure of the vanadium deposits at low vanadium coverage ($\Theta < 0.12$ ML) did not correspond to the electronic

structure of a principal oxide such as V_2O_3 or VO_2. The oxidized vanadium had instead acquired a formal oxidation state between +1 and +2. Interestingly, with further vanadium deposition in an oxygen atmosphere (7×10^{-7} Torr of O_2), the surface vanadium seems to promote the unexpected growth of the thin alumina film [65]. However, Biener *et al.*, using XPS and NEXAFS, also attempted to determine the electronic state of vanadium deposited on α-Al_2O_3(0001) at RT in an oxygen ambient. The results for their investigation of vanadium deposition on alumina were quite similar to those derived from a titania support; namely, a vanadium oxide similar to V_2O_3 forms through a simultaneous multilayer growth mode [66, 67]. The NEXAFS results also suggest that the local atomic arrangement of the vanadium oxide layer consists of vanadium cations with an octahedral coordination with its oxygen neighbors. While this particular study clearly shows evidence of the formation of a vanadium oxide, the oxidation of the deposited vanadium was not accompanied by a reduction of the aluminum cations at the α-Al_2O_3 surface. Therefore, it was suggested that the interaction between the vanadium and aluminum atoms at the oxide interface involved a subtle redistribution of charge instead of change in formal oxidation state [68].

3.6 Vanadium and Vanadium Oxides Supported on α-Fe_2O_3(0001)

As the examples described above clearly demonstrate, there is a healthy scientific interest in the behavior of submonolayer of vanadium and vanadium oxides

when supported on metal oxide substrates. However, to our knowledge, there are no published experimental or theoretical studies that have focused on the interaction between vanadium and an underlying iron oxide support. Therefore, as an accompaniment to the X-ray standing wave investigation on the V/α-Fe_2O_3(0001) system that will be detailed in Chapter 7, our research group conducted an extensive XPS study on the electronic structure of vanadium and vanadia films on the α-Fe_2O_3(0001) surface [69]. This study has provided insight into the chemical interactions that arise between the adsorbed vanadium and the hematite surface. We can then associate these changes in the electronic structure with any changes in the geometric structure that the XSW experiment reveals.

In this investigation, a clean α-Fe_2O_3(0001) surface was prepared by oxygen annealing at 723 K in a stream of atomic oxygen gas. After annealing the Fe_2O_3 for 30 minutes, the surface displayed a sharp (1 x 1) LEED pattern, and no amount of carbon contamination could be detected with XPS. Successive amounts of vanadium were then deposited on the clean α-Fe_2O_3(0001) surface at RT, and XPS spectra were collected after each vanadium dose in order to measure any changes in the electronic state of the surface and in the substrate work function. A total of 8 ML of vanadium was deposited on the sample surface, forming a thick vanadium film. This film was then oxidized by exposure to atomic oxygen at RT, and XPS measurements of the vanadia film were performed.

As shown in Figure 3.6, the work function evolves in four distinct stages as vanadium is deposited on the hematite surface. The initial doses of vanadium cause a rapid decrease of the substrate work function, as electrons are transferred from the vanadium adsorbates to the underlying Fe_2O_3 substrate. As more vanadium is deposited, there is a gradual increase in the work function. This is due to the enhanced interaction between vanadium-induced dipoles, which produce a depolarization of the dipole moments. Finally, as the vanadium layers begins to form a thick film, the work function approaches a value of 3.95 eV (which is close to the work function of bulk vanadium metal [4.10-4.65 eV]) before a small decrease in the work function occurs.

The XPS spectra shown in Figure 3.7 also reveal how the vanadium and iron electronic structure changes as vanadium interacts with the Fe_2O_3(0001) surface. The Fe 2p XPS spectrum displays a shift in the main Fe 2p peak position, as well as in the position of the satellite features. These shifts towards higher binding energy suggest the hematite surface layer is gradually being converted to Fe^{2+} as charge is transferred from the deposited vanadium to the Fe^{3+} surface cations. This transfer of electrons is also manifested in the V 2p XPS spectra, as the V $2p_{3/2}$ peak position (515.7 eV) at low vanadium coverage is close to the binding energy of vanadium in a +3 oxidation state. At higher coverages (Θ > 2/3 ML) an additional peak begins to develop at a lower binding energy (513.3 eV). This peak then shifts with increased V coverage to a binding energy of 512.8 eV, which is indicative of metallic vanadium. However, the

vanadium oxide peak continues to increase in intensity with further vanadium growth before reaching a maximum after depositing vanadium for 150 minutes. This additional oxide growth could be due to the high oxygen affinity of vanadium, as the outer metallic vanadium layers react with the residual oxygen within the UHV chamber.

After exposing the partially oxidized vanadium film to atomic oxygen at room temperature, the V 2p and Fe 2p XPS spectra undergo a significant change. As shown in Figure 3.8, the V $2p_{3/2}$ displays a single peak at a binding energy that corresponds to a layer of V_2O_5. This designation is also supported by the presence of a sharp V 2p feature that originates from the d^0 electronic configuration of vanadium cations with a +5 oxidation state. The Fe 2p spectrum is also affected by the vanadia formation. Before the oxidation procedure, the Fe 2p XP spectrum is composed of a combination of the +2 and +3 Fe oxidation states; after the atomic oxygen exposure, the spectrum reflects an iron distribution that is fully reduced to the +3 oxidation state. Therefore, it seems that the substrate can be fully reduced and reoxidized in a repeatable manner, which suggests the supporting α-Fe_2O_3(0001) may play a significant role in the catalytic activity of the surface vanadium layer. Our goal for the XSW experiments described in Chapter 7 is to determine how this enhanced catalytic behavior is influenced by the atomic-scale structure of the vanadium distribution.

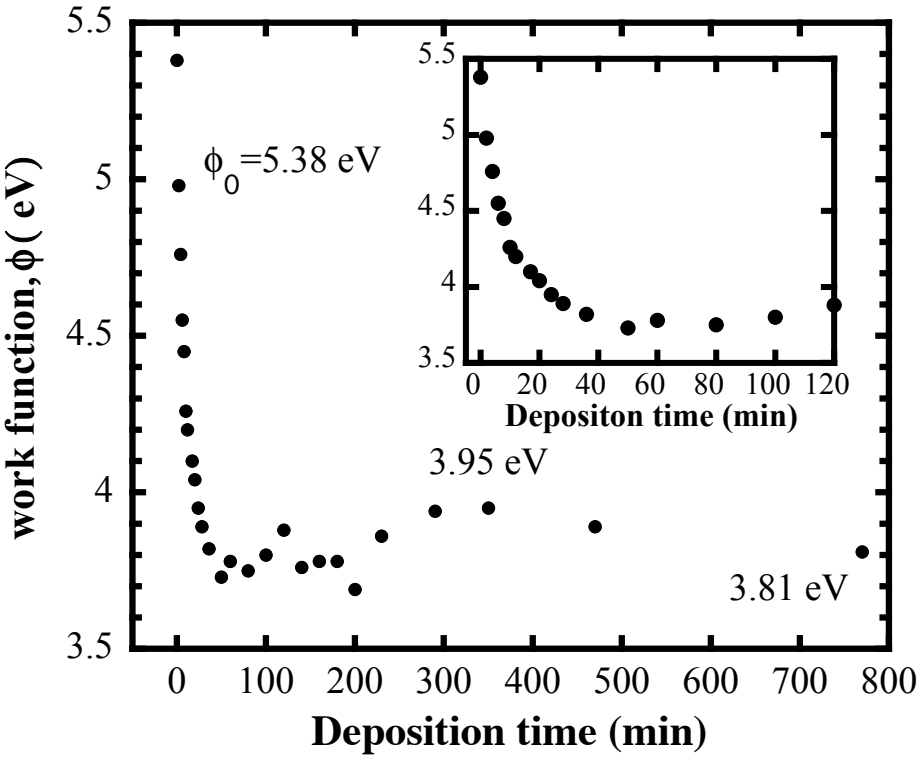

Figure 3.6: The work function as a function of V deposition time. The inset shows the rapid decrease in the work function with the onset of V adsorption. The figure is reproduced from reference [69].

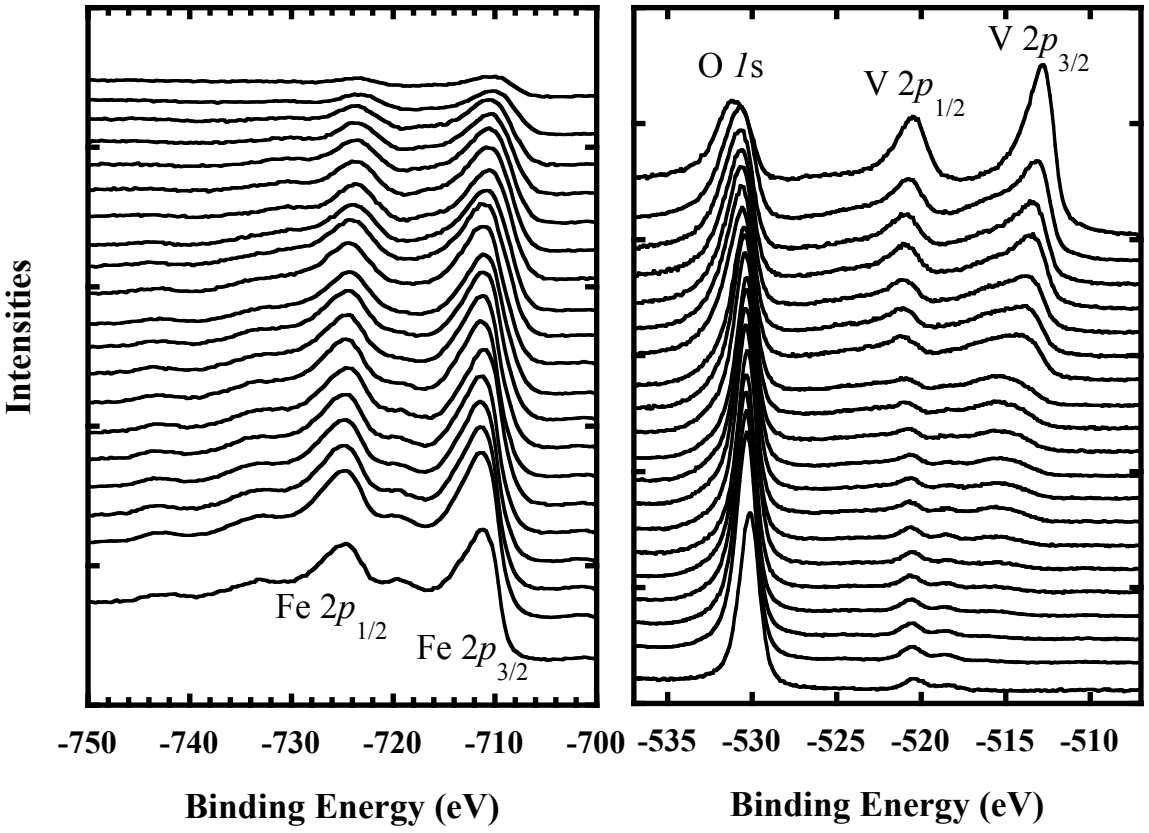

Figure 3.7: The Fe 2p (left) and O 1s and V 2p (right) XPS spectra as a function of increasing vanadium coverage. The spectrum from the clean α-Fe_2O_3(0001) appears as the bottom of the figure. The figure is reproduced from reference [69].

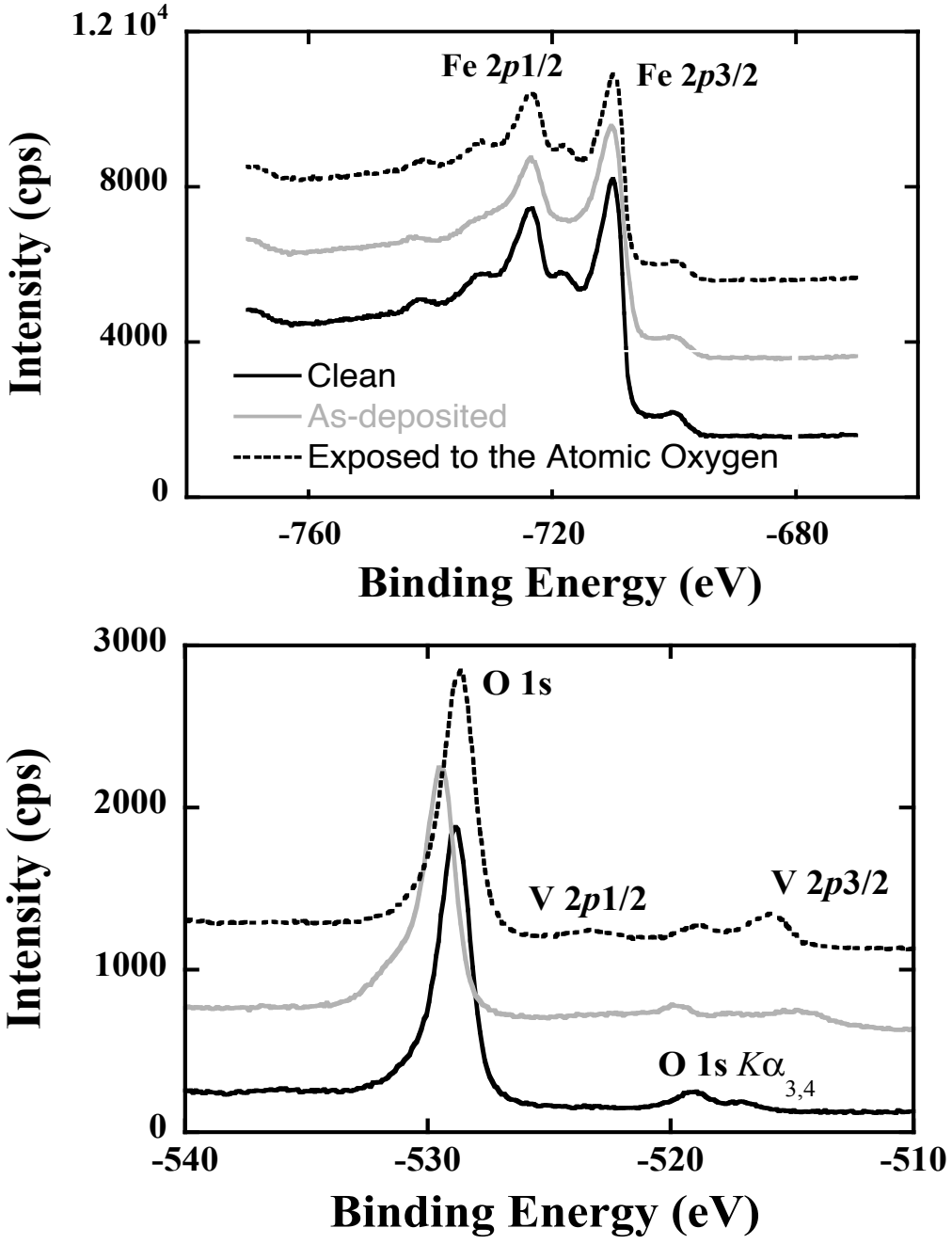

Figure 3.8: The effect of atomic oxygen exposure on the Fe 2p spectra (top) and O 1s and V 2p spectra (bottom). The figures are reproduced from reference [69].

Chapter 4: The X-Ray Standing Wave Method

4.1 Introduction

The X-ray standing wave technique combines both X-ray interference and X-ray spectroscopy to produce an element-specific structural probe. The XSW technique involves the superposition of two X-ray plane waves, which gives rise to a "two-beam" interference field that has a well-defined periodicity and extends beyond the surface of the generating substrate. As the phase between the two plane waves is changed, the antinodes of the XSW moves and induces modulation in the photoemission, x-ray fluorescence, and Auger electron yield from atoms within the field. By monitoring these X-ray spectroscopic yields, the spatial distribution of the excited atoms with respect to the substrate geometry can be directly determined.

In general, an XSW is generated when an incident traveling plane wave (represented by a wave vector $\mathbf{K}_0$) coherently couples with a reflected traveling plane wave with wave vector $\mathbf{K}_H$. The magnitudes of the two wave vectors in vacuum are both equal to $2\pi/\lambda$, where λ is the wavelength of both the incident and reflected X-rays. If the scattering angle between the two plane-waves is 2θ, the X-ray wave vectors are related to each other by the scattering vector $\mathbf{Q}$, which is defined as

$$\mathbf{Q} = \mathbf{K_H} - \mathbf{K_0} . \qquad \textbf{(4.1)}$$

and has an amplitude of $|\mathbf{Q}| = (4\pi/\lambda) \sin\theta$. The scattering vector can also be known as the standing wave vector, since the period of the XSW interference field D is directly related to the magnitude of the scattering vector:

$$D = \frac{\lambda}{2\sin\theta} = \frac{2\pi}{Q}. \quad \textbf{(4.2)}$$

Furthermore, as shown in Figure 4.1, the scattering vector points in the direction of the XSW, as the antinodes of the X-ray interference field form planes that are perpendicular to the standing wave vector.

There are a number of possible ways of producing the two-beam interference condition described above, and each method can generate an XSW with a unique period. For example, when producing diffraction from periodic structures such as crystals or periodic layered-synthetic microstructures (LSM), the standing wave will have a period that is equivalent to the diffraction plane spacing. The d-spacing for single crystals will typically be between 0.5 Å and 10 Å, while the layer period in an LSM, which represents the lattice plane spacing that produces the diffracted X-ray plane wave, can vary between 20 Å to 300 Å. A standing wave with a longer period can also be generated when the incident angle θ is smaller than the critical angle θ_c, which results in total external reflection (TER). During the TER condition the resulting standing-wave field has a period D that varies from infinity at an incident angle of $\theta = 0$ to $D = D_c = \lambda/2\theta_c$ when $\theta = \theta_c$. Therefore, TER-XSW can be used when investigating atomic distributions with length scales from 50 Å to 2000 Å, which would be impossible to probe using an XSW generated with first-order Bragg diffraction. Because the standing-wave period can span several orders of magnitude depending on

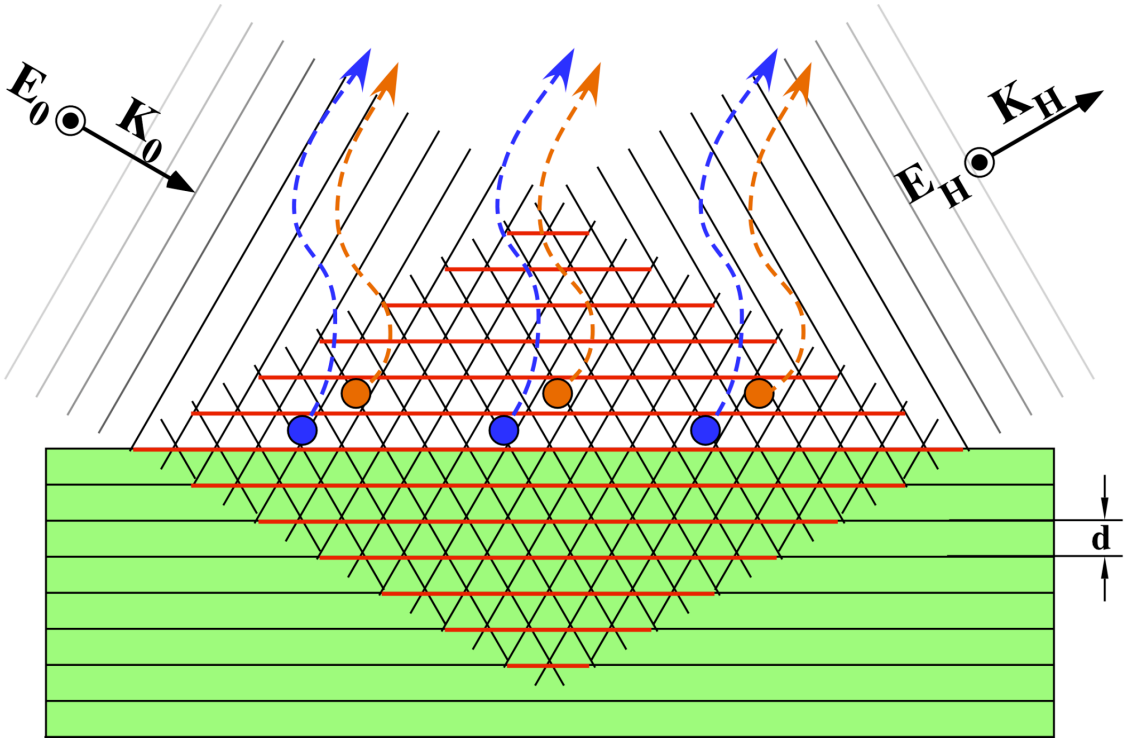

Figure 4.1: The generation of the X-ray standing wave via the interference of an incident and diffracted X-ray plane waves (with wave vectors $\mathbf{K_0}$ and $\mathbf{K_H}$, respectively). The period of the XSW is equal to the lattice spacing d_{hkl} of the Bragg diffraction planes, as seen by the antinodes of the XSW highlighted in red. The electric field intensity of the XSW excites characteristic x-ray fluorescence from atoms in the vicinity of the XSW.

how the interference field is generated, the XSW technique is a powerful tool that can be widely applied to a wide range of materials with an assortment of critical length-scales. In this overview, however, the main focus will be on how an XSW generated via Bragg diffraction from single crystals can be used to probe adsorbate distributions on surfaces.

The development of the XSW technique as a tool for surface science started with Batterman's discovery of an XSW field within a Ge crystal undergoing Bragg diffraction. He also demonstrated how the XSW field shifts as the Ge crystal sweeps through the Bragg condition [70]. This discovery led to the development of the XSW as an analytical tool, as Batterman showed how the location of As impurity atoms within a Si crystal could be determined using the XSW technique [71]. Once it was realized that the standing-wave field also extends above the crystal surface, Cowan *et al*. extended Batterman's findings to surface investigations by using an XSW to determine the height of an adsorbate above its surface [72]. Golovchenko *et al*. later employed both normal and off-normal Bragg reflections in order to determine the in-plane position as well as height of an adsorbate [73]. These early findings showcase some of the inherent advantages of using the XSW technique to investigate surface structures. One such advantage is that the adsorbates in the vicinity of the XSW respond to the standing wave in a chemically specific way. A major issue of many surface science experiments is separating the signal that originates exclusively from atoms on the surface from the

signal that is generated by the appreciably larger number of atoms in the bulk. In the XSW technique, one can easily distinguish the spectroscopic response of the surface atoms from that of the bulk atoms, which in turn provides the necessary surface sensitivity.

In Section 4.2, more detail will be provided about how the standing-wave field behaves and how it can be understood using the dynamical theory of X-ray diffraction. The process in which adsorbate atoms are excited by the X-ray interference field will also be discussed in Section 4.3, as well as how we can take advantage of the dipole approximation when analyzing the induced photoelectric yields. Finally, two distinct approaches of XSW analysis will be presented in Section 4.4: a more conventional model-dependent method in which several XSW measurements are used to triangulate the adsorbate positions, and a newly developed direct-space imaging method that is model-independent.

4.2 Dynamical Theory of X-ray Diffraction

As discussed in the introduction, the creation of a standing-wave field is a fundamental wave phenomenon in which two coherent traveling plane waves interfere with each other. Because the traveling X-ray plane waves can also be considered as electromagnetic waves, they can be expressed in terms of their electric field. The incident plane wave has the form of

$$\vec{\mathscr{E}}_0(\mathbf{r},t) = \vec{E}_0 \exp[-i(\mathbf{K_0}\cdot\mathbf{r}-\omega t)] \tag{4.3}$$

where ω is the X-ray frequency. The diffracted plane wave has a similar form of

$$\vec{\mathscr{E}}_H(\mathbf{r},t) = \vec{E}_H \exp[-i(\mathbf{K_H}\cdot\mathbf{r}-\omega t)], \tag{4.4}$$

and the incident and diffracted wave vectors $\mathbf{K_0}$ and $\mathbf{K_H}$ are related by the scattering vector **Q**. At the Bragg diffraction condition, the scattering vector is equal to the reciprocal lattice vector **H**, which has a magnitude of $|\mathbf{H}| = 2\pi/d_H$, where d_H is the lattice plane spacing of the diffraction planes. This is represented by the Laue condition:

$$\mathbf{H} = \mathbf{K_H} - \mathbf{K_0}\,, \tag{4.5}$$

which in its scalar form is equivalent to the well-known Bragg's law ($\lambda = 2d_H\sin\theta_B$), where θ_B represents the geometrical Bragg angle.

In the spatial region where the incident and diffracted plane waves interfere, the total electric field is simply the sum of the corresponding electric fields, which can be expressed as

$$\begin{aligned}\vec{\mathscr{E}}_T(\mathbf{r},t) &= \vec{\mathscr{E}}_0 + \vec{\mathscr{E}}_H \\ &= \hat{\varepsilon}_0 E_0 \exp[-i(\mathbf{K_0}\cdot\mathbf{r}-\omega t)] + \hat{\varepsilon}_H E_H \exp[-i(\mathbf{K_H}\cdot\mathbf{r}-\omega t)] \\ &= \hat{\varepsilon}_0 E_0 \exp(i\omega t)[\exp(-i\mathbf{K_0}\cdot\mathbf{r})] + \frac{E_H}{E_0}\exp(-i\mathbf{K_H}\cdot\mathbf{r})] \\ &= \hat{\varepsilon}_0 E_0 \exp(i\omega t)\exp(-i\mathbf{K_0}\cdot\mathbf{r})[1 + \frac{E_H}{E_0}\exp(-i\mathbf{H}\cdot\mathbf{r})]\,.\end{aligned} \tag{4.6}$$

While the incident polarization vector $\hat{\varepsilon}_0$ is not, in general, equal to the diffracted polarization vector $\hat{\varepsilon}_H$, we have assumed the X-ray radiation is completely

σ-polarized, which means because the incident and diffracted polarization vectors are collinear and normal to the scattering plane. Because the experiments detailed here used a vertical scattering geometry and made use of the linearly polarized synchrotron radiation from the Advanced Photon Source, this is a valid assumption.

In order to fully describe the behavior of the total electric field, a description of how the incident and diffracted electric fields are related to each other is required. Such a description can be found within the dynamical theory of X-ray diffraction, which was originally developed by Ewald [74], Darwin [75], and von Laue [76]. While the current discussion is focused only on those aspects of dynamical diffraction theory relevant to X-ray scattering in the Bragg geometry, a more complete treatment of dynamical diffraction can be found in Ref. [77].

Dynamical diffraction theory relates the two electromagnetic fields via the ratio of the complex electric field amplitudes, E_H/E_0:

$$\frac{E_H}{E_0} = -\sqrt{|\mathrm{b}|}\sqrt{\frac{F_H}{F_{\bar{H}}}}\left(\eta \pm \sqrt{\eta^2 - 1}\right) , \qquad \textbf{(4.7)}$$

where b is the asymmetry factor that is defined as

$$\mathrm{b} = -\frac{\sin(\theta_B - \phi)}{\sin(\theta_B + \phi)} . \qquad \textbf{(4.8)}$$

The angle ϕ represents the miscut angle between the diffraction planes of the crystal and its optical surface; therefore, for the symmetric (ϕ = 0) Bragg reflections

considered in this dissertation, the asymmetry factor b is equal to –1. The quantity F_H is the structure factor for the **H** Bragg reflection, which is the H[th]-order Fourier coefficient of the electron density of the crystal $\rho(\mathbf{r})$ and therefore can be expressed as

$$F_H = \int_V \rho(\mathbf{r}) \exp(i\mathbf{H}\cdot\mathbf{r}) dV \ . \qquad \textbf{(4.9)}$$

Due to the periodic nature of the crystal, this Fourier component can also be considered as the combined effect of the individual scattering contributions within the unit cell,

$$\begin{aligned} F_H &= \sum_{n=1}^{N} f_n \exp(i\mathbf{H}\cdot\mathbf{r}_n) \\ &= \sum_{n=1}^{N} (f_0 + \Delta f' + i\Delta f'')_n \exp(i\mathbf{H}\cdot\mathbf{r}_n) \end{aligned} \ . \qquad \textbf{(4.10)}$$

The sum over n is over the N atoms that make up the unit cell, and the atomic scattering factor of the n[th] atom at the fractional unit cell location $\mathbf{r}_n$ is f_n. The atomic scattering factor is itself a complex quantity that is wavelength dependent, so the Hönl corrections ($\Delta f'$ and $\Delta f''$) are included with the atomic form factor f_0 in order to account for resonant scattering and absorption. Whether the structure factor F_H is considered a discrete sum or a continuous integral, it is in general a complex quantity and can be written as

$$F_H = F'_H + iF''_H , \qquad \textbf{(4.11)}$$

where F'_H and F''_H are the real and imaginary components of F_H, respectively.

Returning now to the electric field amplitude ratio E_H/E_0, it can be seen that this ratio is a function of the normalized angle parameter η, which in turn is a function of the relative incident angle $\Delta\theta = \theta - \theta_B$ via

$$\eta = \frac{b\Delta\theta \sin(2\theta_B) + \frac{1}{2}\Gamma F_0(1-b)}{\Gamma\sqrt{|b|}\sqrt{F_H F_{\bar{H}}}} \quad . \tag{4.12}$$

The constant Γ is equal to

$$\Gamma = \frac{r_e \lambda^2}{\pi V_c} \tag{4.13}$$

where $r_e = 2.818 \times 10^{-5}$ Å is the classical electron radius and V_c refers to the volume of the unit cell. Because the electric field ratio is a complex quantity and the electric fields are coherent, the electric field amplitude ratio can be rewritten in polar form:

$$\frac{E_H}{E_0} = \left|\frac{E_H}{E_0}\right| \exp(i\varphi) \tag{4.14}$$

The amplitudes of the two electric fields can be related using the reflectivity R, which is defined as the intensity ratio of the two X-ray plane waves:

$$R = \frac{I_H}{I_0} = \left|\frac{E_H}{E_0}\right|^2 \quad . \tag{4.15}$$

Both the reflectivity R and phase φ are functions of the normalized angular coordinate η; an example of this dependence on η is shown in Figure 4.2, which shows the reflectivity and phase for the Si(111) Bragg reflection at $E_\gamma = 7$ keV. The region of

strong Bragg reflection occurs over a small range ω, which is defined as the region where η shifts from +1 to –1. (Because of how η is defined in Eq. 4.12, an increase in incident angle corresponds to a decrease in η.) The angular range ω is known as the Darwin width of the Darwin-Prins reflectivity curve (or rocking curve) and can be expressed as:

$$\omega = \Delta\theta_{\eta=-1} - \Delta\theta_{\eta=+1} = \frac{2\Gamma\sqrt{F_H' F_{\bar{H}}'' + F_0''^2 - F_H'' F_{\bar{H}}''}}{\sqrt{|b|}\sin 2\theta_B}. \quad \textbf{(4.16)}$$

The center of the rocking curve at η = 0 does not coincide with the geometrical Bragg angle at θ_B due to refraction of the X-rays at the crystal surface. The angular offset due to this refraction effect can be expressed as

$$\Delta\theta_{\eta=0} = \frac{\Gamma F_0'}{\sin 2\theta_B}\left(\frac{1+|b|}{2|b|}\right). \quad \textbf{(4.17)}$$

While the reflectivity approaches unity as the crystal is scanned through the rocking curve, the phase φ between E_H and E_0 experiences a significant change. As shown in Figure 4.2, the phase changes by π, as the two plane waves are out of phase when $\eta > 0$ on the low-angle side of the rocking curve but become in phase on the high-angle side (when $\eta < 0$).

While the behavior of the incident and diffracted electric fields within the region of the Bragg condition has been discussed in length, we have not discussed what

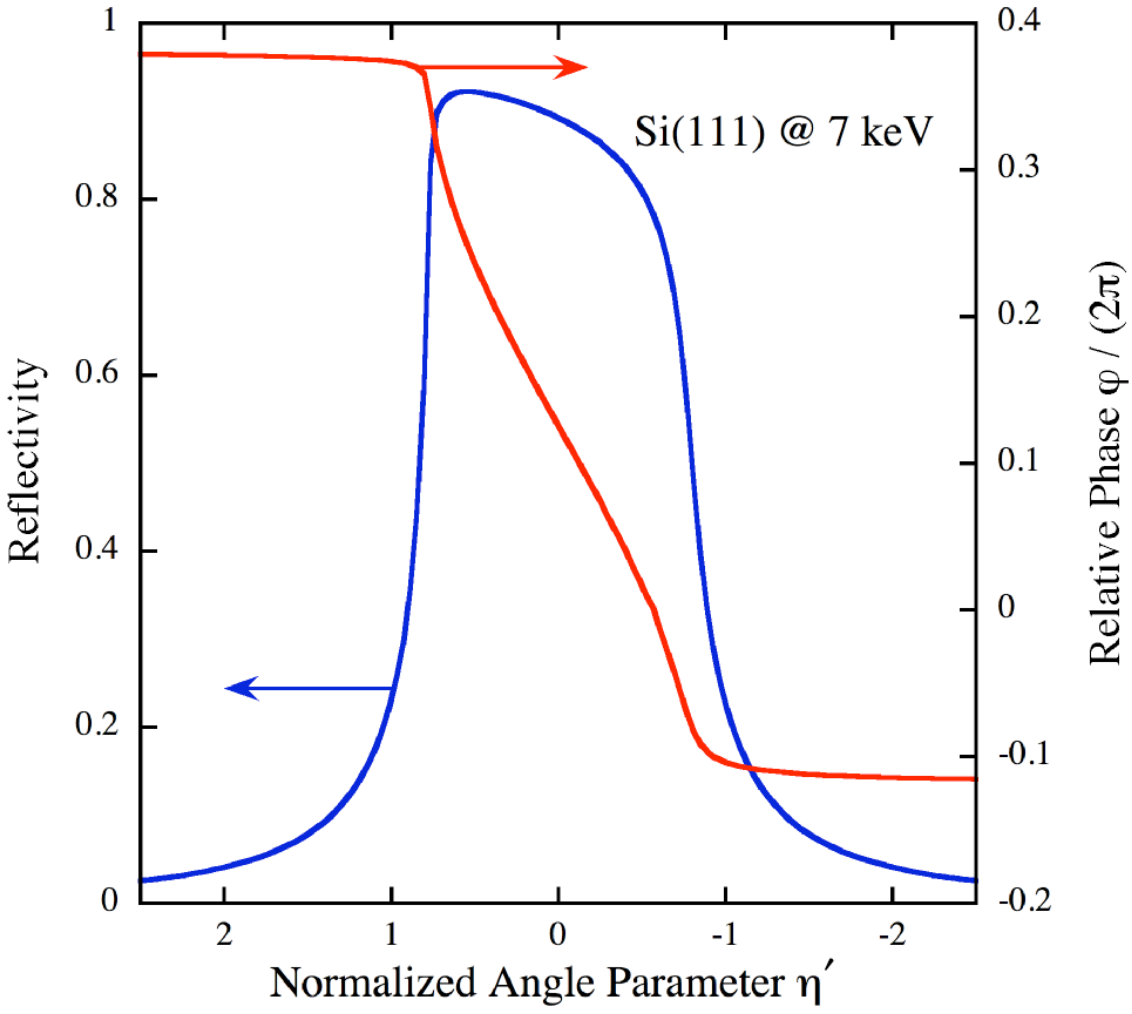

Figure 4.2: The variation in normalized reflectivity and relative XSW phase on the normalized angle parameter η' for the Si(111) Bragg reflection at 7 keV. The relative XSW phase experiences a shift of π radians as the Si crystal traverses through the strong Bragg condition. This results in the antinodes of the XSW field coinciding with the Si(111) Bragg diffraction planes on the high-angle side of the Bragg reflection ($\eta' < -1$). For this phase calculation the unit cell origin (that enters via the structure factor F_{111}) was chosen to coincide with a Si atom in the top of the bilayer.

this means for the total electric field that gives rise to the observed XSW. By substituting Eq. 4.14 in our original expression for the total electric field $\mathscr{E}_T$, Eq. 4.6 can be expressed as

$$\vec{\mathscr{E}}_T(\mathbf{r},t) = \hat{\varepsilon}_0 E_0 \exp(i\omega t)\exp(-i\mathbf{K_0}\cdot\mathbf{r})[1 + \left|\frac{E_H}{E_0}\right|\exp(i\varphi - i\mathbf{H}\cdot\mathbf{r})] \ , \qquad \textbf{(4.18)}$$

and the normalized intensity of the total electric field becomes

$$I(\theta,r) = \frac{\vec{\mathscr{E}}_T \cdot \vec{\mathscr{E}}_T^{\,*}}{|E_0|^2}$$

$$= [1 + R(\theta) + 2\sqrt{R(\theta)}\cos(\varphi(\theta) - \mathbf{H}\cdot\mathbf{r})] \times \begin{cases} 1; & \text{above the surface} \\ e^{-\mu_z(\theta)z}; & \text{at depth z below surface} \end{cases} \qquad \textbf{(4.19)}$$

Within the crystal, $\mathbf{K_0}$ has an imaginary component that leads to the effect of X-ray absorption that is calculated using an exponential damping term $\exp(-\mu_Z z)$, which varies with θ and z, the depth below the surface. The quantity μ_Z is the effective linear absorption coefficient and is defined as

$$\mu_z(\theta) = \frac{\mu_0}{\sin\theta_B}\left[1 + \frac{F'_{\bar{H}}}{F''_0}\left(\frac{E_H}{E_0}\right)'' + \frac{F''_{\bar{H}}}{F''_0}\left(\frac{E_H}{E_0}\right)'\right], \qquad \textbf{(4.20)}$$

where μ is the linear absorption coefficient and is equal to

$$\mu_0 = \frac{2\pi}{\lambda}\Gamma F''_0 \ . \qquad \textbf{(4.21)}$$

The first term in Eq. 4.20 accounts for normal absorption, while the second and third terms dominate when in the vicinity of a Bragg reflection. This explains the strong extinction effect that strongly reduces the X-ray penetration depth as the crystal scans through a Bragg reflectivity peak.

Looking closely at the total electric field intensity given by Eq. 4.19, it is clear that the superposition of the incident and diffracted plane waves has resulted in a time-independent, spatially modulated electric field. This wavefield is in fact the X-ray standing wave field produced by the interference of the two traveling X-ray plane waves. The modulation of the electric field take the form of planes, since the dot product $\mathbf{H} \cdot \mathbf{r}$ is a dimensionless real number that is at a maximum in the direction parallel to **H** and equal to zero in the direction perpendicular to **H**. Therefore, the nodes and antinodes of electric field intensity form an XSW with a period that is equal to the lattice d-spacing of the *hkl* diffraction planes.

While the diffraction vector **H** determines the periodicity of the XSW, it is the phase φ that governs the position of the XSW. The phase φ represents both the incident X-rays relative to the diffracted beam, as well as the phase of the XSW with respect to the chosen origin for the structure factor F_H. Typically the origin is selected so that the standing wave phase can be referenced with respect to the diffraction planes. Choosing this particular origin means that when the incident angle is much smaller than the geometrical Bragg angle θ_B, the XSW phase φ is equal to $\varphi' + \pi$, and the nodes of the

XSW coincide with the diffraction planes while the antinodes lie halfway between the diffraction planes. At the other extreme, when the incident angle is much larger than θ_B, the phase φ is now equal to φ' because of the π phase shift of the XSW. This causes the antinodes and nodes to exchange positions, with the antinodes located exactly on the diffraction planes. The end result is that when the crystal is scanned in angle through its rocking curve, the XSW field gradually shifts inward one-half of the XSW period (and therefore one-half of a diffraction plane d-spacing).

4.3 Photoexcitation from X-ray Standing Waves

In the previous section, it was demonstrated that the XSW is a direct result of the scattering of an incident X-ray plane wave from a set of diffraction planes. However, it is the scattering of the standing-wave field itself that enables the XSW to be detected and used as a high-precision structural probe. While there are many possible interactions between the XSW and the atomic distributions of interest, this overview will focus solely on atomic photoexcitation and the secondary emission processes that ensue. The photoexcitation process will be discussed with respect to the dipole approximation, which simplifies the XSW analysis and is partly responsible for the high resolution provided by the XSW technique. While some of the limits of the dipole approximation will be addressed, the dipole approximation is a valid one for all

the XSW experiments discussed in this dissertation. Much of the following treatment draws from the XSW review article by Zegenhagen [78].

For atoms within an XSW field, there is a finite probability that the atoms will interact with the standing-wave field via the photoelectric absorption of a photon with energy $E_\gamma = h\nu$. The photon energy is transferred to an electron, causing it to be excited from its ground state $|i\rangle$ to an unoccupied state $|f\rangle$. If the electron is ejected from the atom into the vacuum, the excited state $|f\rangle$ represents the electron with a kinetic energy of

$$E_{kin} = h\nu - E_B \ , \tag{4.22}$$

where E_B is the binding energy of the electron. The probability of such an excitation from state $|i\rangle$ to state $|f\rangle$ is proportional to the transition matrix element M_{fi}. By using first-order perturbation theory, we can relate the transition matrix element to the electric field **A** that causes the transition by

$$\mathbf{M}_{\mathrm{fi}} \propto \int d^3\mathbf{r}_\mathbf{e} \Psi_f^* \mathbf{A} \cdot \mathbf{p} \Psi_i \ , \tag{4.23}$$

where **p** is the momentum operator and Ψ_i (Ψ_f) represents the wavefunction of the initial (final) state. The electric field **A** is the vector potential of the XSW as expressed in Eq. 4.18:

$$A = \vec{\mathscr{E}}_T = \hat{\varepsilon}_0 E_0 \exp(i\omega t)\exp(-i\mathbf{K_0}\cdot\mathbf{R})[1+\sqrt{R}\exp(i\varphi - i\mathbf{H}\cdot\mathbf{R})] \ . \tag{4.24}$$

where the modulus of the complex field ratio $|E_H/E_0|$ has been replaced with the square root of the reflectivity *R*. The position vector **R** refers to the location of the absorbing electron; this position can be referenced relative to the atom at a position **r** via

$$\mathbf{R} = \mathbf{r_e} + \mathbf{r} \tag{4.25}$$

where $\mathbf{r_e}$ is the location of the electron with respect to the atom. This allows Eq. 4.24 to be rewritten as

$$\begin{aligned}\mathbf{A} = \vec{\mathscr{E}}_T = \hat{\varepsilon}_0 E_0 \exp(i\omega t)\exp(-i\mathbf{K_0}\cdot\mathbf{r})\exp(-i\mathbf{K_0}\cdot\mathbf{r}_e)\times \\ [1+\sqrt{R}\exp(i\varphi)\exp(-i\mathbf{H}\cdot\mathbf{r})\exp(-i\mathbf{H}\cdot\mathbf{r}_e)]\end{aligned} \tag{4.26}$$

The exponential functions of $\mathbf{r_e}$ has the Taylor series expansion

$$\begin{aligned}\exp(-i\mathbf{K_0}\cdot\mathbf{r}_e) &= 1 - i(\mathbf{K_0}\cdot\mathbf{r}_e) + \tfrac{1}{2}(\mathbf{K_0}\cdot\mathbf{r}_e)^2 - \ldots, \\ \exp(-i\mathbf{H}\cdot\mathbf{r}_e) &= 1 - i(\mathbf{H}\cdot\mathbf{r}_e) + \tfrac{1}{2}(\mathbf{H}\cdot\mathbf{r}_e)^2 - \ldots\end{aligned} \tag{4.27}$$

which is equivalent to a multipole expansion. In the dipole approximation, only the first order term is significant because it is assumed the terms $\mathbf{K_0} \cdot \mathbf{r_e}$ and $\mathbf{H} \cdot \mathbf{r_e}$ are negligible. Therefore, the terms $\exp(-i\mathbf{K_0} \cdot \mathbf{r_e})$ and $\exp(-i\mathbf{H} \cdot \mathbf{r_e})$ are both equal to 1, and the electric field **A** can be rewritten as

$$\mathbf{A} = \vec{\mathscr{E}}_T = \hat{\varepsilon}_0 E_0 \exp(i\omega t)\exp(-i\mathbf{K_0}\cdot\mathbf{r})[1+\sqrt{R}\exp(i\varphi)\exp(-i\mathbf{H}\cdot\mathbf{r})] \ , \tag{4.28}$$

which is independent of $\mathbf{r_e}$. Therefore, the absorption cross section, which is proportional to the square modulus of the matrix element $\mathbf{M_{fi}}$ and therefore proportional to the square modulus of the electric field, can be expressed as

$$\begin{aligned}\sigma_D &\propto \left|\mathbf{M_{fi}}\right|^2 \propto \left|\mathbf{A}\right|^2 \\ &\propto \left|E_0 \exp(i\omega t)\exp(-i\mathbf{K_0}\cdot\mathbf{r})[1+\sqrt{R}\exp(i\varphi)\exp(-i\mathbf{H}\cdot\mathbf{r})]\right|^2 \\ &= \left|E_0\right|^2[1+R+2\sqrt{R}\cos(\varphi-\mathbf{H}\cdot\mathbf{r})]\end{aligned} \quad . \qquad \textbf{(4.29)}$$

Because the photoabsorption cross section is now only a function of the position vector **r** and not $\mathbf{r_e}$, we can ignore the particular details of the electron distribution surrounding the atom and assume the photoemission process occurs only at the exact atom center.

The higher-order multipole terms must be taken into account under certain conditions, such as when using very high energy X-rays or when the electron shells are large and do not have radial symmetry [79]. However, in most cases the second-order quadrupole term is less than 1% of the dipole contribution, which is small enough to correctly apply the dipole approximation.

4.4 XSW Analysis

4.4.1 Measuring atomic distributions with XSW

Given the absorption cross section calculated in the previous section, the normalized fluorescence yield from a single atom frozen at the lattice position **r** and excited by the standing wave field will be

$$Y_H = 1+R+2\sqrt{R}\cos(\varphi-\mathbf{H}\cdot\mathbf{r}) \quad . \qquad \textbf{(4.30)}$$

If it were experimentally possible to acquire only this yield from an individual atom, it would be a simple matter to analyze this signal for a given *hkl* Bragg reflection and

determine the projection along **H** of the position vector **r**. Repeating this for two other noncollinear **H** would determine **r** in three dimensions. However, because an XSW experiment will typically sample a surface area of at least a few tenths of mm^2 in size, the collected fluorescence yield will reflect the ensemble average of all the atoms within the diffraction volume. This diffraction volume will usually excite on the order of 10^{12} atoms on the surface alone.

Therefore, instead of measuring the yield of a single atom at a position **r**, the measured yield will be the sum of the scattered yields from the individual atoms at the position $\mathbf{r}_i$. If there are N atoms that contribute to the overall yield, the normalized scattered yield can be written as

$$Y_H = 1 + R + 2\sqrt{R}N^{-1}\sum_{i=1}^{N}\cos(\varphi - \mathbf{H}\cdot\mathbf{r}_i) \qquad \textbf{(4.31)}$$

Because the XSW yield is a time-averaged sampling of a large ensemble of atoms, atoms that thermally fluctuate about their equilibrium positions will affect the fluorescence yield. For this reason, instead of working with a sum of discrete positions, it is more convenient to consider an atomic distribution function $\rho(\mathbf{r})$, where **r** is a position vector within a unit cell. Such a spatial distribution function can more accurately describe the effect of thermal vibrations, even for the simple case of a single adsorbate located at a unique position. The spatial distribution function is a function of

r, and any arbitrary position **r′** can be represented with respect to the crystalline lattice as

$$\mathbf{r'} = \mathrm{m}\mathbf{a}_1 + \mathrm{n}\mathbf{a}_2 + \mathrm{o}\mathbf{a}_3 + \mathbf{r} \tag{4.32}$$

where $\mathbf{a}_1$, $\mathbf{a}_2$, and $\mathbf{a}_3$ are the axes that define the lattice unit cell and m, n, o are integers. The entire diffraction volume can be parameterized in terms of the unit cell, and the spatial distribution function can then be defined as

$$\int_{V_c} \rho(\mathbf{r}) d\mathbf{r} = 1 \tag{4.33}$$

where

$$\rho(\mathbf{r}) = \sum_m \sum_n \sum_o \rho(m\mathbf{a_1} + n\mathbf{a_2} + o\mathbf{a_3} + \mathbf{r}) \tag{4.34}$$

and V_c is the volume of the unit cell. This atomic distribution function can then substitute for the discrete sum within the expression for the normalized scattered yield (Eq. 4.31).

In the experiments detailed here, the acquired scattered signal from the atomic distribution takes the form of X-ray fluorescence. In this case, the XSW yield is the total fluorescence yield, which is

$$Y_H = Y_{OB}\left[1 + R + 2\sqrt{R}\int_{V_c} \rho(\mathbf{r})\cos(\varphi - \mathbf{H}\cdot\mathbf{r})\exp(-\mu_f(\alpha)z)d\mathbf{r}\right], \tag{4.35}$$

where the normalization factor Y_{OB} represents the off-Bragg fluorescence yield. The exponential term including the effective thickness absorption coefficient $\mu_f(\alpha)$ accounts for the attenuation of the outgoing fluorescent X-rays, which varies as a function of

their take-off angle α. After evaluating the integral, the total fluorescence yield can be expressed as

$$Y_H(\theta) = Y_{OB}\left[1 + R(\theta) + 2\sqrt{R(\theta)}f_H \cos(\varphi(\theta) - 2\pi P_H)\right]Z(\theta)\ , \qquad \textbf{(4.36)}$$

which includes three important parameters: the coherent fraction f_H, the coherent position P_H, and the off-Bragg fluorescence yield Y_{OB}. The coherent position is a measure of the spatial arrangement of the atomic distribution relative to the *hkl* diffraction planes, while the coherent fraction accounts for the ordering in this spatial arrangement.

These three parameters can also be considered with regards to a Fourier analysis of the atomic distribution. In general, the coherent fraction f_H and coherent position P_H are the amplitude and phase, respectively, of the $\mathbf{H}^{th}$-order Fourier coefficient of the spatial distribution function. In other words,

$$\mathcal{F}_H\left[\rho(\mathbf{r})\right] = \int_{V_c} \rho(\mathbf{r})\exp(i\mathbf{H}\cdot\mathbf{r})d\mathbf{r} = f_H \exp(2\pi i P_H) \qquad \textbf{(4.37)}$$

and in general,

$$f_H = \left|\mathcal{F}\left[\rho(\mathbf{r})\right]\right| \qquad \textbf{(4.38a)}$$

$$P_H = \frac{1}{2\pi}\tan^{-1}\left(\frac{\mathrm{Im}\left(\mathcal{F}\left[\rho(\mathbf{r})\right]\right)}{\mathrm{Re}\left(\mathcal{F}\left[\rho(\mathbf{r})\right]\right)}\right) + \begin{cases} 1/2, \text{ if } \mathrm{Re}\left(\mathcal{F}\left[\rho(\mathbf{r})\right]\right) < 0 \\ 0, \text{otherwise} \end{cases} \qquad \textbf{(4.38b)}$$

From our expressions for the spatial distribution function (Eq. 4.33) and the normalized XSW yield (Eq. 4.36), it can be seen that the off-Bragg fluorescence yield is the zeroth-order Fourier ($\mathcal{F}_0$) coefficient of the atomic distribution.

4.4.2 Structural analysis using the coherent fraction and coherent position

Now that the origin of the coherent fraction and coherent position has been established, the remaining question is how these parameters can be used to analyze an unknown atomic configuration. As mentioned earlier, the coherent position is a measurement of the arrangement of the atomic distribution with respect to a selected set of diffraction planes. The coherent fraction is also an indication of the atomic species' geometric configuration, as well as its degree of ordering. One contribution to the atoms' ordering is the thermally induced motion of the atoms. Therefore, the coherent fraction f_H can be considered as the combination of three factors:

$$f_H = C\, a_H\, D_H\,. \qquad \textbf{(4.39)}$$

Each of the three contributions to the coherent fraction can vary from zero to unity. The ordered fraction C is the fraction of atoms that are ordered with respect to the substrate crystalline lattice; an ordered fraction of one corresponds to a completely ordered distribution, while a completely random arrangement of the atoms will result in an ordered fraction of zero. The geometrical factor a_H is a measure of the atomic

arrangement of the fluorescent species, and the Debye-Waller factor D_H accounts for deviations from the atoms' equilibrium positions due to thermal vibrations.

One way of describing the atomic distribution is that some of the atoms of interest are randomly distributed among the crystal, while the rest of the atoms occupy N inequivalent lattice sites with a given occupation fraction. The N different unit cell locations can be represented by $\mathbf{r}_1$, $\mathbf{r}_2$, …, $\mathbf{r}_N$, while the occupation fractions of the atoms at these N sites are c_1, c_2, …, c_N. The ordered fraction C can then be written as

$$C = \sum_{n=1}^{N} c_n \ . \tag{4.40}$$

From Eq. 4.38a and 4.38b, the geometrical structure factor S_H for the coherent atoms can be defined as

$$S_H = \frac{1}{C} \sum_{n=1}^{N} \left[c_n \exp(i\mathbf{H} \cdot \mathbf{r}_n) \right] \ . \tag{4.41}$$

From this definition, the geometrical factor a_H can be expressed as

$$a_H = \left| S_H \right| , \tag{4.42}$$

while the coherent position becomes

$$P_H = \frac{1}{2\pi} \mathrm{Arg}[S_H] \ . \tag{4.43}$$

The last contribution to the coherent fraction is the Debye-Waller factor D_H, which quantifies the effect of thermal vibrations on the time-averaged atomic distribution. This effect can be considered for the entire distribution as a whole or for the individual

atoms that make up the distribution. In this treatment, the assumption is that all the atoms within the spatial distribution have the same vibrational amplitude. By convoluting the atomic distribution with a normalized Gaussian distribution, the Debye-Waller factor D_H can be expressed as

$$D_H = \exp(-M) = \exp\left(-\frac{1}{2}\left\langle u_H^2 \right\rangle H^2\right) = \exp\left(\frac{-2\pi^2\left\langle u_H^2 \right\rangle}{d_H^2}\right). \qquad \textbf{(4.44)}$$

where the term $\left\langle u_H^2 \right\rangle$ represents the mean square vibrational amplitude of the atoms in the **H** direction.

The process of determining the details of an unknown atomic distribution from the measured XSW parameters is best demonstrated with a few examples. The simplest example involves a spatial distribution where all the atoms occupy a single atomic site above the crystal surface. In this case, N = 1, C = 1 (assuming there is no incoherent fraction), and the geometrical factor a_H is equal to unity. Therefore, the coherent fraction f_H is simply equal to the Debye-Waller factor for the fluorescence-selected adatoms, and the coherent position is equal to the $(\mathbf{H} \cdot \mathbf{r})/2\pi$ fractional position of the occupation site relative to the bulk diffraction planes. If the measured coherent position originates from a Bragg reflection in the surface-normal direction, the coherent position will reveal the out-of-plane location of the atomic site. This information can be combined with the results of off-normal XSW measurements in order to determine the in-plane configuration of the adsorbate. Triangulating the unique atomic site position

would theoretically require the combination of three XSW measurements from a set of mutually non-collinear diffraction vectors. However, the adatom will typically be located at a high-symmetry adsorption site, which can be triangulated using one surface-normal and one off-normal XSW measurement. No matter which particular Bragg reflections are employed in an XSW experiment, the derived structural information can be quite precise, since it is the lattice spacing between the selected diffraction planes that represents the "ruler" that probes the atomic distribution.

If the fluorescent-selected atoms occupy multiple sites, the analysis of the coherent fraction and coherent position becomes more complicated. For example, if the atoms were located at two adsorption sites in equal populations, the geometrical factor can be expressed as

$$a_H = \left|\cos\left[\mathbf{H}\cdot(\mathbf{r}_1 - \mathbf{r}_2)/2\right]\right| , \qquad \textbf{(4.45)}$$

and the coherent position will be equal to

$$P_H = \frac{(r_1 + r_2)}{2d_H} . \qquad \textbf{(4.46)}$$

If $\mathbf{r}_1 = \mathbf{r}_2$, the geometric factor would equal one as expected, since this would be identical to the single adsorption site scenario. However, if the two atomic sites were separated from each other by a distance equal to one-half of the lattice d-spacing $\left(|\mathbf{r}_2 - \mathbf{r}_1| = d_H/2\right)$, then the geometrical factor (and therefore the coherent fraction) will be equal to zero. This situation is directly comparable to the case when a particular

Bragg reflection is forbidden due to its structure factor. Furthermore, if the coherent fraction is zero, the measured coherent position does not convey any meaningful information about the atomic distribution. If an intermediate distance separated the two atomic sites, however, the coherent position would be equal to the average position of the two adsorption sites with respect to the diffraction planes, and the geometrical factor would be nonzero.

Of course, real materials systems can involve much more complex distributions made up of multiple adsorption sites that have different occupation fractions, and it may not be possible to directly determine the locations of the atoms from the set of measured XSW parameters. In such cases analyzing XSW data will typically involve designing a reasonable structural model based on existing information and using this model as the basis for calculating a set of coherent fractions and coherent positions. By comparing the XSW parameters calculated from the chosen structural model to the measured XSW data, the model can be refined using a best-fit chi-squared routine. However, this method can be problematic if there are errors or omissions in the initial model that traditional XSW analysis cannot reveal; in such a scenario, an inappropriate model could lead to a result that would be compatible with the experimental XSW data but ultimately flawed. While acquiring several sets of XSW measurements or making other types of structural measurements would minimize this possibility, it would be preferable if the structure determined by the XSW analysis was independent of the

fitting procedure or the initial model used in the fit. This is made possible with the XSW direct space imaging method, which takes advantage of the phase information that is retained in the XSW technique to produce a model-independent direct space image of the atomic distribution. How this image is generated is the subject of the following section.

4.4.3 The XSW direct-space imaging method

One of the inherent limitations of conventional diffraction experiments is that by only measuring the intensity of the diffracted X-rays far from the region where the incident and reflected X-ray beam coherently couple, any information regarding the relative phase between the incident and scattered X-rays is unavailable. However, in an XSW experiment, not only do we detect the intensity of the diffracted beam, but we also detect the intensity of the electric fields itself using the characteristic fluorescence emitted from the atoms that lie within the XSW. As elucidated in Section 4.4.1, by measuring the electric field intensity via the modulation of the induced fluorescence yield, the amplitude and phase of the scattering amplitude of an individual atomic species can then be extracted in the form of the coherent fraction and coherent position.

Because the coherent fraction and coherent position together make up the $\mathbf{H}^{th}$-order Fourier coefficient of the XSW-measured atomic distribution, examination of Eq. 4.37 suggests the atomic density profile of the fluorescent-selected atoms $\rho(r)$ can be

recovered via an inverse Fourier transform. This process has been extensively reviewed by Bedzyk and Cheng [80]. This Fourier inversion involves expressing the atomic distribution as a summation of the available Fourier components:

$$\rho(\mathbf{r}) = \sum_H \rho_H = \sum_H \mathcal{F}_H\left[\rho(\mathbf{r})\right]\exp(-i\mathbf{H}\cdot\mathbf{r}) = \sum_H f_H \exp\left[i(2\pi P_H - \mathbf{H}\cdot\mathbf{r})\right] . \qquad \textbf{(4.47)}$$

The Fourier sum can be simplified by recognizing that the coherent positions and coherent fractions for the $\mathbf{H}$ and $\overline{\mathbf{H}}$ reflections are related by $f_H = f_{\overline{H}}$ and $P_{\overline{H}} = -P_H$. This is mathematically equivalent to Friedel's law, which states that the structure factors for the case of $\Delta f'' = 0$ follow the rule $F_H = F_{\overline{H}}^*$. Furthermore, because the desired result ρ(r) is a normalized distribution function, the 0th-order Fourier coefficient is equal to unity. Therefore, the Fourier sum that represents the spatial distribution function can be written as

$$\rho(\mathbf{r}) = 1 + 2\sum_{\substack{H\neq 0 \\ H\neq\overline{H}}} f_H \cos(2\pi P_H - \mathbf{H}\cdot\mathbf{r}) . \qquad \textbf{(4.48)}$$

This distribution function can then be imaged as a three-dimensional, element-specific atomic density profile.

While it may seem quite simple to apply the XSW imaging approach, there are some important caveats regarding its use. First of all, because the XSW originates from the strong Bragg reflection of the substrate crystal, the Fourier summation is restricted to including only the set of XSW-determined Fourier coefficients for which the

corresponding bulk structure factor is nonzero. This limitation means the atomic distribution that results from the Fourier sum will be projected within the bulk primitive unit cell. For example, in surface studies it is often that the adsorption of foreign atoms on a surface produces a change in the surface geometry and an expansion of the surface unit cell. It would be impossible to fully probe this reduction in the surface symmetry relying on the XSW-derived imaging approach alone, since the image would represent the new extended atomic-scale structure as compressed within the primitive substrate unit cell.

While the structure factor of the substrate restricts the amount of possible Fourier coefficients that can be included in the Fourier sum, the limited amount of time allowed for an XSW experiment and the technical constraints affecting the experiment itself (such as an unachievable X-ray energy or sample geometry) prevent the collection of all but a fraction of the available Fourier components. Because the summation can only contain a finite number of Fourier components, its abrupt termination will be reflected in the resulting image as background density oscillations. As additional Fourier terms are included and the truncated Fourier sum more closely reproduces the real atomic density distribution, the amplitude of these background oscillations will decrease, while the actual atomic density maxima will intensify. Therefore, it is to our advantage to include as many Bragg reflections as possible to lessen the likelihood of mistaking a false background peak for an actual atomic position.

Another benefit of including as many sets of XSW data as possible is the resolution of the calculated profile will improve as higher-order reflections are added to the Fourier sum. This is because the full width at half maximum (FWHM) of any given density maxima will be no smaller than approximately $d_{H_{\max}}/2$, where $d_{H_{\max}}$ is the d-spacing of the highest order Bragg reflection $H_{\max}$. Any structural characteristic smaller than this length scale would be masked by the width of the atomic density peak and be impossible to resolve. Even a structural feature that is only slightly larger than $d_{H_{\max}}/2$ (such as the separation between two adatoms in a reconstructed surface) may not be properly displayed in the direct-space image; while the feature may be correctly represented in a qualitative sense, the quantitative details (such as the amount of separation or the absolute atom positions) may not be correct if the resolution of the image is insufficient. Therefore, if finer structural details are to be determined, collecting higher-order Fourier terms in a particular direction may be more important than accounting for a wide area of reciprocal space using several in-plane Bragg reflections.

The characteristics of the XSW direct-space imaging technique discussed above can be summarized with a few examples. The simplest illustration involves calculating the atomic density profile along a single direction, such as the surface normal. While the result of the one-dimensional calculation is obviously not as comprehensive as the full three-dimensional atomic density profile, it can be quite useful, for instance, when

(*hkl*) reflection	(111)	(222)	(333)	(444)	(555)	(666)	(777)	(888)
f_H	0.707	0	0.707	1	0.707	0	0.707	1
P_H	-0.125	0	0.125	0	-0.125	0	0.125	0

Table 4.1: The calculated values for coherent fraction f_H and coherent position P_H for the bulk Si atomic distribution in the [111] direction. The unit cell origin chosen for this calculation coincides with the Si atom located at the top of the bilayer. Furthermore, the ordered fraction C and Debye-Waller factor D_H are equal to unity.

investigating adsorbate structures in which the in-plane geometry is fairly well-established but the structural details in the out-of-plane direction are in question. This is a rather apt description of the 1/3 ML Sn/Si(111) surface discussed later in this dissertation. Therefore, investigating the bulk Si atomic distribution along the [111] direction would be a suitable example of the XSW direct-space imaging approach.

In order to produce a Si density profile in one dimension, the selected set of coherent fractions and positions presented in Table 4.1 are calculated according to Eqs. 4.39 and 4.43 after choosing an appropriate origin for the Si unit cell. While the coherent fractions listed in Table 4.1 are independent of the choice of unit cell origin, the tabulated coherent positions are not. For the values in Table 4.1, the chosen origin coincides with the top atom of the Si bilayer. For simplicity, the ordered fraction C and the Debye-Waller factor D_H are equal to unity.

The individual contributions of each Fourier component are shown in Figure 4.3(a), which depicts the Si Fourier terms over an interval corresponding to the one-dimensional fractional unit cell along the [111] direction. In total, nine separate *hhh* Fourier components (*h*=0 to 8) are represented in the figure. Figure 4.3(b) demonstrates how the Fourier sum changes as higher-order terms are included in the summation of Eq. 4.48. The h=1 term arises from the Si(111) reflection and produces a single atomic density maxima centered at z = –0.125. The effect of higher-order Fourier coefficients on the synthesized density distribution starts to become apparent with the addition of the h=3 term (the h=2 term has no effect because the coherent fraction for the (222) reflection is zero). The summation of the h=0 to 3 Fourier terms produces a density profile in which two density maxima appear at z = 0 and z = –0.25. While the two peaks in the distribution are quite broad (FWHM = 0.564 Å as compared to d_{333} = 1.045 Å) and do not appreciably extend beyond the background oscillations, their location does approximate the actual location of the Si atoms within the fractional unit cell.

As the additional higher-order *hhh* terms are added to the h=0 to 3 Fourier components, the amplitude of the density maxima increases and their width decreases, resulting in a better representation of the Si atomic distribution. For example, when the summation only includes the h=0 to 5 *hhh* Fourier terms, the FWHM of the density maxima is equal to 0.323 Å, which is 52 percent of the 0.627 Å spacing between the Si (555) diffraction planes. When the summation is completed up to the h=8 term so that

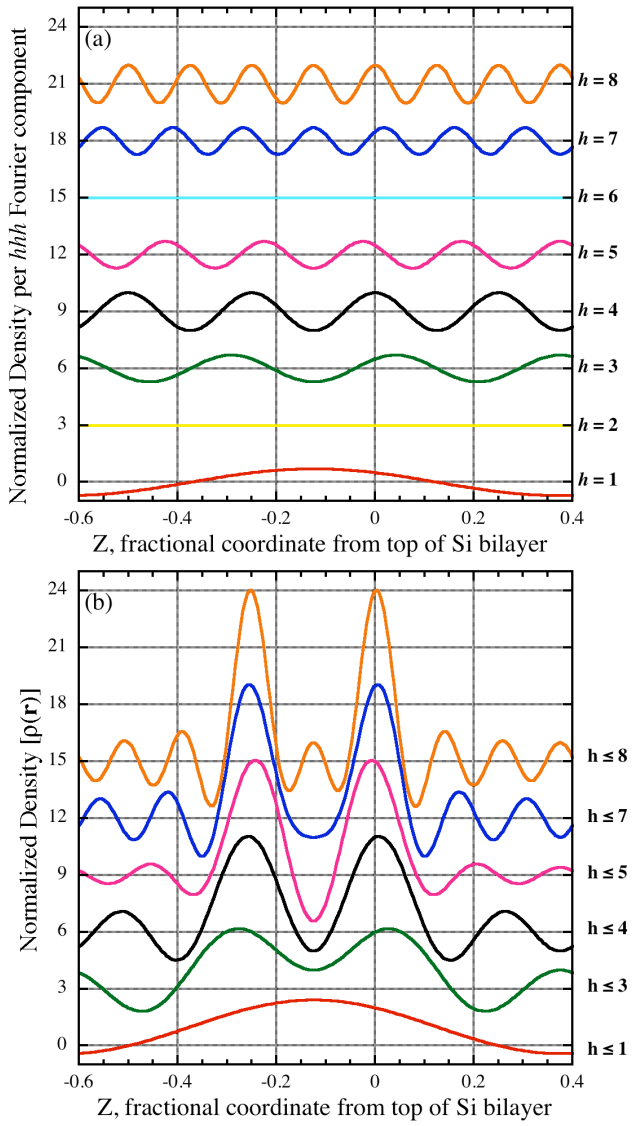

Figure 4.3: (a) Graphical representation of the individual *hhh* Fourier components for the Si atomic density distribution in the [111] direction. Each ρ_{hhh} component is offset by +3 in the vertical scale. (b) The calculated 1D direct-space image of the Si density distribution, which is produced by the summation of the Fourier terms shown in (a). The effect of an increasing number of Fourier components on the density distribution is demonstrated.

the minimum lattice spacing included in the sum becomes d_{888} = 0.392 Å, the FWHM of the density peak shrinks accordingly to 0.21 Å. This reduction in the density peak width helps translate into the improved resolution of the density profile. The amplitude of the background oscillations also subsides as the higher-order Fourier components are included, further improving the accuracy of the density profile. All these trends would continue as more XSW data is inserted into the Fourier summation. In fact, because this simulation assumes the Si atoms occupy only the ordered sites (C = 1) and do not experience thermal vibrations (D_H = 1), if an infinite number of Fourier terms could be calculated and included in the Fourier sum, the density maxima would become infinitely sharp while the background becomes negligible. The density profile would then resemble two delta functions located at the Si atomic positions.

Of course, when investigating an unknown structure, we are often interested in its full three-dimensional atomic density profile and not just its atomic distribution in a single direction. In such cases, the XSW experiment should be tailored so that the desire to generate a high-resolution image using higher-order Fourier components should be balanced with the need to gather data from a wide area in reciprocal space. The symmetry of the bulk crystal can be exploited to help make this goal easier to achieve, since the XSW data obtained from a given Bragg reflection can be also assigned to any other symmetrically equivalent reflection. Because of the bulk symmetry, only a reasonable number of symmetrically inequivalent reflections are

required to populate the Fourier sum with a significant amount of reciprocal lattice data.

As an example of this approach, a three dimensional density profile for the Fe atoms that make up the bulk hematite (α-Fe_2O_3) structure can be generated from a moderate number of Bragg reflections. This example is the three-dimensional analogue to the one-dimensional profile introduced earlier for Si(111). In the V/Fe_2O_3(0001) surface investigation discussed later in this thesis, four symmetrically inequivalent reflections were measured, consisting of one off-normal measurement (the (0006) Bragg reflection) and three off-normal measurements (the $(10\bar{1}4)$, $(01\bar{1}2)$, and $(11\bar{2}3)$ Bragg reflections). Applying the bulk symmetry operators of the hematite structure (space group $R\bar{3}c$) to these four Fourier components increases the number of Fourier terms that are included in the density calculation to 20 reflections. The $(11\bar{2}3)$ Bragg reflection has a multiplicity of 12 for the bulk hematite structure; in the example shown here, all 12 symmetrically equivalent reflections are included in the Fourier summation. The result of the calculation is shown in Figure 4.4, which represents the projection of the atomic density maxima onto the $(11\bar{2}0)$ Fe_2O_3 crystallographic plane. The bulk positions of the Fe atoms have been overlaid on this projection to aid the comparison between the density calculation and the expected bulk structure. For the one-dimensional Si(111) example, the complete result of the Fourier sum was shown. However, in the three-dimensional case, only the regions of the spatial distribution

where the atomic density equals or exceeds 80% of the overall density maximum are shown for the sake of clarity. This example demonstrates how the summation of only four symmetrically inequivalent Fourier components can produce a density profile that successfully replicates the location of the Fe atoms within the interior of the hexagonal unit cell. The FWHM of a given density maxima in the surface normal direction is 1.20 Å. This can be compared to the 2.295 Å d-spacing of the (0006) Fe_2O_3 diffraction planes. However, the density profile is much less precise in the off-normal direction; the maximum peak width of the density maxima as measured in the direction parallel to the basal plane is 2.6 Å. The resolution of this density map can be improved by collecting further Fourier terms using additional off-normal Bragg reflections.

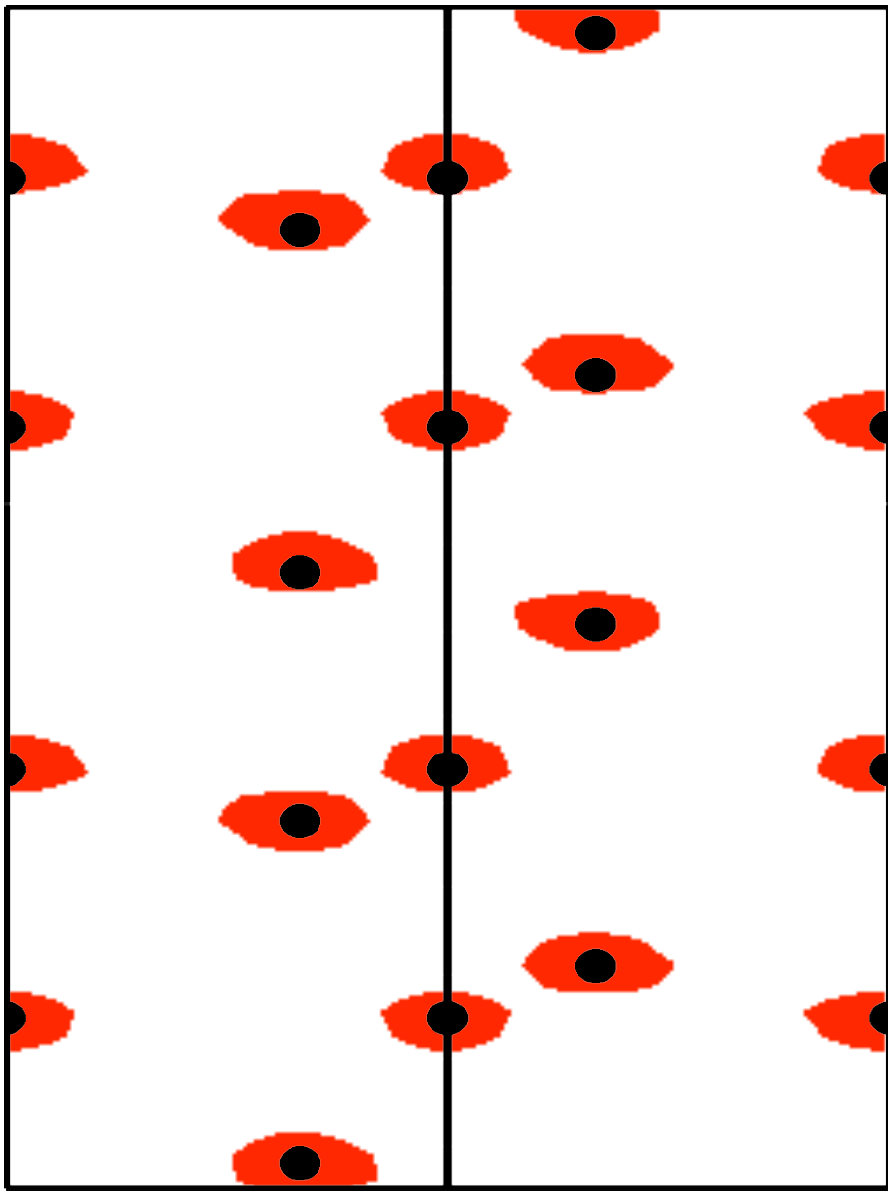

Figure 4.4: Projection of the Fourier summation calculated Fe atomic density onto the $(11\bar{2}0)$ crystallographic plane. The red areas represent regions where the calculated density distribution is greater or equal to 80% of the maximum Fe atomic density. To aid comparison, the locations of the Fe atoms in the bulk hematite structure are shown as black spots overlaid on the density map.

Chapter 5: Experimental Apparatus

5.1 Introduction

Each surface science experiment detailed in this dissertation was conducted at a separate experimental setup, with each having a unique set of x-ray optics and surface science facilities. The Sn/Si(111) investigation was performed at the BESSRC-CAT 12ID-D beamline at the Advanced Photon Source (APS) at Argonne National Laboratory (ANL). The V/Fe_2O_3(0001) study was also conducted at the APS at the DND-CAT 5ID-C beamline. While the surface science chambers at these two experimental hutches have distinctly different capabilities, these two setups have very similar x-ray optics and methods for data collection.

Both setups share the common feature of a UHV surface science chamber for in-situ sample characterization, which is located downstream to a series of x-ray optics (monochromators, x-ray focusing mirrors, etc.), which is used to condition the incident radiation from a synchrotron radiation storage ring. A brief description of all these elements located at the 5ID and 12ID beamline will be presented in Sections 5.2 and 5.3. A short overview of the how XSW data is collected and processed at the APS is given in Section 5.4.

5.2 X-Ray Optics at the 5ID and 12ID Beamlines at the APS

An overview of some of the common features of the 5ID and 12ID experimental setups is schematically presented in Figure 5.1. Both beamlines use photons supplied

by the Hybrid Undulator A, a third generation synchrotron insertion-device source designed by the APS staff. For both experiments the APS operated in top-mode, maintaining the storage ring current at about 100 mA throughout the course of the experiments. The entire V/Fe_2O_3(0001) investigation and much of the Sn/Si(111) experiment was conducted using an incident x-ray beam energy close to 7.00 keV. This energy is within the range of the undulator's first harmonic (2.9 to 13.0 keV). One of the XSW measurements at 12ID required using a higher incident energy (15.80 keV). This was achieved using the third harmonic, which provides for a maximum incident energy of 38 keV.

In order to select the desired energy from the white-beam undulator radiation, both the 5ID and 12ID beamlines employ a double crystal, fixed exit high-heat load monochromator (HHLM). The HHLM at both beamlines is made up two Si(111) crystals in which the position of the second Si crystal is continuously controlled by a feedback mechanism in order to maintain a chosen detuning value. Because the HHLM is exposed to the full power of the x-ray beam, the first Si crystal of the 5ID HHLM is cryogenically cooled. Liquid nitrogen is used to directly cool the first Si crystal of the 12ID HHLM, while copper braids linked to a liquid nitrogen supply cool the second Si crystal.

The post-monochromator optics of the two beamlines differ somewhat. At 5ID, a pair of horizontally deflecting glass mirrors provides both harmonics rejection and

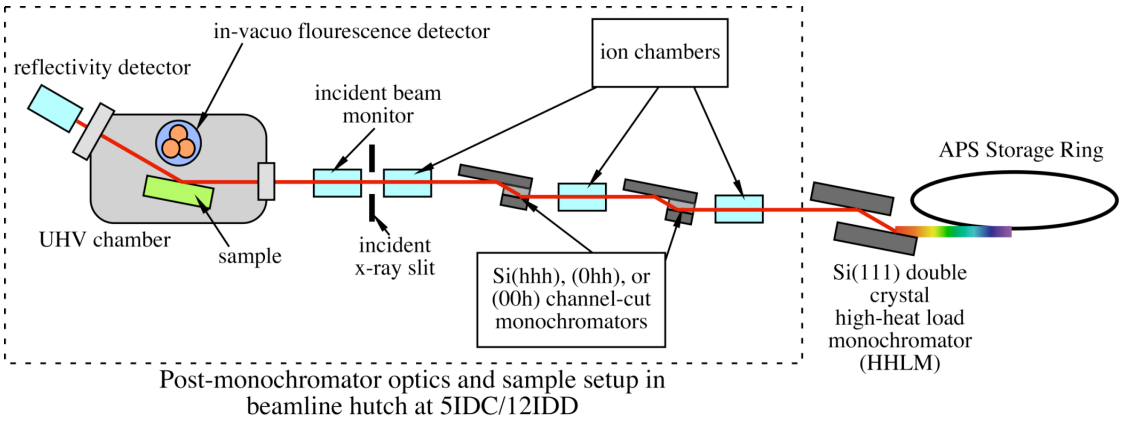

Figure 5.1: A depiction of the experimental equipment located at the 5ID and 12ID beamlines of the Advanced Photon Source. The post monochromator optics and UHV chamber are located in the beamline hutches upstream of the HHLM. Note: the dual focusing mirrors that are used at 5ID-C for rejecting higher-order harmonics are not shown. Also, the reflectivity detector used at 12ID-D is located within the UHV chamber, unlike the external reflectivity detector used at 5ID-C that is depicted here.

horizontal focusing (with 1:1). When working at high x-ray energies (above 11 keV), a stripe of Pt or Rh located on the glass mirror can be used as the reflecting surface; because the experiment of interest was conducted at 7.00 keV, the bare glass surface was used to focus the incoming x-rays. At 12ID, the rejection of higher-order harmonics is achieved by the detuning of the HHLM, at a typical value of 80% of the peak intensity of the Si(111) reflection from the first Si crystal. The x-rays diffracted from the HHLM then pass through an evacuated beam pipe into the experimental hutch (12ID-D or 5ID-C), which contains the post-monochromator optics and the UHV surface science chamber.

The post-monochromator optics serve to reduce the energy and angular dispersion of the conditioned x-rays from the HHLM. It is made up of two non-dispersive, two-bounce Si channel-cut monochromators that are mounted on ZXθ stages. These stages are located on an optical table, which can be remotely moved in the X, Y, and Z directions. Each monochromator is made up of three separate Si channel-cut crystals with a different surface orientation: (00*l*), (*hh*0), and (*hhh*). The three Si channel-cuts are positioned on the XZθ stage so that the desired Si surface orientation can be easily selected to better match the d-spacing of the sample's Bragg reflection. Each channel-cut also has two available gaps to make larger Bragg angles (and therefore energy range) accessible to each channel-cut, which in turn allows a wider range of x-ray energies for the experiment.

Ion chambers filled with He are situated upstream and downstream from each monochromator to measure the x-ray beam intensity before and after being diffracted from the Si channel-cuts. These ion chambers not only allow the intensity of the x-rays to be constantly monitored, but they also are used as the input signals for a feedback loop that continually maintains a user-selectable detuning value of the two Si channel-cut monochromators. The feedback mechanism maintains the chosen detuning setting using either analog monochromator stabilizer (MOSTAB) units (at 5ID-C) or digital MOSTABs (at 12ID-D) to compare the ion chamber signals with the desired detuning value and adjust the angular position of the Si channel-cuts accordingly. These minute adjustments are made by MOSTAB-regulated piezo transducers that deflect the torsion-bearing stages that support the Si channel-cuts. Typically, the first MOSTAB is set to detune the first channel-cut to 80% of the x-ray intensity from the HHLM, while the second MOSTAB keeps the second channel-cut at a detuning value of 25% of the peak intensity from the previous channel-cut. By tuning the channel-cuts to these values, the angular width and energy distribution of the incident x-ray beam is minimized, which improves the phase contrast of the XSW, which in turn makes the XSW results more precise. Finally, in addition to the three ion chambers needed for the channel-cut stabilization setup, there is a fourth ion chamber that measures the beam intensity once the x-ray beam size is defined by a pair of slits.

The end result of the aforementioned x-ray optics can be graphically depicted in

the DuMond diagram shown in Figure 5.2(a). The DuMond diagram depicts the output of the APS undulator, the Si(111) HHLM, and two Si(111) channel-cut monochromators in wavelength-angle space. The vertical stripe is a representation of the undulator output at an incident energy of 7.00 keV and has a width of 2σ = 13.6 μrad. The stripes representing the Bragg reflection from the Si HHLM and channel-cuts have a slope derived from differential form of Bragg's law and an angular width equal to the Darwin width of the Si(111) reflection (ω = 39.4 μrad). The effect of detuning is shown as an angular offset of the stripes representing the detuned monochromators. The output of the optics is represented by the shaded region at the intersection of the stripes; this result can be then compared in Figure 5.2(b) to the Si(111) Bragg reflection. A similar diagram representing the optical setup used for measuring the Si(333) reflection is shown in Figure 5.3. For the V/Fe_2O_3(0001) experiment conducted at 5ID-C, a single Si(022) channel-cut was used as the post-monochromator optic in order to increase the x-ray flux incident on the sample; the effect of replacing the two Si(hhh) channel-cuts with a single detuned Si(022) monochromator is depicted the DuMond diagram shown in Figure 5.4. Because of the mismatch in d-spacing between the Si(022) monochromator (d_{Si022} = 1.92 Å) and the various Fe_2O_3 reflections (d_{0006} = 2.295 Å, $d_{11\bar{2}3}$ = 2.208 Å, $d_{10\bar{1}4}$ = 2.703 Å, $d_{01\bar{1}2}$ = 3.686 Å), there is a measurable broadening of the Fe_2O_3 rocking curve due to dispersion. All the Sn/Si(111) XSW measurements, however, were conducted in a non-dispersive manner.

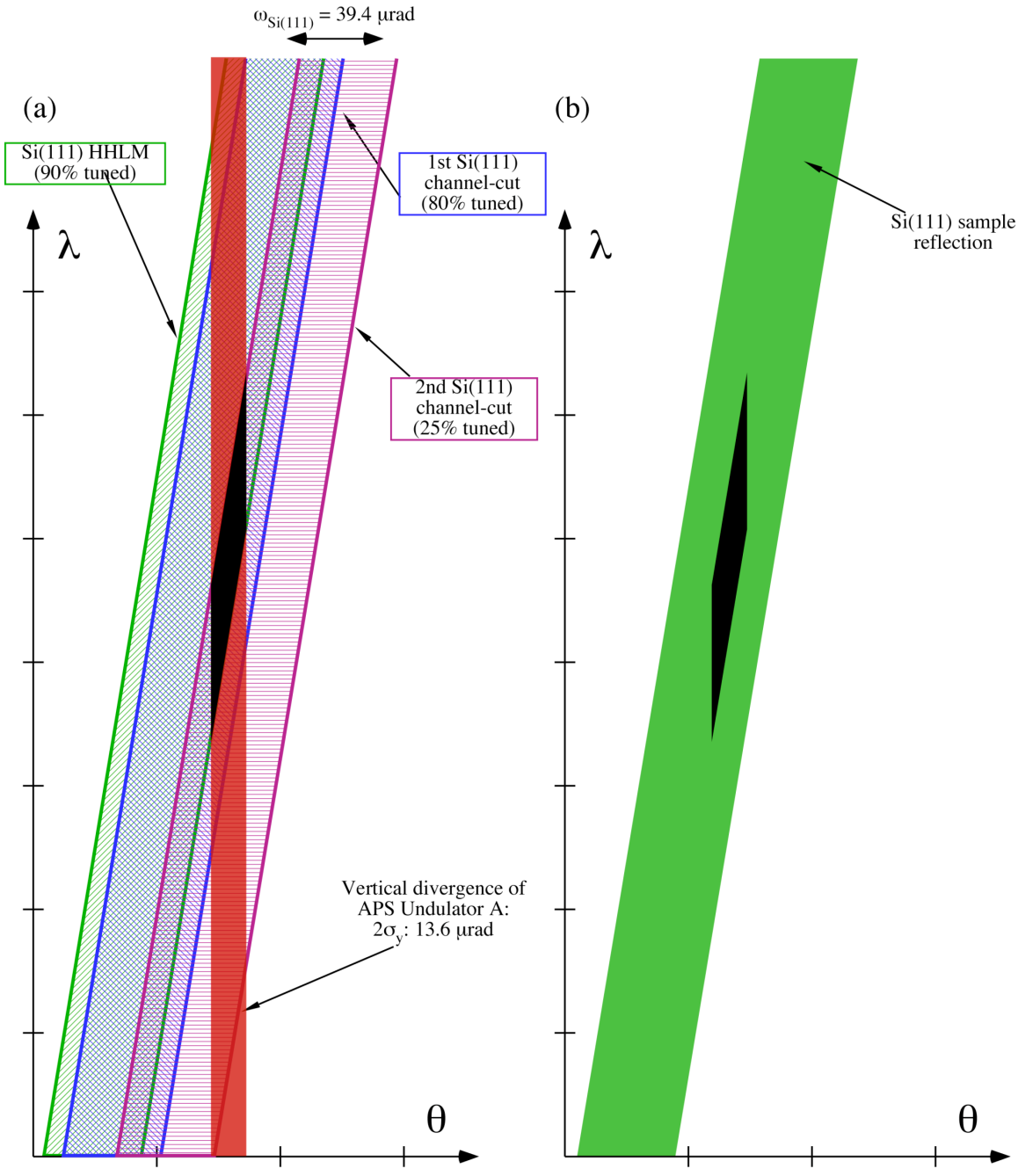

Figure 5.2: DuMond diagram for the x-ray optics of the 5ID-C beamline at 7 keV. The output of the Si(111) high-heat load monochromator and two Si(111) detuned channel-cuts is shown and compared to the Si(111) sample reflection.

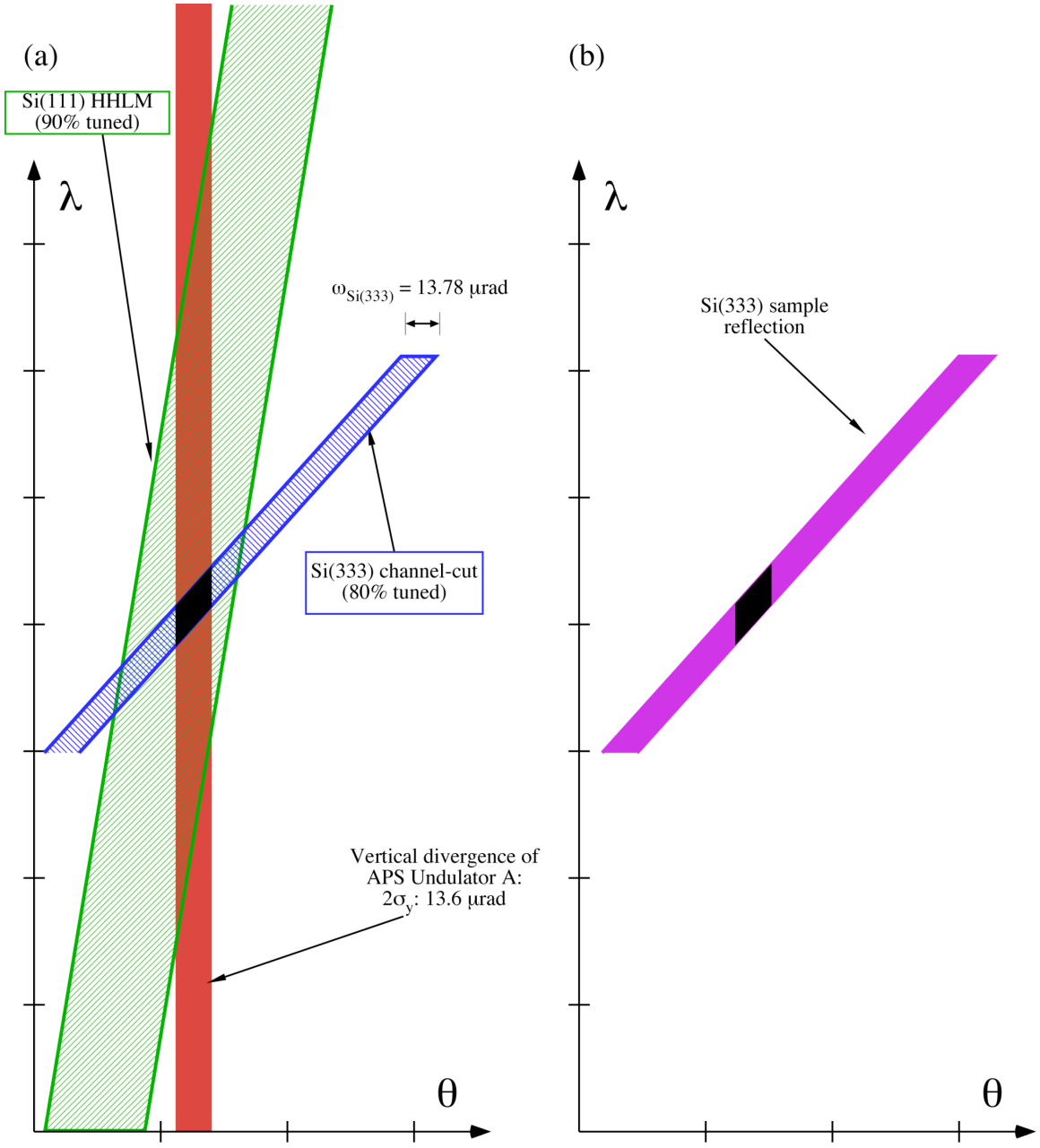

Figure 5.3: DuMond diagram for the x-ray optics of the 5ID-C beamline at 7 keV. The output of the Si(111) high-heat load monochromator and a single Si(333) detuned channel-cut is shown and compared to the Si(333) sample reflection.

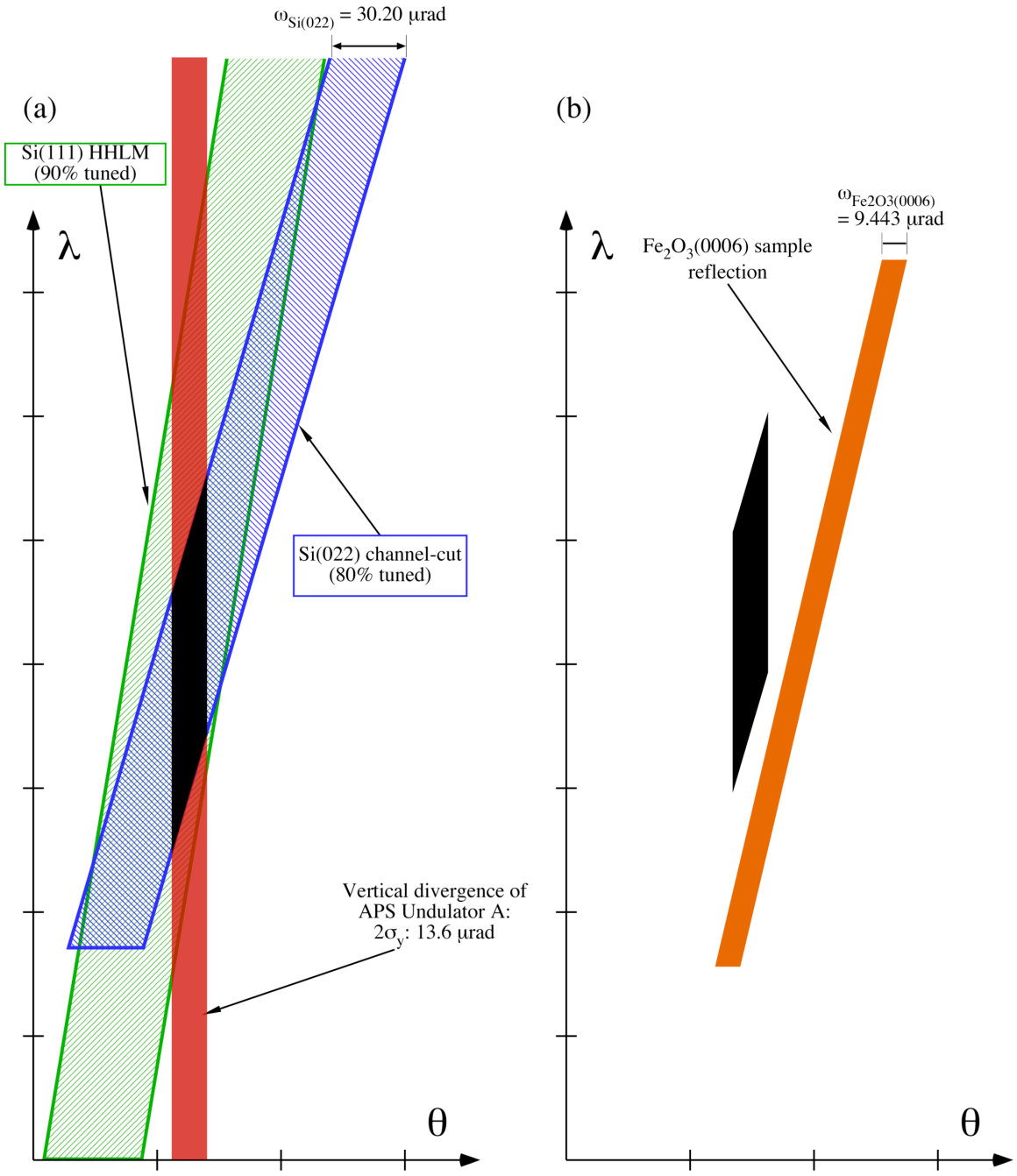

Figure 5.4: DuMond diagram for the x-ray optics of the 5ID-C beamline at 7 keV. The output of the Si(111) high-heat load monochromator and a single Si(022) detuned channel-cut is shown and compared to the Fe_2O_3 sample reflection.

5.3 UHV Surface Science Equipment at the 5ID-C and 12ID-D Beamlines

The UHV surface science chambers located in the 5ID-C and 12ID-D experimental hutches both include facilities for sample preparation and surface characterization using electron-based techniques or synchrotron radiation. However, the two beamlines take different approaches in their design. The UHV chamber in the 12ID-D hutch consists of several chambers dedicated to a single task, such as molecular beam epitaxy (MBE) growth, surface characterization using low-energy electron diffraction (LEED) or Auger electron spectroscopy (AES), or sample characterization using the x-rays from the APS undulator. These separate chambers are all interconnected via an R2P2 chamber, which allows samples to be transferred between the separate systems while maintaining an UHV environment.

On the other hand, the UHV surface-analysis endstation used at the 5ID-C beamline makes use of a single UHV surface science chamber, which contains all the sample preparation and characterization tools required for a variety of surface sensitive techniques. This chamber is part of an entire UHV endstation in which the surface science chamber is an integral part of a psi-circle UHV diffractometer, where *in vacuo* rotational stages within the UHV chamber couple with external rotational axes (for detector and further sample positioning) to allow a wide range of sample orientations with respect to the incoming x-ray beam and a given detector. This allows for a diverse range of possible x-ray experiments, such as x-ray reflectivity (XRR), surface x-ray

diffraction (SXRD) in both grazing-incident and grazing-exit configurations, surface extended x-ray absorption fin structure (SEXAFS), and of course, x-ray standing waves. Both the similarities and differences of the UHV setup at the two APS beamlines will be detailed in the following section, as well as how these differences result in some unique advantages and disadvantages for our XSW measurements.

5.3.1 UHV Chamber at the 12ID-D Endstation

A schematic of the entire UHV surface science assembly is presented in Figure 5.5. As mentioned briefly in the following section, the most distinct feature of the UHV chamber at the 12ID-D station is a central R2P2 chamber, which facilitates sample transfer from the various chambers mounted along the circumference of the R2P2 chamber while maintaining UHV. The vacuum within the R2P2 is maintained by a 400 liter/sec ion pump. A titanium sublimation pump is also available to improve pumping speeds, especially when the chamber pressure rises significantly above the base pressure, which is less than 1×10^{-10} Torr. Two separate chambers are connected directly to the R2P2: a sample carousel for the storage of samples without exposing them to a non-UHV environment, and a surface analysis chamber, which provides both reverse-view LEED and a cylindrical mirror analyzer (CMA) for AES. Samples are typically transferred to the analysis chamber before and after any growth processes or XSW measurements to check the long-range surface structure (using LEED) and the

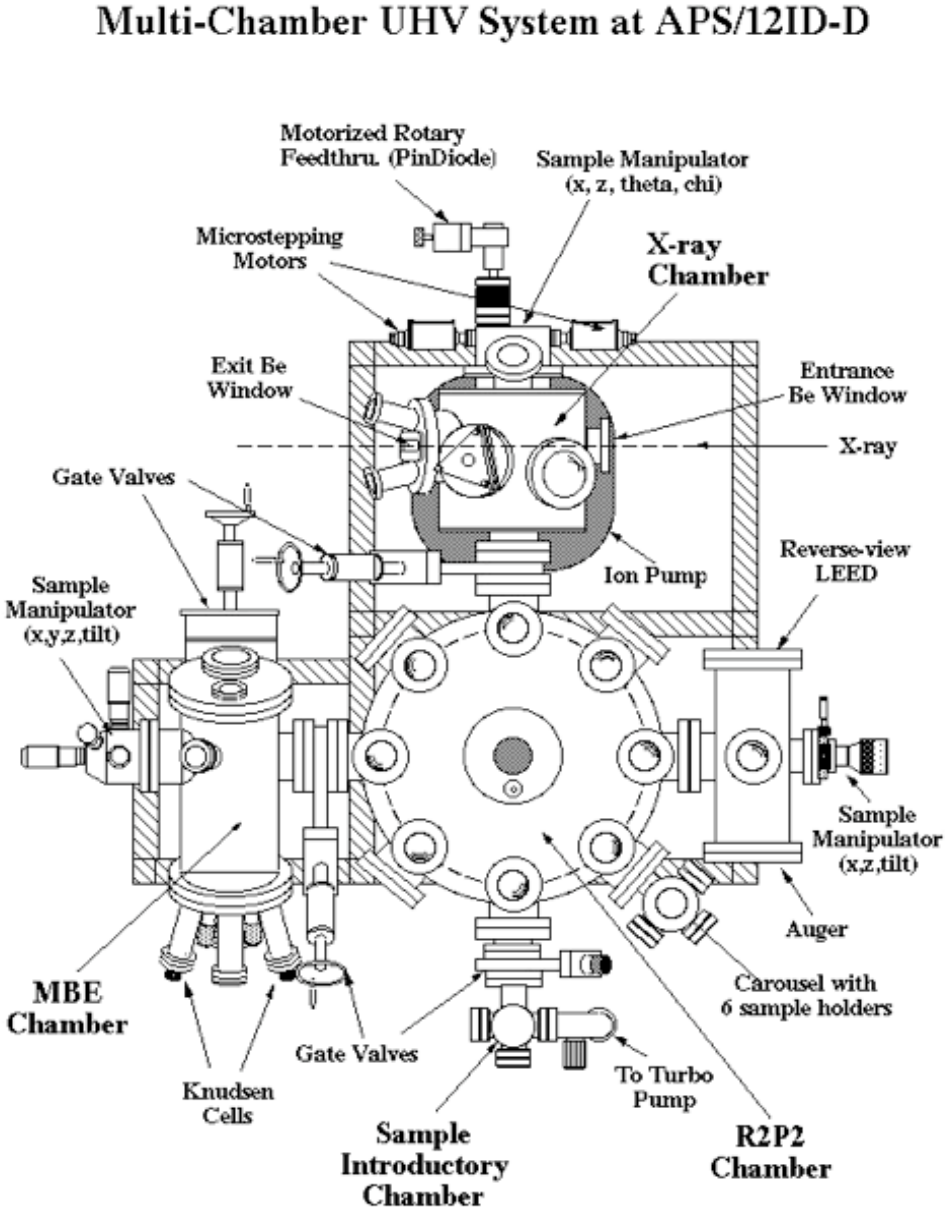

Figure 5.5: Schematic of the top view of the UHV system at the BESSRC 12ID-D undulator system. The figure is reproduced from reference [81].

amount of surface contamination due to residual gases (using AES).

There are three other chambers are accessible from the R2P2, but they are connected to the R2P2 via gate valves so that these chambers may be isolated from the rest of the vacuum system when needed. Therefore, each of these chambers needs their own pumping system to achieve the required vacuum environment. One of these chambers is an introduction chamber, which is evacuated using a turbomolecular pump (TMP). This load-lock system allows the storage of six samples in HV conditions (~1 x 10^{-6} Torr) for eventual insertion into the main UHV chamber; while the gate valve between the load-lock and the main chamber is open, the pressure in the main chamber will usually increase into the 10^{-9} Torr range, but will typically drop quickly once the gate valve is closed.

Another chamber that can be closed off from the R2P2 system is the MBE growth chamber. This chamber contains equipment dedicated to surface preparation, such as three Knudsen cells for atomic deposition, a quartz crystal monitor for monitoring the effusion flux from the Knudsen cells, and a quadrupole mass spectrometer for residual gas analysis. The chamber also contains a sample manipulator for sample positioning and heating to over 1000°C via a tungsten filament. The growth chamber has a base pressure of less than 1 x 10^{-10} Torr, which is achieved using a cryopump. During MBE growth, the gate valve connecting the growth chamber and the R2P2 is usually kept closed, so that the cryopump alone is used to maintain the vacuum

in the growth chamber. However, because the cryopump He compressor causes vibrations in the system that can adversely affect the XSW measurements, the gate valve is opened and the cryopump is turned off during x-ray scans, leaving only the main ion pump to pump on the growth chamber.

The final chamber to be discussed is the x-ray chamber, which can also be isolated from the main system using a gate valve. As such, this chamber has its own 400 liter/sec ion pump and titanium sublimation pump for UHV operation. Because this chamber holds the samples during the actual XSW scans, the chamber must allow for precision orientation of the sample, the detection of both the diffracted beam and the x-ray fluorescence, and of course, a way of allowing x-rays from the undulator to reach the sample. Therefore, the chamber contains a sample manipulator that can translate the sample in the X and Z directions, as well as adjust the incident (θ) and tilt (χ) angles of the sample so that various normal and off-normal reflections can be detected. The manipulator also contains a tungsten filament that allows heating of samples up to 800°C. Detection of the diffracted beam is accomplished using a Si *in vacuo* photodiode that can be positioned up to a two-theta angle of 150°. X-ray fluorescence is measured using a custom-built PGT Si(Li) solid-state detector with a 0.3 mil thick Be window. The detector is seated within a detector "snout", which extends into the x-ray chamber from the chamber top. On the side of the snout near the sample manipulator is a small Be window, which allows fluorescence emitted from the sample to exit the

chamber and be collected by the PGT detector. Finally, two thin Be windows located directly across from one another allow x-rays from the post-monochromator optics to enter and exit the x-ray chamber.

While the aforementioned sample manipulator can be used coarsely position the incident angle of the sample, the motion of the theta stage is not precise enough to scan the sample through its rocking curve without introducing artifacts into the reflectivity curve. Therefore, the entire UHV system is mounted on a frame, which in turn is supported by three z-motion translation stages that are driven by stepper motors. Once the desired Bragg condition is found using the theta drive of the x-ray sample manipulator, these translation stages can be used to "rock" the entire UHV system and therefore scan through the sample rocking curve. The small changes in the sample's incident angle can be as small as 2×10^{-5} degrees in theta, which is fine enough to be able to reproducibly capture the Si(444) reflectivity curve at 9.40 keV ($\omega = 7.7$ μrad). For narrower rocking curves (such as the Si(555) reflection at 11.20 keV, which has a Darwin width of $\omega = 3.0$ μrad), scanning the sample rocking curve can be performed by scanning one of the post-monochromator channel cuts.

5.3.2 UHV Psi-circle diffractometer at the 5ID-C Endstation

The design of the UHV psi-circle surface science diffractometer was motivated by the need to provide a flexible endstation instrument capable of facilitating both

UHV surface preparation as well as surface analysis via x-ray or electron scattering and x-ray or electron spectroscopy. This desired versatility presented a number of design difficulties, one example being the need to position samples within the UHV chamber so that neither x-ray experiments nor electron-based surface analysis would be compromised. The following section will describe how such design challenges were overcome and detail some of the important features of the diffractometer.

A photograph of the UHV chamber/diffractometer at the 5ID-C endstation is shown in Figure 5.6, which shows the UHV system as seen from the downstream direction. The UHV diffractometer sits on an X-Z table, which allows the entire assembly to be positioned with respect to the incoming x-ray beam. The diffractometer configuration is composed of six rotational axes in a psi-circle geometry. The psi-circle configuration is also known as "4S+2D" due to the four degrees of freedom (DOF) for the sample and two DOF for the detector. This design choice allows for a simplified vacuum interface between the UHV chamber and rotational stages; more importantly, it is also responsible for the large amount of reciprocal-space that can be accessed by the detector through the chamber's Be windows. Of the six rotational axes that comprise the psic geometry, four axes (del, eta, mu, and nu) are implemented using high-precision angular stages with 20:1 gear reducers. The UHV sample manipulator contains the stages for the remaining two (chi and phi) rotational motions, as well as an X-Y-Z stage, which is essential for precise translational positioning of the sample with

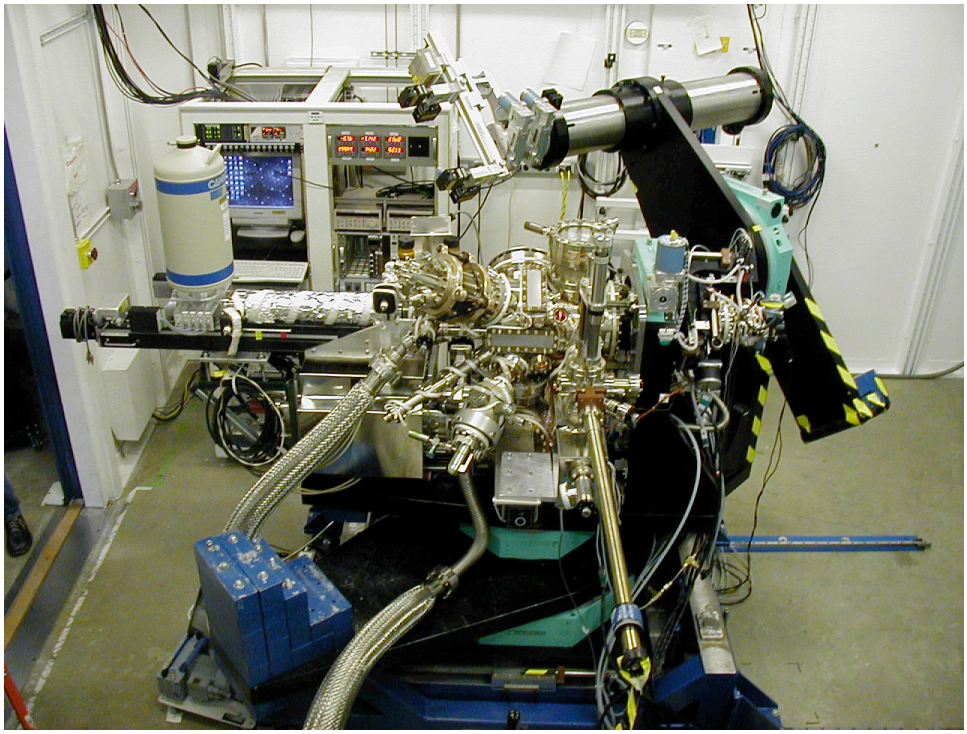

Figure 5.6: Photograph of the UHV chamber/diffractometer located at the 5ID-C endstation. The image is taken from within the endstation and shows the downstream side of the UHV chamber. The entire assembly is situated on a set of rails that allow it to be translated perpendicular to the incident x-ray beam direction; the picture shows the chamber/diffractometer when not in the path of the x-ray beam. The photograph is reproduced from reference [82].

respect to the incoming x-ray beam. For the XSW experiments detailed here, the chi and phi *in vacuo* rotation stages were used to orient the surface normal of the samples so that the desired off-normal XSW measurements could be performed. The diffractometer was then used much like a 2-circle reflectivity setup would be for these XSW experiments, with mu=nu=0, eta=θ, and del=2θ.

While the sample manipulator is an integral part of the psic configuration, it also plays an important role in UHV surface preparation. The sample manipulator contains a tungsten filament for annealing samples up to 1100 K, as well as indirect sample cooling to 115 K from copper braids affixed to the sample stage. The Cu braids are cooled from an *in vacuo* liquid nitrogen reservoir. Other instruments that can be used during sample preparation include a residual gas analyzer, a differentially-pumped ion gun for sputter cleaning samples, three Knudsen cells for MBE growth, a reverse-view LEED, and a double-pass CMA for AES and x-ray photoelectron spectroscopy. Unused ports on the chamber are available for installing more specialized equipment, such as the oxygen source used in the V/Fe_2O_3 study. This oxygen source will be described further in Chapter 7. The entire chamber is evacuated using an ion pump, which is equipped with a titanium sublimation pump and cryoshield and backed by a TMP. This pumping system results in a base pressure of ~1.5×10^{-10} Torr.

As in the 12ID-D x-ray chamber discussed previously, synchrotron radiation enters and exits the UHV chamber via Be windows on Conflat flanges. For the 5ID-C

chamber, a single rectangular Be window allows x-rays to enter the chamber; directly downstream from this window lies a ten inch diameter circular Be window, which allows a wide range of angles for x-rays to exit and be collected. Another smaller rectangular Be window is situated on top of the UHV chamber and permits scattering for larger incident and exit angles. Because of space and design considerations, these Be windows must be located relatively far from some of the other surface analysis equipment, such as the LEED or CMA. Therefore, the sample must be able to occupy a range of positions so that both x-ray and electron analysis can be conducted in the UHV chamber. Instead of requiring the sample manipulator to traverse the length of the UHV chamber so that the sample can be accessed by the Be windows or the various surface science tools, the sample stage remains more or less fixed in space, while the chamber itself can translate independent of the sample and diffractometer. This translation is achieved via a linear translation stage, a large bellows that connects the chamber to the diffractometer, and an air piston system that counteracts the vacuum force using a series of pulleys and cables.

When the chamber is translated into the scattering position, the sample is accessible by a 7-element Canberra Ultra LEGe solid-state detector (SSD), which is the primary detector used for collected x-ray fluorescence spectra. The SSD connects to the UHV chamber via a differentially-pumped custom-built UHV interface that is situated directly opposite the bellows and sample manipulator. When the detector is not used for

data collection (for example, during sample preparation), it can be retracted behind a pair of UHV gate valves that make up part of the UHV interface. In order to collect x-ray fluorescence spectra, these gate valves must be opened and the detector inserted into the UHV chamber. The interface between the SSD and the main chamber has a differential pumping port for a TMP and a set of Kapton seals that wrap around the detector snout. Both devices serve to reduce the pressure increase caused by the presence of the SSD inside the UHV chamber.

The position of the SSD is chosen so that the fluorescence signal from the sample provides reasonable statistics for the XSW scans but does not saturate the SSD electronics. Therefore, the SSD position will depend on the position of the sample, the size of the incident x-ray beam, and the amount of fluorescing material within the diffraction volume. When the detector is fully inserted into the UHV chamber, the SSD detector array will be exposed to x-ray fluorescence arising from not only the sample, but also from the Be windows that span the UHV chamber. Typically this x-ray fluorescence is characteristic of any evaporated material from the Knudsen cells that have been inadvertently deposited on the Be windows. Therefore, a collimator assembly can be placed between the detector snout and the sample in order to restrict the line of sight of the SSD to only the area directly in front of the detector snout. There are three separate collimators that can be rotated in front of the detector, and each collimator can be equipped with thin foils that act as filters to attenuate the strong

fluorescence signal from the sample substrate and prevent pile-up effects. The user can select the foils to be installed depending on the incident x-ray energy and the particular sample; one collimator will usually be used without a filter to allow the full x-ray fluorescence spectra to be collected without attenuation.

5.4 XSW Data Collection at the Advanced Photon Source

While the experimental setups at the 5ID-C and 12ID-D are different in many ways, the process of acquiring XSW data at the APS has been designed to be very consistent between the two beamlines. This allows users to become familiar with how XSW experiments are typically performed at either of the two beamlines, and then be able to apply their experience at the other endstation with a minimum amount of training required. This is made possible by implementing a common interface for experimental control and spectroscopy analysis that can work with the unique experimental setups (such as different vacuum chambers and fluorescence detectors) used at the two beamlines.

One important element of this data acquisition system is the electronics that provide the digital x-ray processing of fluorescence spectra. This electronics system is comprised of the X-ray Instrumentation Analysis (XIA) DXP-2X spectrometers, which digitally analyzes the incoming pulses from the preamplifier of a fluorescence detector. The DXP-2X system features four amplifier and pulse processing channels on a single

CAMAC module, and multiple CAMAC modules can be implemented in a single CAMAC crate. The user can configure the DXP units via a Labview-based software package called MESA. The MESA software also allows the user to inspect the collected fluorescence spectrum or the unprocessed preamplifier output for any of the available channels. More importantly, the DXP units can also interface with the SPEC instrument control software package; therefore, the SPEC software can then be used to control almost every aspect of the XSW experiment, including diffractometer control and all types of data acquisition and processing.

Managing the XSW experiments with SPEC is made much simpler through a set of SPEC macros, which streamline the process of collecting data from XSW scans. These specialized SPEC macros provide a common interface to the different experimental setups at the two APS beamlines, which makes conducting experiments at the APS a much simpler and straightforward process.

One such macro (setxswdxp) allows the user to specify all the important parameters of an XSW scan, such as the number of steps in angle or energy steps per scan, the count time of each step, and the total number of scans to be conducted. Another macro (xswdxp) handles the actual XSW data collection, which involves performing a rocking-curve scan (either by changing the angular position of the sample or the post-monochromator channel-cut) while simultaneously processing the counts from the reflectivity detector and the entire spectrum from the DXP multi-channel

analyzer. The xswdxp macro also contains a drift-control subroutine, which is responsible for adjusting the rocking-curve scan to correct mechanical instabilities and then discarding XSW data collecting during unstable scans. The macro can then records acceptable XSW data to text files, which include all the relevant motor positions, monitor and detector counts, pulse-processing statistics (which can be used to calculate the deadtime of the solid-state detector during a given dataset), and the entire MCA spectrum as processed by the XIA DXP units. While the XSW data from each individual rocking curve scan can be captured separately, it is usually more practical to configure the xswdxp macro to save the sum of several scans into a separate dataset in order to reduce the size of the resulting data files.

Once the data files are parsed using our custom-built XSW analysis software package (SUGO) [83], the fluorescence spectrum collected by the MCA can be extracted. For example, a typical MCA spectrum from one of the Sn/Si(111) XSW scans is shown in Figure 5.7. An incident energy of 6.90 keV was used for these experiments, which shows up in the MCA spectrum as the strong elastic peak located at the far right. The incident x-rays excite the Lα and Lβ x-ray fluorescence from the Sn adsorbate layer at 3287 eV and 3663 eV, as well as Si Kα fluorescence at 1740 eV originating from the underlying Si(111) substrate. Because the Sn/Si(111) investigation was conducted at the 12ID-D endstation, this fluorescence spectrum demonstrates the

performance of the single-element PGT detector used at 12ID-D, with the pulse-height analysis performed by the aforementioned XIA DXP units.

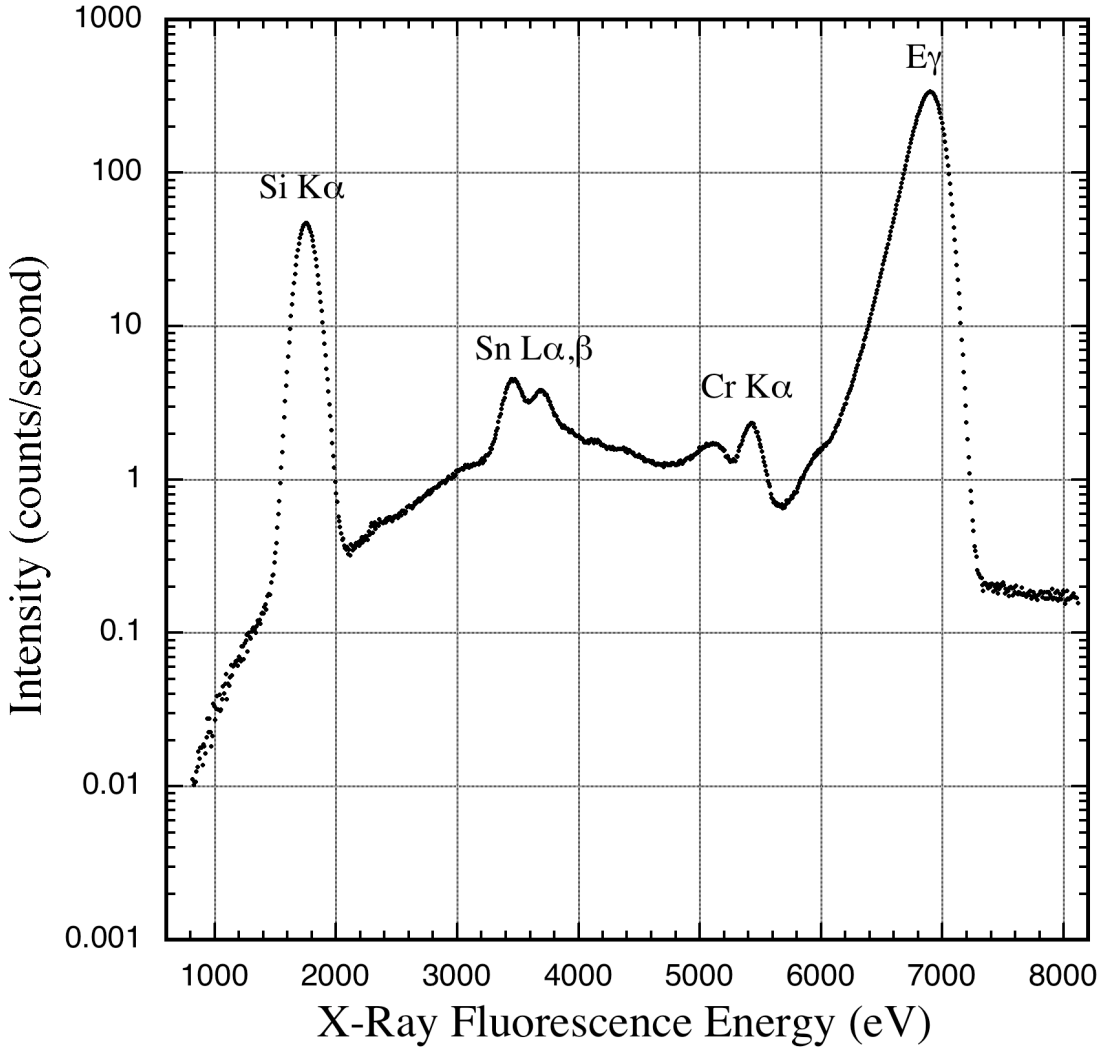

Figure 5.7: One of the x-ray fluorescence spectra collected at the 12ID-D endstation during the 1/3 ML Sn/Si(111) XSW experiment (E_γ = 6.90 keV). The total spectrum is the result of 70 XSW scans added together. Since each scan includes 32 angular steps and the counting time at each step was 1 second, this plot is averaged over 2240 seconds of collection time.

Chapter 6: XSW Measurements of the 1/3 ML Sn/Si(111)-(√3x√3)R30 Surface

6.1 Sample Preparations

Sample preparation and characterization were conducted in an ultra-high vacuum (UHV) chamber (base pressure ~1.5 x 10^{-10} Torr) located at the 12ID-D undulator BESSRC-CAT experimental station at the Advanced Photon Source, Argonne National Laboratory. The single-crystal Si(111) samples were cut from a high purity boule of float zone Si with a miscut angle less than 0.1°. After etching, the Si samples were Syton polished to produce a mirror-like finish. In cases where some Syton residue remained on the sample surface due to the polishing process, the samples underwent an additional cleaning with a piranha etch (H_2SO_4:H_2O_2 [2:1] at 130ºC) to remove any visible polishing debris. The samples were then further cleaned in ultrasonic baths of acetone, then methanol, then finally trichloroethylene.

The degreased samples were then etched using a modified Shiraki process and mounted on molybdenum sample holders before insertion into the UHV system. These holders support the winged design of the Si samples using small strips of tantalum that fit between the sample wings and the sample holder walls; these thin tantalum ribbons apply a small amount of pressure on the wings of the sample, affixing the sample in place without applying undue pressure that could affect the sample rocking curve. Before mounting the Si substrates, the sample holders were degassed by heating them in UHV for several hours at 1273 K in order to minimize any sample contamination

from the sample holder itself. The samples were degassed for 6 to 8 hours at 873 K, and then annealed for 15 min. at 1113 K to remove the chemically grown protective oxide. Auger electron spectroscopy (AES) showed C and O contamination levels to be less than 0.02 ML. The sample temperature during each processing step was measured using an optical pyrometer. The high-temperature anneal produced a clean, well-ordered Si(111)-(7x7) surface, which was confirmed with the LEED images shown in Figure 6.1. A total of 0.33(3) ML of Sn was evaporated onto the clean, RT Si(111) surface at a rate of 0.016 ML/min using an effusion cell. One monolayer on the Si(111) surface corresponds to an areal coverage of 7.8×10^{14} Sn atoms/cm^2. The coverage of Sn was determined in UHV by comparing the intensity of the Sn Lα x-ray fluorescence to that of a Sn-implanted Si(111) standard calibrated by RBS. The samples were annealed for 4 min. at 913 K (a process which has been noted to result in $\sqrt{3}$ surfaces with a minimal amount of Si substitutional defects), and then allowed to slowly cool to RT (at a rate of ~1 K/s). This process resulted in a reduction in the Sn coverage to 0.23(3) ML and a sharp $\sqrt{3}$ LEED pattern, which is shown in Figure 6.1.

To compensate for the significant desorption of Sn from the Si surface during the sample annealing and arrive at a final coverage closer to the ideal Sn coverage of 1/3 ML, a second Sn/Si(111) sample was prepared by depositing 0.45 ML of Sn onto the RT Si substrate. The higher coverage sample was then was annealed at 933K for 2 minutes, which resulted in a surface displaying a sharp $\sqrt{3}$ LEED pattern and a final Sn

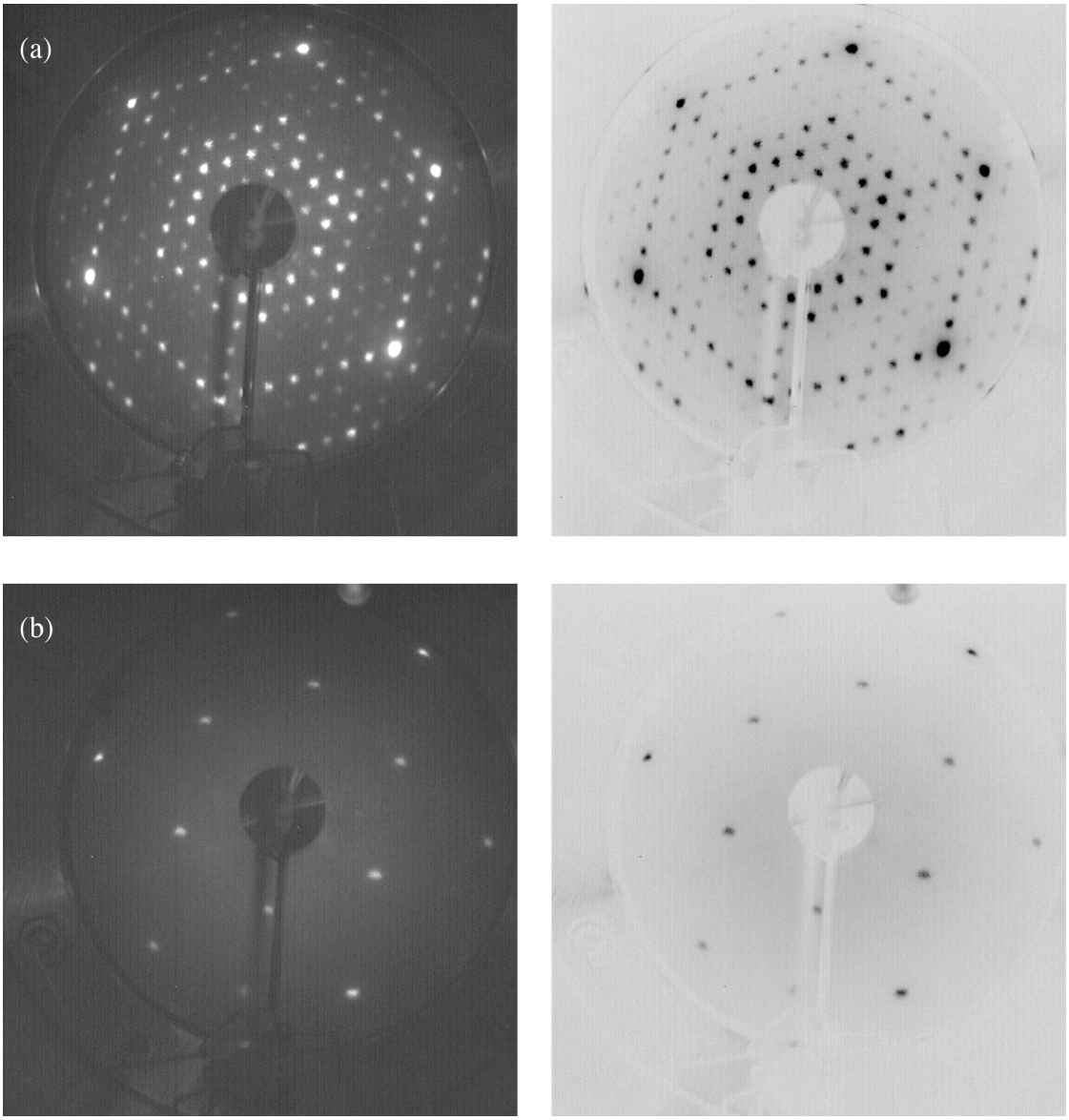

Figure 6.1: LEED images (as captured and inverted) for the different Si(111) surfaces observed during the 1/3 ML Sn/Si(111) XSW experiment. (a) LEED images from the clean Si(111)-(7 x7) surface, E=30.1 eV. (b) LEED images from the 0.23 ML Sn/Si(111)-√3 surface, E=28.5 eV.

coverage of 0.33(4) ML. While the annealing temperature used for this sample was not significantly higher than the annealing conditions for the 0.23 ML Sn/Si surface, the initial Sn coverage was increased by 36% over the first sample. This particular sample was characterized using a different set of XSW measurements as the lower-coverage, 0.23 ML Sn/Si surface, which will be detailed further in the following section.

6.2 X-Ray Standing Wave Measurements

The XSW measurements were made after allowing both samples to cool to room temperature. The data shown in Figs 6.2-6.8 was collected by scanning the 0.23 ML sample in angle through the allowed Si (*hhh*) Bragg reflections (h = 1, 3, 4, and 5) and simultaneously collecting the diffracted beam intensity and x-ray fluorescence spectra (using an *in vacuo* photodiode and energy-dispersive Si(Li) detector, respectively) at each angular step. Three additional off-normal XSW measurements were collected in the same manner utilizing the Si $(\bar{1}11)$, $(\bar{3}33)$, and $(5\bar{1}\bar{1})$ Bragg reflections in order to determine the in-plane Sn distribution. The {111}, {333}, and $(5\bar{1}\bar{1})$ XSW measurements were collected using 6.90 keV x-rays that were conditioned by the high-heat-load 12ID Si(111) monochromator. For the {111} XSW measurements, a pair of detuned non-dispersive Si(111) channel-cut crystals was used to condition the incident beam; in all other cases, a single d-spacing-matched Si(hhh) channel cut was used to maximize the available x-ray intensity on the Sn/Si(111)

sample. Because the range of the motion for the *in-vacuo* photodiode is limited, the higher-order Si(hhh) measurements required the use of higher-energy x-rays (h = 4, 9.40 keV; h = 5, 11.20 keV) to ensure the diffracted x-ray beam would be collected by the photodiode reflectivity detector.

For the higher coverage 0.33 ML Sn/Si(111) surface, the data shown in Figs 6.9-6.13 was collected using the Si (111) and (333) Bragg reflections to provide structural information in the surface normal direction. The higher-order Fourier components employed for the 0.23 ML sample could not be acquired due to experimental time constraints. The Si (022), (311) and ($\bar{1}$33) Bragg reflections were used to probe the in-plane Sn distribution instead of the off-normal {111} and {333} Bragg reflections because of mechanical problems moving the sample surface into the proper orientation. Because the higher-order (*hhh*) Bragg reflections were not collected for the higher-coverage sample, all the XSW measurements for the 0.33 ML surface were acquired using an incident x-ray energy of 7.00 keV. While the XSW data for the (*hhh*) Fourier components employed a pair of detuned non-dispersive Si(111) channel-cut crystals to decrease the angular spread of the incident x-rays, the off-normal XSW data was collected in a dispersive manner by using a single (004) channel-cut as the post-monochromator optics.

Fitting the normalized reflectivity and Sn Lα fluorescence yield with dynamical diffraction theory produced the coherent position (P_H) and coherent fraction (f_H) for the

(*hkl*) reflection	(111)	(333)	(444)	(555)	($\bar{1}$11)	($\bar{3}$33)	(5 $\bar{1}$ $\bar{1}$)
f_H	0.76(2)	0.44(2)	0.20(7)	0.27(8)	0.89(5)	0.36(3)	0.41(4)
P_H	0.61(1)	0.75(2)	0.37(3)	0.92(4)	0.49(1)	0.58(2)	0.58(2)

Table 6.1: Summary of the XSW results for the 0.23(3) ML Sn/Si(111) surface. The unit cell origin coincides with the top of the bulk-like Si bilayer.

adsorbed Sn atoms. A summary of the measured XSW parameters for the 0.23 ML Sn surface is listed in Table 6.1. The coherent positions listed here are with respect to a Si unit cell with its origin centered on the bulk-like Si site at the top of the Si bilayer. Because the sample surface is susceptible to deterioration due to residual gases in the chamber, the coherent fraction may decrease with time as the surface becomes more disordered. Therefore, the (111) XSW measurement was repeated in order to monitor any change in the coherent fraction due to changes of the sample over time was monitored by repeating the (111) XSW measurement. Based on a comparison of these two (111) measurements, the fraction of ordered Sn decreased by 7% over a 42 h period. Because the entire XSW experiment was conducted over a period of ~64 h, it is assumed the effect of sample disorder on the other (*hhh*) measurements is small. Finally, in order to ensure the integrity of the data and analysis the bulk Si Kα fluorescence was analyzed and found to agree with the expected XSW parameters for the Si substrate.

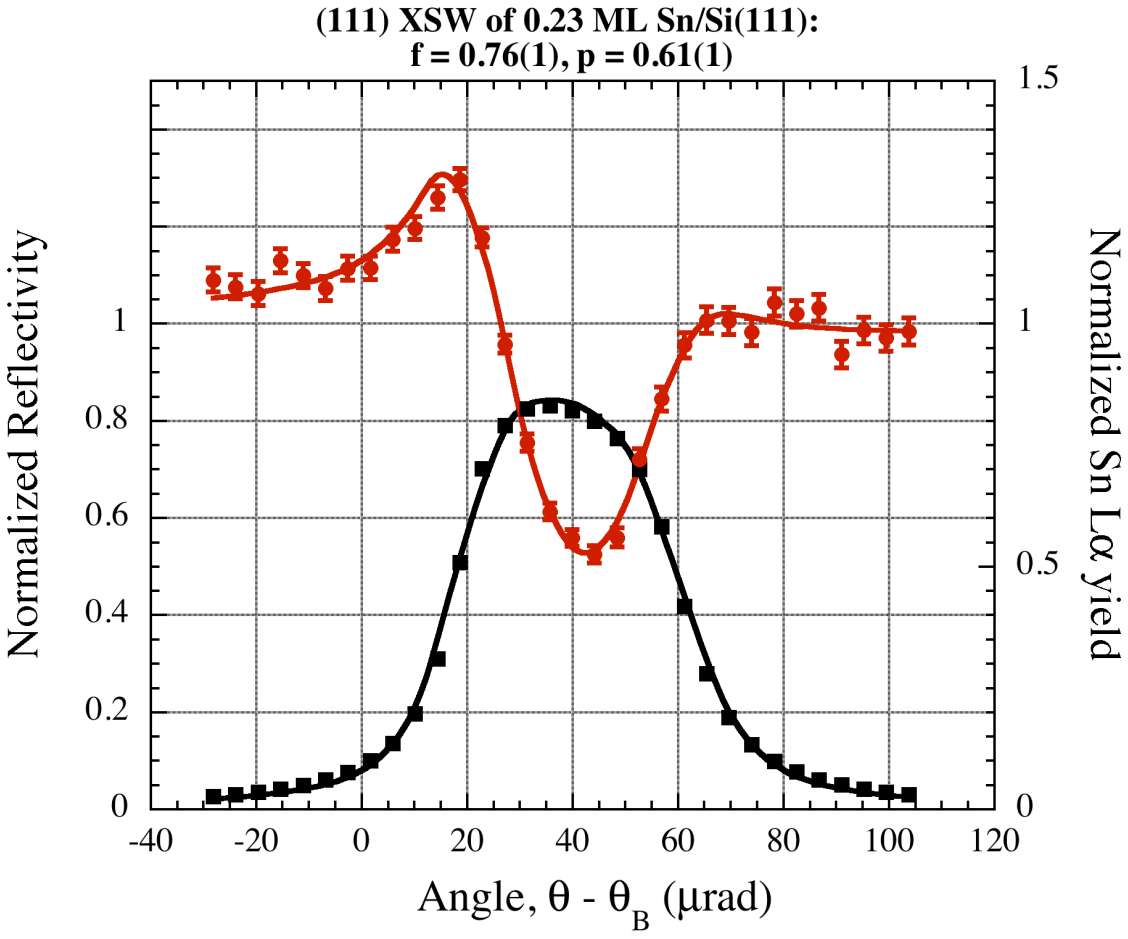

Figure 6.2: Reflectivity (closed squares) and normalized Sn Lα fluorescence yield (closed circles) experimental data along with theoretical fits (solid lines) for the (111) XSW measurement on 0.23(3) ML Sn/Si(111).

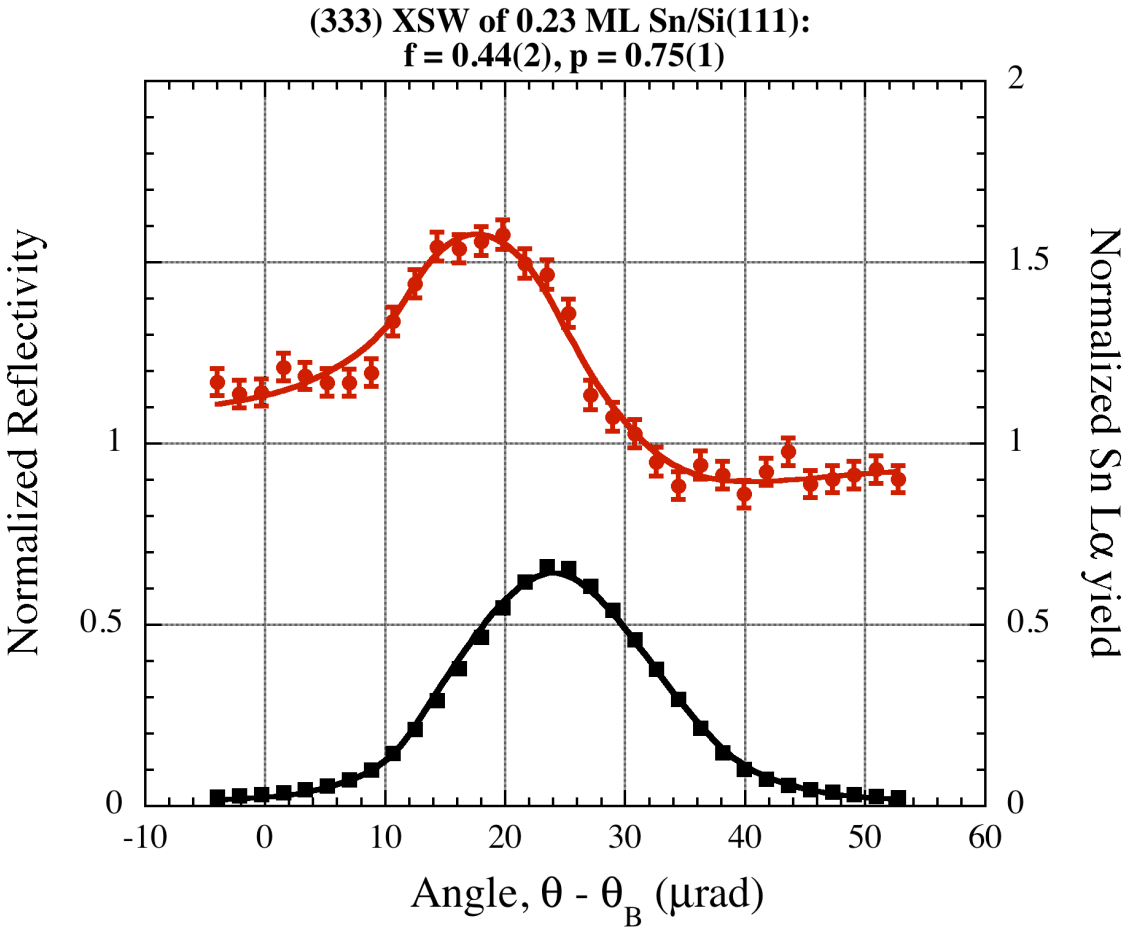

Figure 6.3: Reflectivity (closed squares) and normalized Sn Lα fluorescence yield (closed circles) experimental data along with theoretical fits (solid lines) for the (333) XSW measurement on 0.23(3) ML Sn/Si(111).

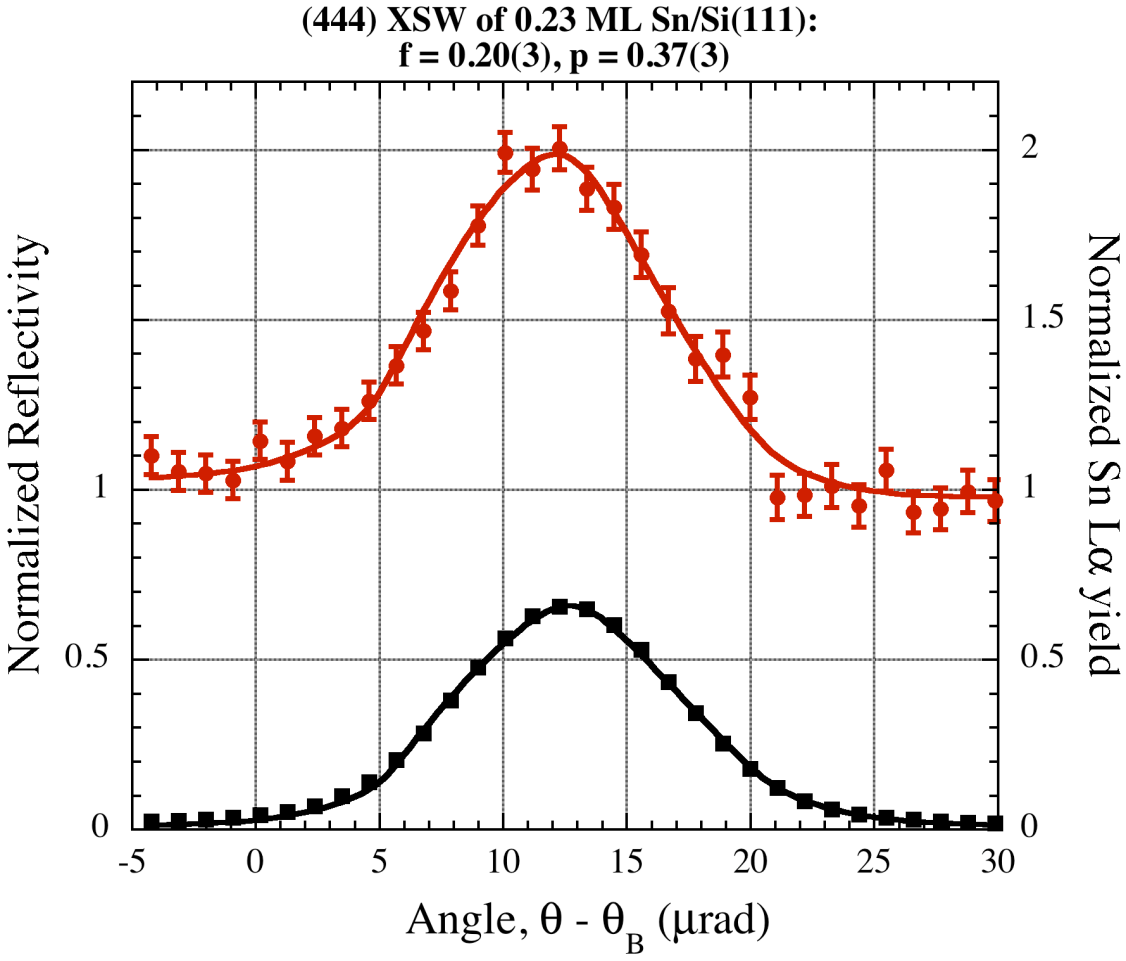

Figure 6.4: Reflectivity (closed squares) and normalized Sn Lα fluorescence yield (closed circles) experimental data along with theoretical fits (solid lines) for the (444) XSW measurement on 0.23(3) ML Sn/Si(111).

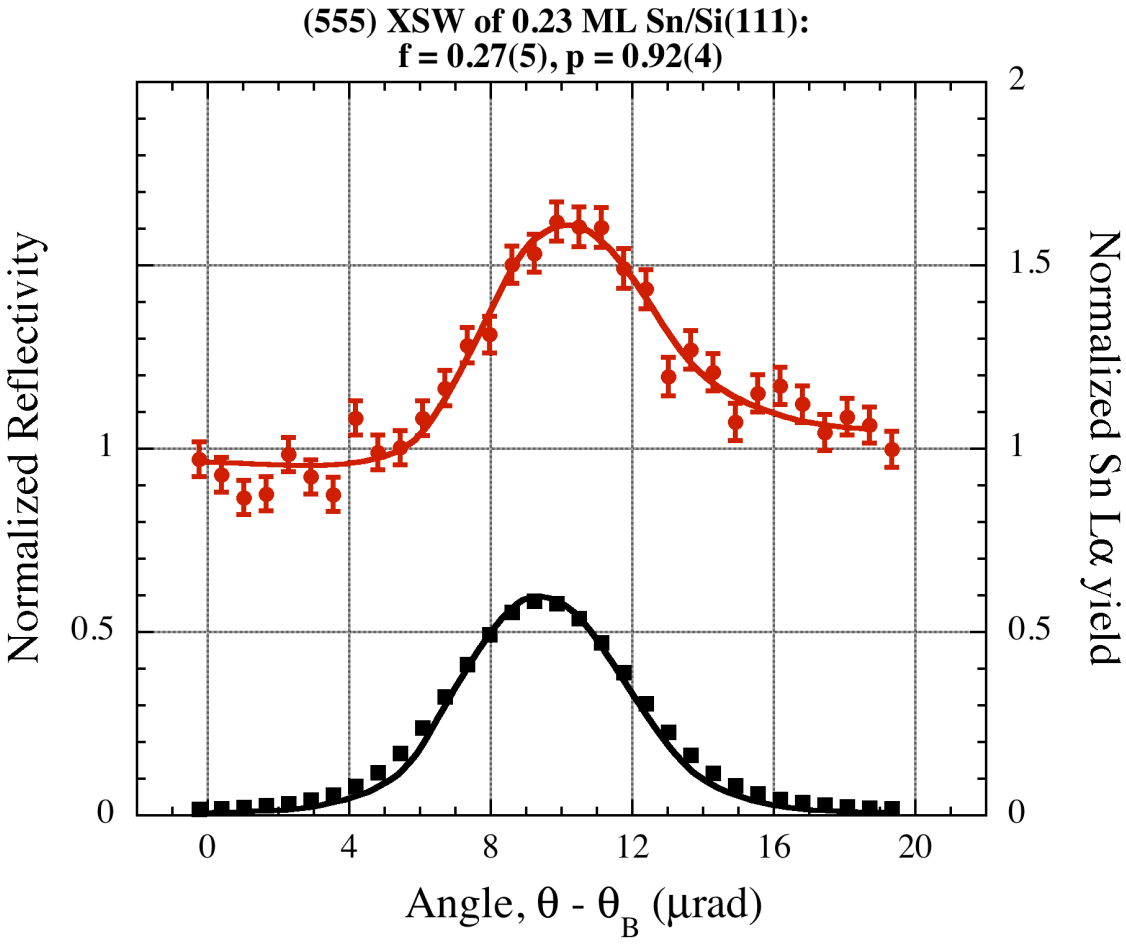

Figure 6.5: Reflectivity (closed squares) and normalized Sn Lα fluorescence yield (closed circles) experimental data along with theoretical fits (solid lines) for the (555) XSW measurement on 0.23(3) ML Sn/Si(111).

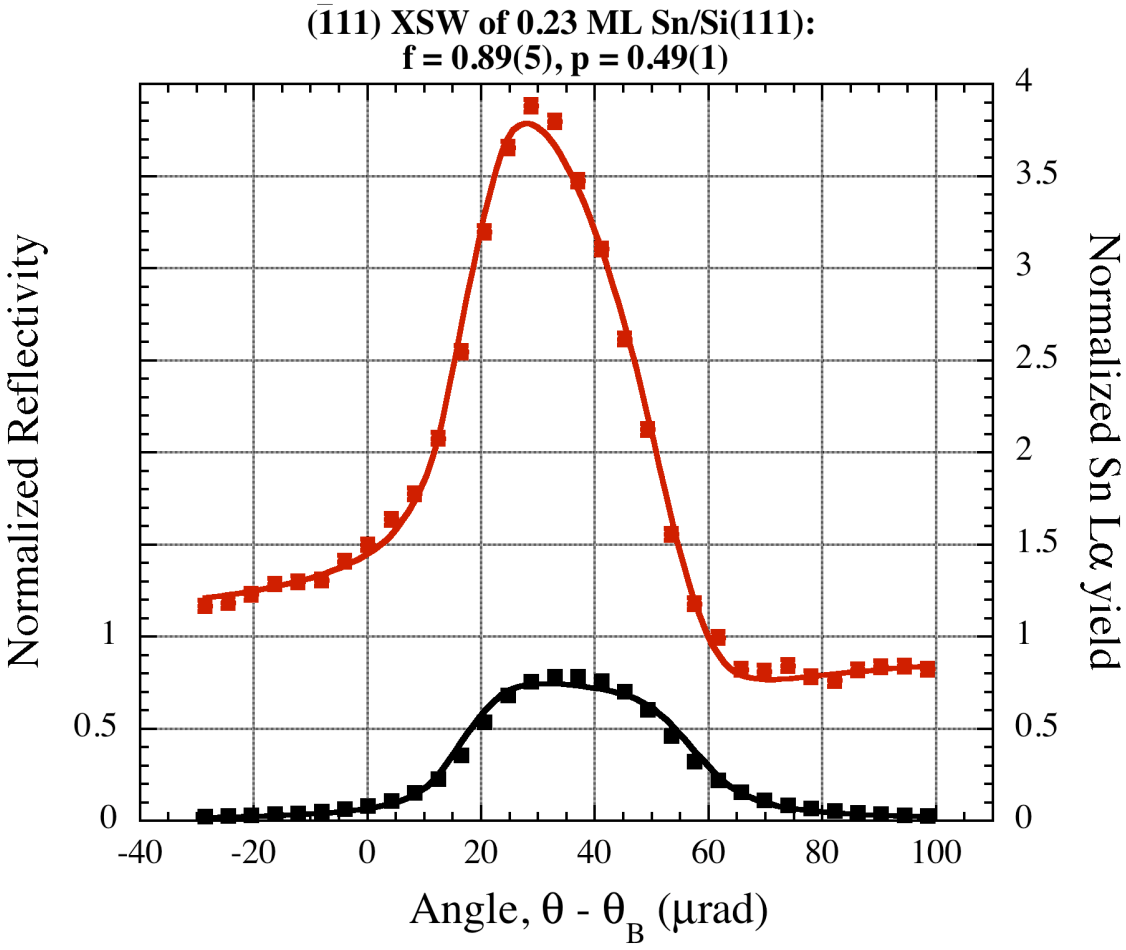

Figure 6.6: Reflectivity (closed squares) and normalized Sn Lα fluorescence yield (closed circles) experimental data along with theoretical fits (solid lines) for the ($\bar{1}11$) XSW measurement on 0.23(3) ML Sn/Si(111).

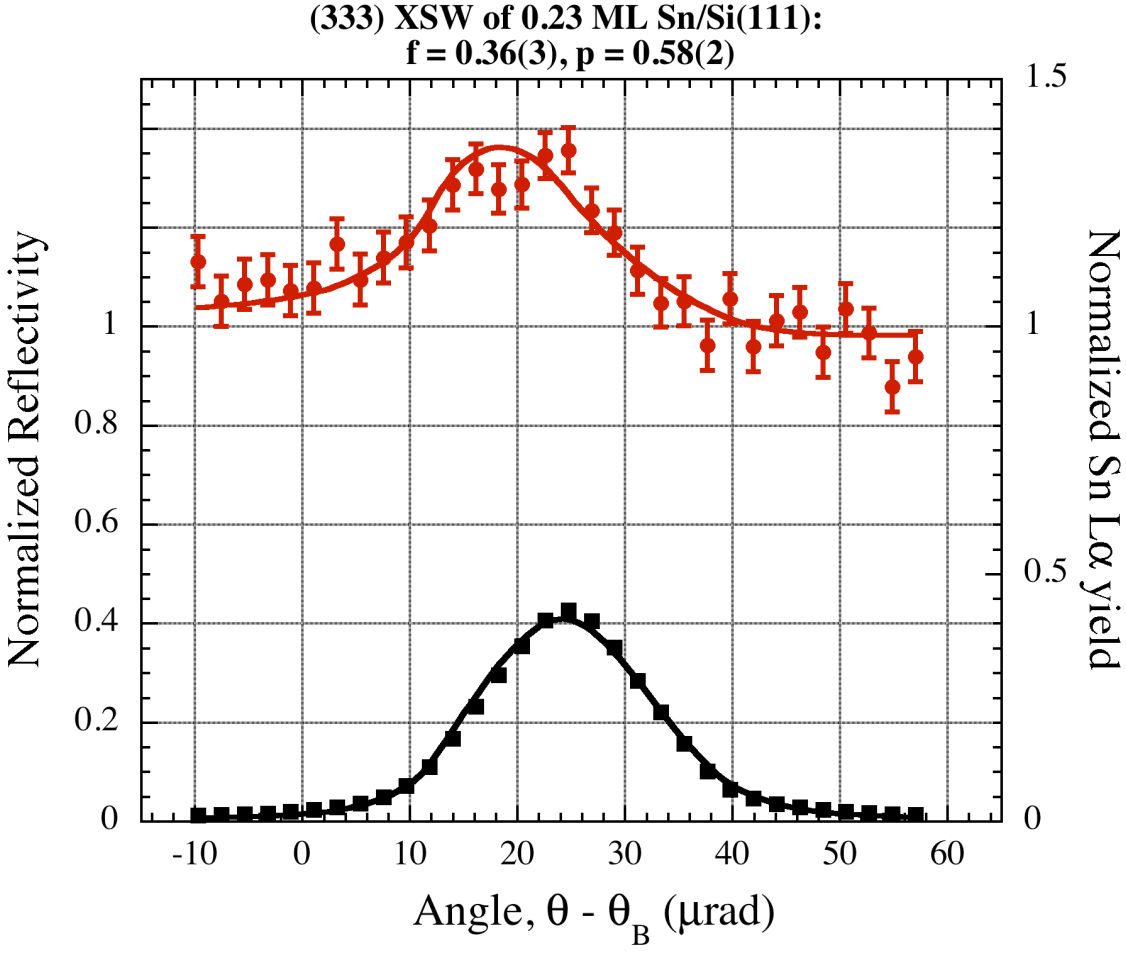

Figure 6.7: Reflectivity (closed squares) and normalized Sn Lα fluorescence yield (closed circles) experimental data along with theoretical fits (solid lines) for the ($\bar{3}$33) XSW measurement on 0.23(3) ML Sn/Si(111).

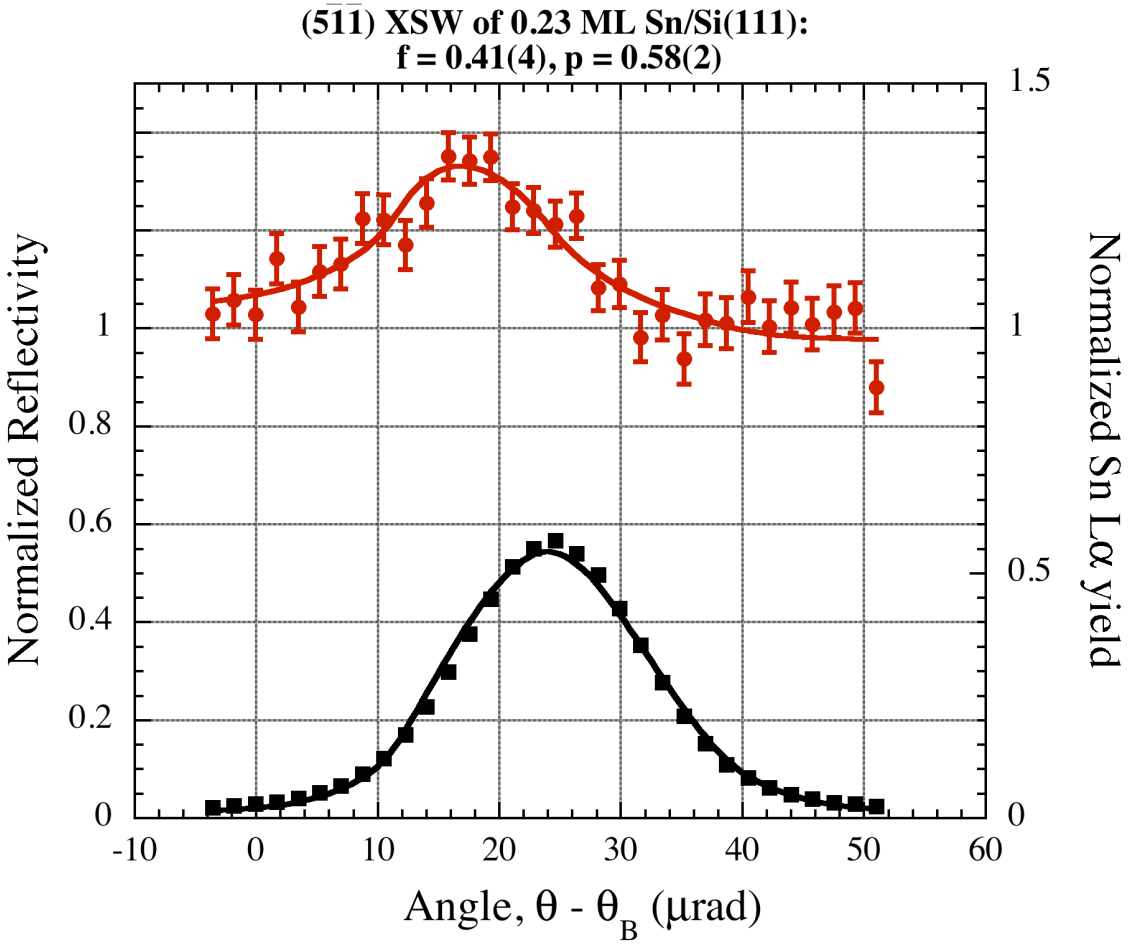

Figure 6.8: Reflectivity (closed squares) and normalized Sn Lα fluorescence yield (closed circles) experimental data along with theoretical fits (solid lines) for the (5 $\bar{1}$ $\bar{1}$) XSW measurement on 0.23(3) ML Sn/Si(111).

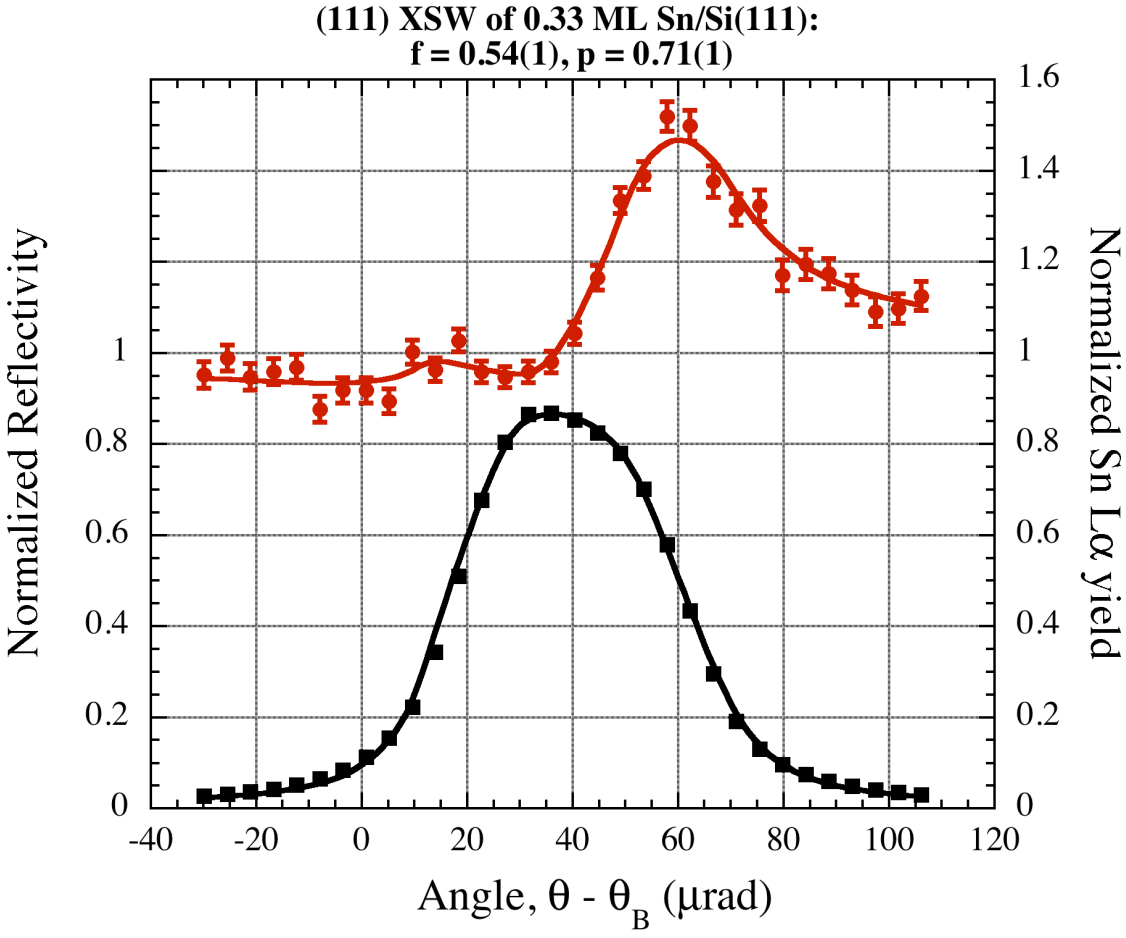

Figure 6.9: Reflectivity (closed squares) and normalized Sn Lα fluorescence yield (closed circles) experimental data along with theoretical fits (solid lines) for the (111) XSW measurement on 0.33(4) ML Sn/Si(111).

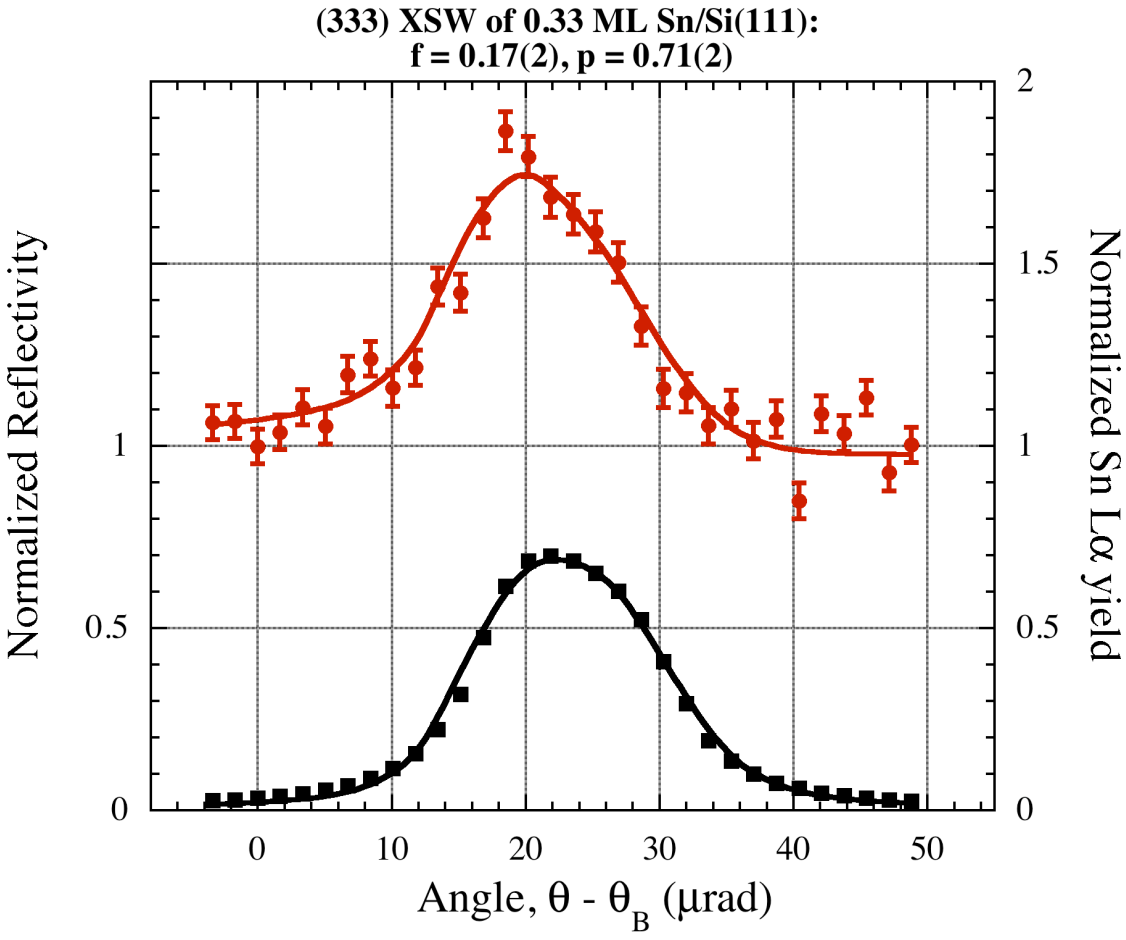

Figure 6.10: Reflectivity (closed squares) and normalized Sn Lα fluorescence yield (closed circles) experimental data along with theoretical fits (solid lines) for the (333) XSW measurement on 0.33(4) ML Sn/Si(111).

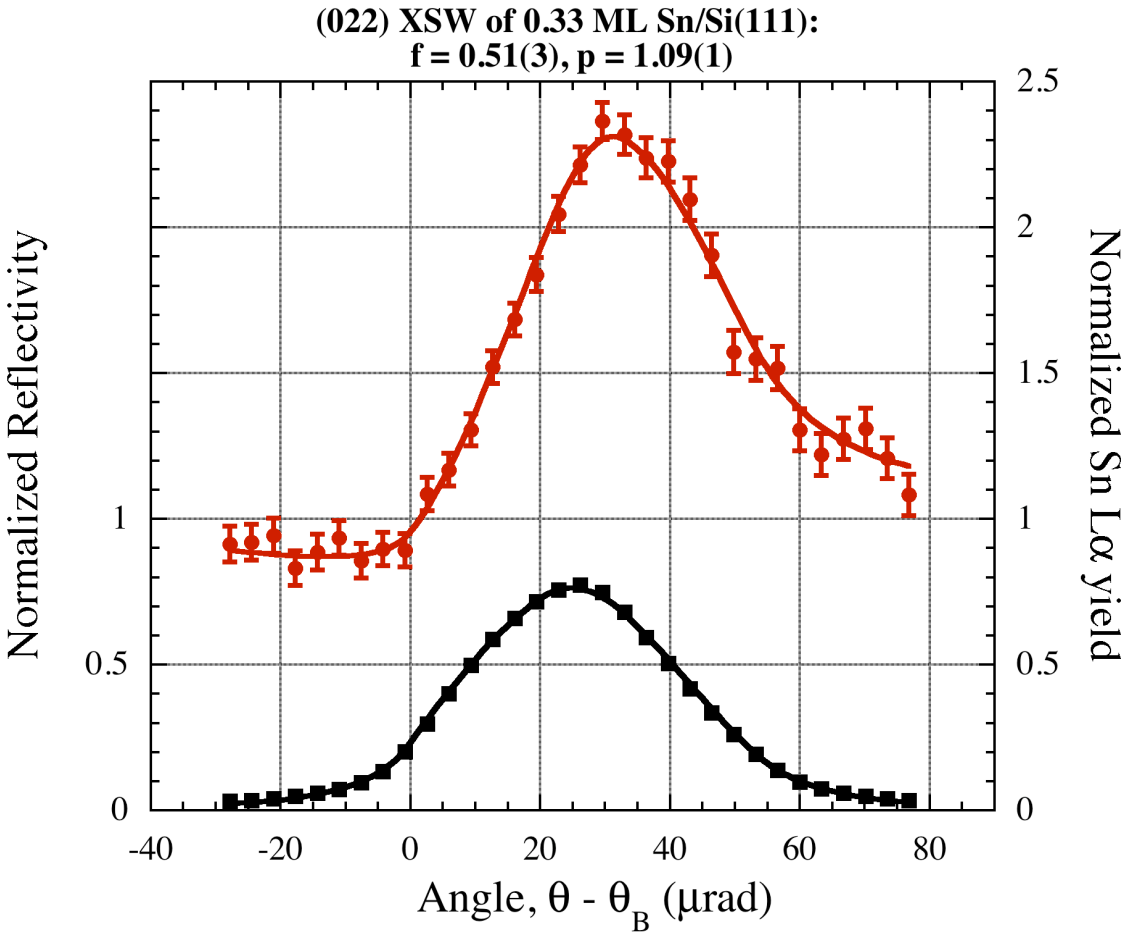

Figure 6.11: Reflectivity (closed squares) and normalized Sn Lα fluorescence yield (closed circles) experimental data along with theoretical fits (solid lines) for the (022) XSW measurement on 0.33(4) ML Sn/Si(111).

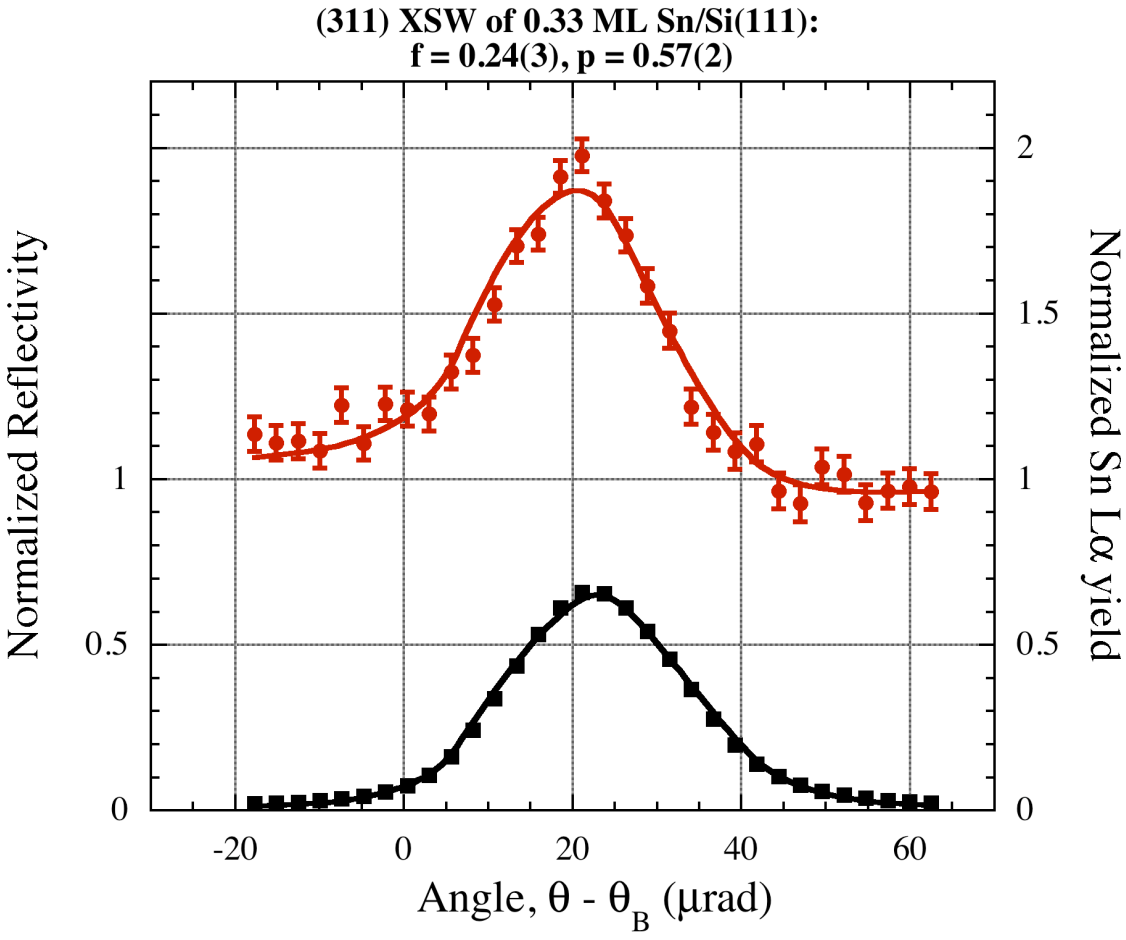

Figure 6.12: Reflectivity (closed squares) and normalized Sn Lα fluorescence yield (closed circles) experimental data along with theoretical fits (solid lines) for the (311) XSW measurement on 0.33(4) ML Sn/Si(111).

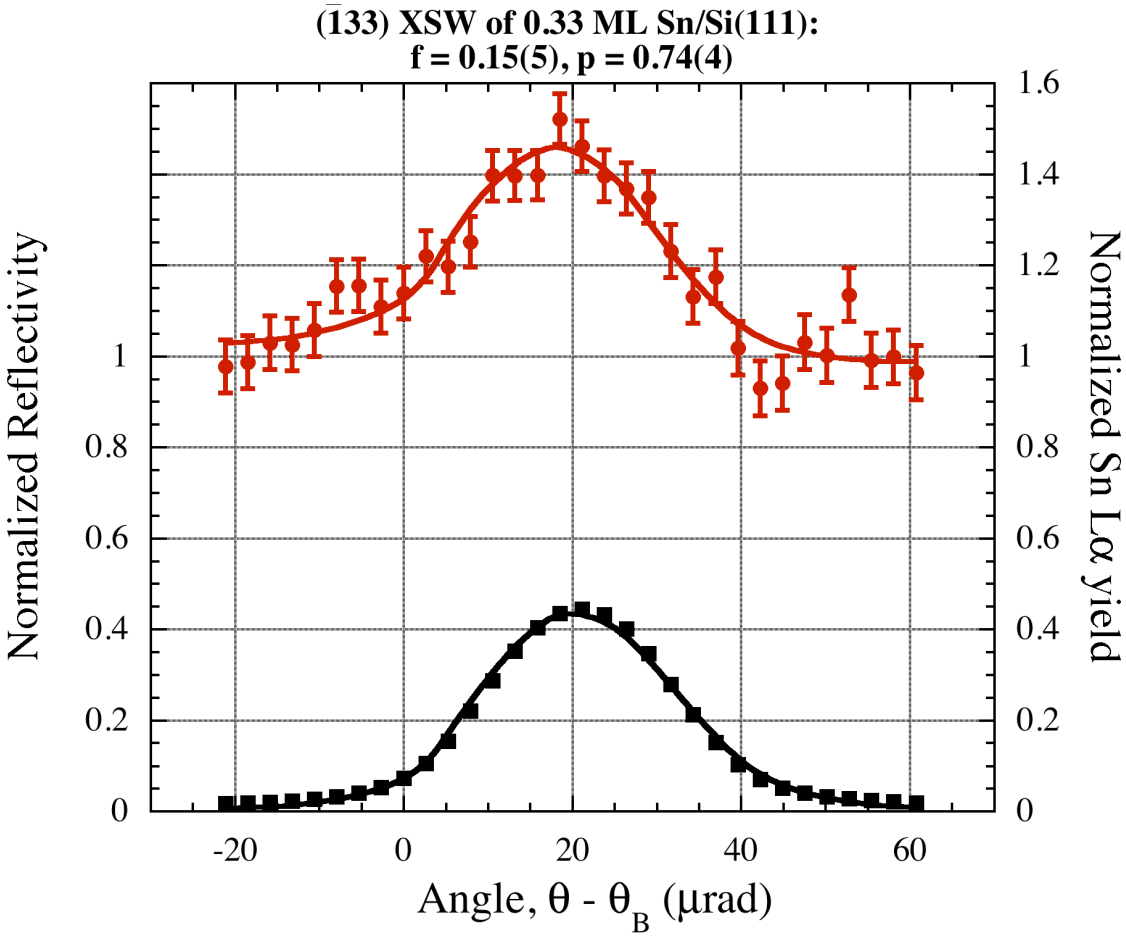

Figure 6.13: Reflectivity (closed squares) and normalized Sn Lα fluorescence yield (closed circles) experimental data along with theoretical fits (solid lines) for the ($\bar{1}$33) XSW measurement on 0.33(4) ML Sn/Si(111).

6.3 Results and Discussion of the 1/3 ML Sn/Si(111)-√3 Surface

6.3.1 XSW direct space imaging of the 0.23 ML Sn/Si(111)-(√3x√3) surface

In Section 4.4.3, it was explained how a direct-space image of the atomic density distribution for the fluorescent-selected atoms can be produced by a summation of the available XSW-determined Fourier components. By measuring a sufficiently complete set of Fourier coefficients, the collected XSW reciprocal-space data can be Fourier-inverted to generate a three-dimensional density map that is specific to the fluorescence-selected atoms and is independent of any presupposed structural model.

The direct-space Sn density distribution generated by the measured XSW parameters from Table 6.1 is shown in Figure 6.14. The resolution limit of this method corresponds to one-half of the smallest d-spacing measured, which in this case is $d_{555}/2$ = 0.31 Å. The top view shown in Figure 6.14(a) shows the Sn density variations at a height of 1.80 Å above the Si(111) surface (where the origin is chosen to be the top atom of the bulk-like Si(111) bilayer). This view demonstrates the maximum Sn atom density is centered at the T_4 adsorption site, as expected. This is confirmed by the XSW coherent position measurements agreeing with the relationships $P_{\bar{1}11}=(P_{111}+1)/3$ and $P_{\bar{3}33}=(P_{333}+1)/3$, which are the geometrical symmetry conditions for the occupation of T_4-adsorption sites on the Si(111) surface.

The side view shown in Figure 6.14(b) is a cross-sectional cut through the Sn density distribution containing the long diagonal of the (1x1) surface unit cell. While

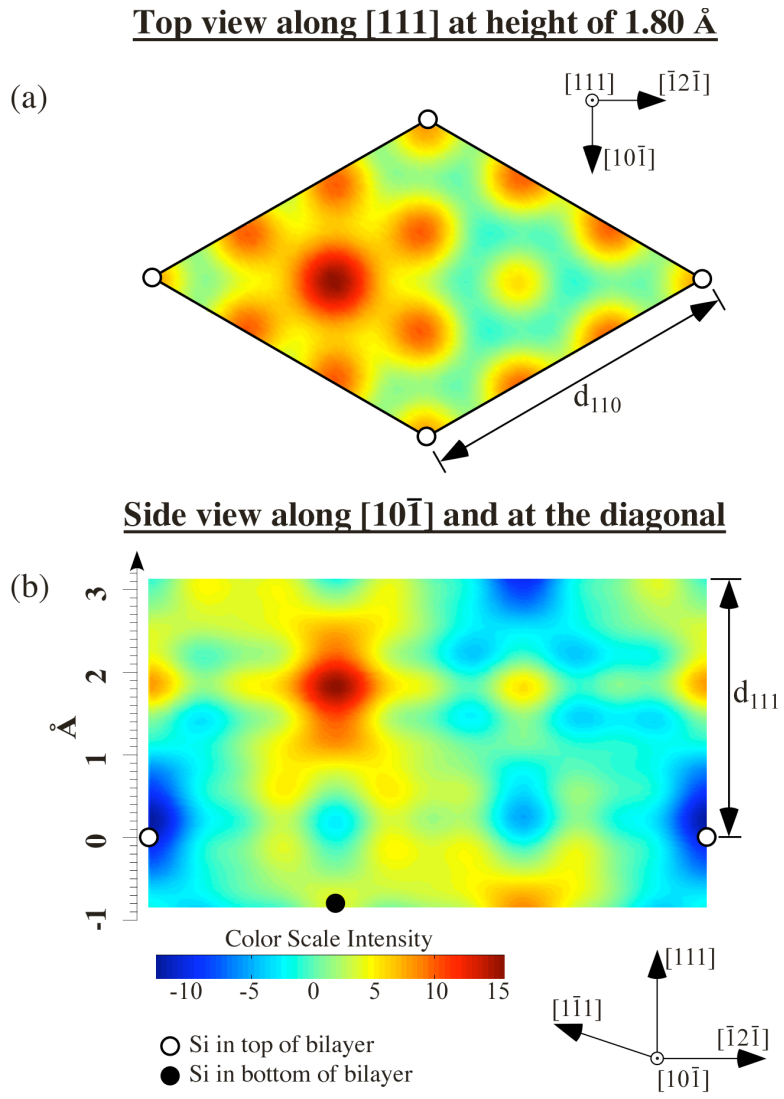

Figure 6.14: 2D cuts through the 3D XSW direct space Sn atomic density maps for the 0.23 ML Sn/Si(111) surface. The superstructure is projected into the primitive unit cell of the bulk crystal. (a) Top view of the (1 x 1) surface unit cell. (b) Side view of the (1 x 1) surface unit cell. Both 2D maps are positioned to cut through the maximum of the 3D Sn density map, which coincides with the T_4 adsorption site. The subsidiary maxima surrounding the T_4 site are artifacts due to the termination of the Fourier sum, which is confirmed via a comparison to the results of a forward calculation.

this view also shows the Sn occupies the T_4-adsorption site, there is no obvious vertical asymmetry or multiple density maxima, as would be expected for Sn adsorbed at multiple heights. The subsidiary density maxima that also appear in the direct-space image arise from the abrupt termination of the Fourier sum; this is confirmed by comparing the direct-space images shown in Figure 6-14 with the atomic density maps generated from the results of a forward calculation. In the forward calculation, a structural model under consideration is used to calculate the coherent fractions and positions for multiple sets of Bragg reflections. One set should encompass the set of *hkl*s used in the actual XSW experiment, while other sets should include additional XSW data derived from a subset of the Fourier components that were not experimentally acquired. These simulations then become the basis for a new Fourier sum and XSW direct-space image, which can then be compared with the experimentally-derived atomic density map. Therefore, this comparison helps answer the question of whether the density fluctuations that are visible in the XSW direct-space image are a result of the actual atomic-scale structure of the fluorescent-selected atoms or if they are simply artifacts of the Fourier inversion process.

The presence of only a single Sn density maxima can be interpreted in one of two ways: either the Sn is arranged in a flat, $\sqrt{3}$ structure as seen in STM images, or the Sn is in a "rippled" configuration with a separation between the Sn adatoms that is smaller than the 0.31 Å resolution of this XSW direct-space image. In order to

distinguish between these two possibilities, a comparison between the measured (*hhh*) coherent positions can be made to obtain a qualitative sense of the vertical distribution of the Sn atoms.

If the equilibrium state of the √3 surface is composed of Sn atoms at a single height, the time-averaged distribution of Sn, as projected along the [111] direction is symmetric, and it would be expected that the measured P_{111} and P_{333} would follow the relationship $P_{333} = Mod_1[\ 3P_{111}\ ]$. However, if one compares the results from the (111) and (333) XSW measurements, it can be seen that our measured value for $P_{333} = 0.75$ is less than $Mod_1[3P_{111}] = 3(0.61)-1 = 0.83$, which demonstrates the Sn atomic distribution is not consistent with the single height model suggested by earlier structural studies. In fact, relating the measured (111) and (333) coherent positions demonstrates the time-averaged projected Sn distribution is asymmetric and furthermore bottom-heavy. While the additional (*hhh*) XSW parameters will help refine the details of this asymmetric configuration, this simple comparison of two measurements immediately addresses the primary question concerning the 1/3 ML Sn/Si(111) surface structure: whether or not the RT Sn vertical distribution is flat or asymmetric. However, in order to precisely determine the structural details of this asymmetric Sn distribution, an appropriate model for the Sn/Si(111) surface can be employed to interpret the XSW results.

6.3.2 Conventional XSW analysis for the 0.23 ML Sn/Si(111) surface

While the XSW direct-space image of the 0.23 ML Sn/Si surface was not able to definitively determine the source of the asymmetric Sn distribution, analyzing the XSW data in a more conventional way may shed light on the geometric arrangement of the Sn adatoms. When analyzing the available XSW data in a traditional manner, the typical approach is to refer to a reasonable structural model, compare the experimentally determined XSW parameters with the model-derived XSW parameters, and use the results of the comparison to determine whether the model should be refined or discarded in favor of a new structural model.

One model that can be used for reference was developed in the XSW investigation of 1/3 ML Sn/Ge(111) discussed in Chapter 2 [19]. These XSW measurements concluded that the Sn atoms are located at the T_4-adsorption sites and favored a "one up, two down" structure at both RT and at 115 K. These same assumptions detailed in the earlier XSW study can also be used here: 1) one-third of the ordered Sn is located at a height h_A and the remaining two-thirds are at a height h_B, 2) the rms vibrational amplitudes $\langle u^2 \rangle^{1/2}$ along the [111] direction for all Sn atoms are identical, and 3) some fraction of Sn (1 - C) is randomly distributed, while the remaining fraction C is located at T_4 sites. As the direct-space images in the previous section show, this last assumption is a valid one.

In order to relate the measured amplitude *(f_H)* and phase *(P_H)* of the Hth Fourier coefficient (F_H) to the model parameters, the following equation is used:

$$F_m = f_m \exp(2\pi i P_m) = C[(1/3)\exp(2\pi i m h_A/d_{111}) + (2/3)\exp(2\pi i m h_B/d_{111})]\exp(-2\pi^2 m^2 \langle u^2 \rangle / d_{111}^2). \quad \textbf{(6.1)}$$

In this equation, *m* refers to the order of the *(hhh)* reflection of interest (*m* = 1,3,4,5). A global chi-squared minimization routine was used to integrate the four sets of XSW data, account for the relative errors for each individual XSW measurement, and calculate a set of model parameters. The fitting routine resulted in a structural model made up of a "one up, two down" configuration, with the up position at h_A = 2.04(5) Å above the top of the Si bulk-like layer and the down position at h_B = 1.78(3) Å. The vibrational amplitude for the Sn atoms in the [111] direction was calculated to be $\langle u^2 \rangle^{1/2}$ = 0.13(3) Å, while the Sn ordered fraction was C = 0.81(2). The reduced chi-squared value for this fit was 1.98.

With the Sn adatoms arranged in the configuration detailed above, the resulting Sn-Si bond length would be 3.01 Å for the top Sn atoms and 2.84 Å for the lower Sn atoms assuming Si were located at bulk-like positions. These distances, which are 10-17% larger than the sum of the Sn and Si covalent radii (2.58 Å), indicate a strong possibility of substantial Si relaxations. An earlier surface x-ray diffraction (SXRD) study of 1/3 ML Sn/Si(111)-√3 calculated that the adsorption of Sn produced considerable atomic relaxations within the first six sublayers of the Si substrate [18].

Similar vertical Si displacements were determined in an electron standing wave (ESW) structural study [25] and a theoretical full-potential linearized augmented plane wave (FLAPW) study [26]. In the SXRD investigation, it was calculated that the Si atoms within the first substrate layer experiences a lateral displacement of 0.211 Å towards the Sn adatom. Incorporating these relaxations with the XSW-determined Sn time-averaged distribution results in a more realistic estimate for the Sn-Si bond lengths (from 3.01 Å to 2.86 Å for the upper Sn atoms and from 2.84 Å to 2.68 Å for the lower Sn atoms).

Beyond providing a more realistic picture of the Sn bonding arrangement, significant Si relaxations may have other consequences as well. The SXRD study calculated a large strain energy of 2.29 eV per $\sqrt{3}$ surface unit cell due to the stretching of Si bonds [18]. Some of this strain energy may be relieved by the substitution of Sn from the adatom layer into the Si substrate. While this phenomena has not been directly observed by STM images of Sn/Si(111), STM images have shown Si can substitute for Sn atoms in the adatom layer [84]. Furthermore, small shifts of the Sn adatoms from the T_4 site were interpreted as the effect of substitutional Sn defects located in the first two Si layers. In the following section, it will be demonstrated how this Sn substitution phenomenon has been directly observed in the case of the XSW measurements of the 0.33 ML Sn/Si(111) surface.

(*hkl*) reflection	(111)	(333)	(022)	($\bar{1}$33)	(311)
f_H	0.54(1)	0.17(3)	0.51(3)	0.15(5)	0.24(3)
P_H	0.71(1)	0.71(3)	1.09(1)	0.74(4)	0.57(2)

Table 6.2: Summary of the XSW results for the 0.33(4) ML Sn/Si(111) surface. The unit cell origin coincides with the top of the bulk-like Si bilayer.

6.4 The Substitution of Sn within the Si Bilayer

The results of the XSW measurements collected on the higher-coverage, 0.33 ML Sn/Si(111) surface are shown in Table 6.2. As before, the coherent positions for the off-normal measurements can be compared with the (111) coherent position in order to deduce the in-plane geometry of the Sn atomic distribution. The applicable geometric symmetry relationships for Sn atoms located at T_4 sites are $P_{022}=(4P_{111}-1)/3$ and $P_{133}=P_{311}=(5P_{111}-1)/3$. The off-normal XSW measurements on the higher-coverage surface do not obey these requirements, unlike the previously discussed XSW results. Furthermore, a comparison of the (111) and (333) XSW measurements shows P_{333} = 0.71 to be much greater than Mod[$3P_{111}$] = 3(0.71)-2 = 0.13, indicating the Sn atomic distribution is markedly different than the one discussed earlier. Because a sufficient number of Fourier coefficients were measured on this higher-coverage Sn/Si(111)-√3 surface, the XSW direct space imaging technique can be used to qualitatively probe where this difference lies without reliance on a particular structural model.

The XSW direct-space image generated from the XSW parameters in Table 6.2 is shown in Figure 6.15. The increased in-plane width of the Sn atomic density distribution is partly due to the lower in-plane sensitivity of the off-normal XSW measurements made for this surface. Above the Si surface, this image is quite similar to the XSW direct-space image from the lower-coverage surface shown in Figure 6.14, since both images indicate a Sn atomic density maximum close to 1.80 Å above the top of the Si bilayer. However, the image in Figure 6.15 contains an additional Sn maximum that is approximately 25% less dense than the upper maximum. This lower density spot is located 0.35 Å below the bulk-like Si atoms at the top of the Si bilayer. The two maxima are separated by 2.15 Å, and therefore are easily distinguished from each other in the XSW direct-space image, which has an expected resolution of 0.52 Å ($d_{333}/2$). Both atomic density maxima are centered on T_4 adsorption sites; therefore, the image suggests the surface incorporated Sn replaces Si atoms located in the bottom of the surface bilayer.

In order to quantitatively determine the amount and location of the subsurface Sn, the previously discussed structural model can be modified by introducing two additional parameters: c_{sub}, the fraction of ordered Sn that has migrated beneath the Si surface, and h_{sub}, the depth below the top of the Si bulk-like bilayer where the Sn has diffused. One constraint imposed on the Sn population is the fraction of ordered Sn located at T_4 sites ($1 - c_{sub}$) is fixed in a 1:2 occupation ratio. The previously described

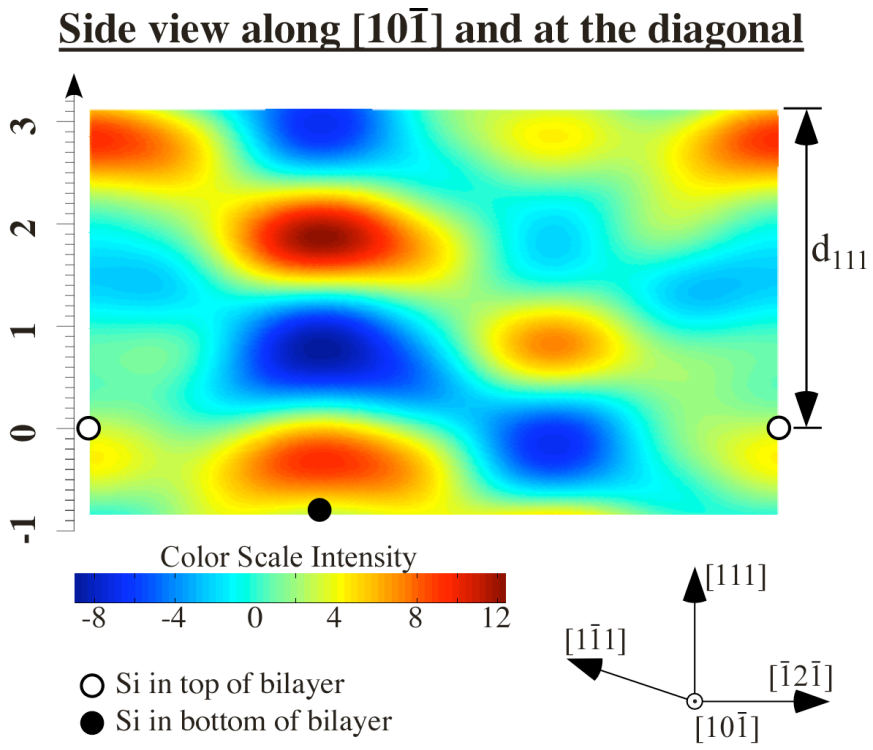

Figure 6.15: XSW direct space Sn atomic density image for the 0.33(4) ML Sn/Si(111)-√3 surface. While the majority of Sn appears adsorbed at the T_4 site, a significant amount appears to occupy a third site directly below the T_4 site within the Si surface. The other subsidiary maxima that are not located the subsurface site or T_4 site are artifacts due to the termination of the Fourier sum, which is again confirmed via the results of a forward simulation.

minimization routine can then be applied to the following equation for the *hhh* Fourier components:

$$F_m = f_m \exp(2\pi i P_m) = \mathrm{C} \times [[(1-\mathrm{c}_{sub})/3]\exp(2\pi i m h_A / d_{111}) + [2(1-\mathrm{c}_{sub})/3] \times \exp(2\pi i m h_B / d_{111}) + (\mathrm{c}_{sub})\exp(2\pi i m h_{sub} / d_{111})] \times \exp(-2\pi^2 m^2 \langle u^2 \rangle / d_{111}) \quad \textbf{(6.2)}$$

When fitting this revised set of equations to the XSW data in Table 6.2, the heights h_A and h_b as well as the thermal vibrational amplitude are fixed at the values determined from the previously discussed calculation (h_A = 2.04 Å, h_B = 1.78 Å, $<u^2>^{1/2}$ = 0.13 Å). After applying these constraints, the least-squares minimization routine returns a best-fit in which 38% (±3%) of the ordered Sn is located 0.37(4) Å below the top of the Si bulk-like surface. The fraction of Sn that is not randomly distributed is C = 0.81(4).

A similar analysis can be used to quantify the amount of subsurface Sn for the 0.23 ML Sn/Si(111) surface. Reevaluating the XSW data for this surface determined only a small amount of Sn (6±3%) of the ordered Sn is located 0.5(1) Å below the ideal Si surface. The inclusion of subsurface Sn in our surface model did not significantly affect the other structural parameters. The reduced chi-squared value for this fit was 1.87.

6.5 Discussion of XSW Results

To further assess if the chosen structural model for the 0.23 ML Sn/Si surface is reasonable, we can compare the measured Sn fluorescence yield modulation with

simulated Sn fluorescence yields based on our adsorption model. This comparison is shown in Figure 6.16, which depicts the simulated Sn fluorescence as a dashed line and the best fit to the measured Sn Lα fluorescence as a solid line. There is good agreement between the measured Sn fluorescence yield and the calculated yield curves; therefore, our structural model can be considered a reasonable description of the Sn atomic arrangement.

Our "one-up, two-down" surface model can also be compared to the results of previous investigations of the Sn/Si(111)-√3 surface. In one such study, Profeta *et al.* predicted that Sn occupies a single adsorption height of 1.80 Å with respect to the top of the Si bulk-like layer [26]. This study mentioned the possibility of multiple adatom heights. Another study by Yamanaka *et al.* used ESW to determine a single Sn adsorption height of 2.06 Å with respect to the top of the Si bulk-like layer [25]. However, it was also proposed that Sn could also be located in two inequivalent sites. Molecular dynamics simulations were used to calculate a vertical separation between two Sn sites of 0.3 Å. This calculation was used to reanalyze the ESW data, which produced a Sn height distribution with maxima at 1.96 Å and 2.26 Å, with the maximum at 1.96 Å being 30% larger than the upper maximum. Neither study addressed the possibility of Sn incorporation in the Si surface. These earlier single-height models are compared with our XSW results in Figure 6.17, which shows the calculated Sn fluorescence yield curves from the conclusions of Profeta *et al.* and

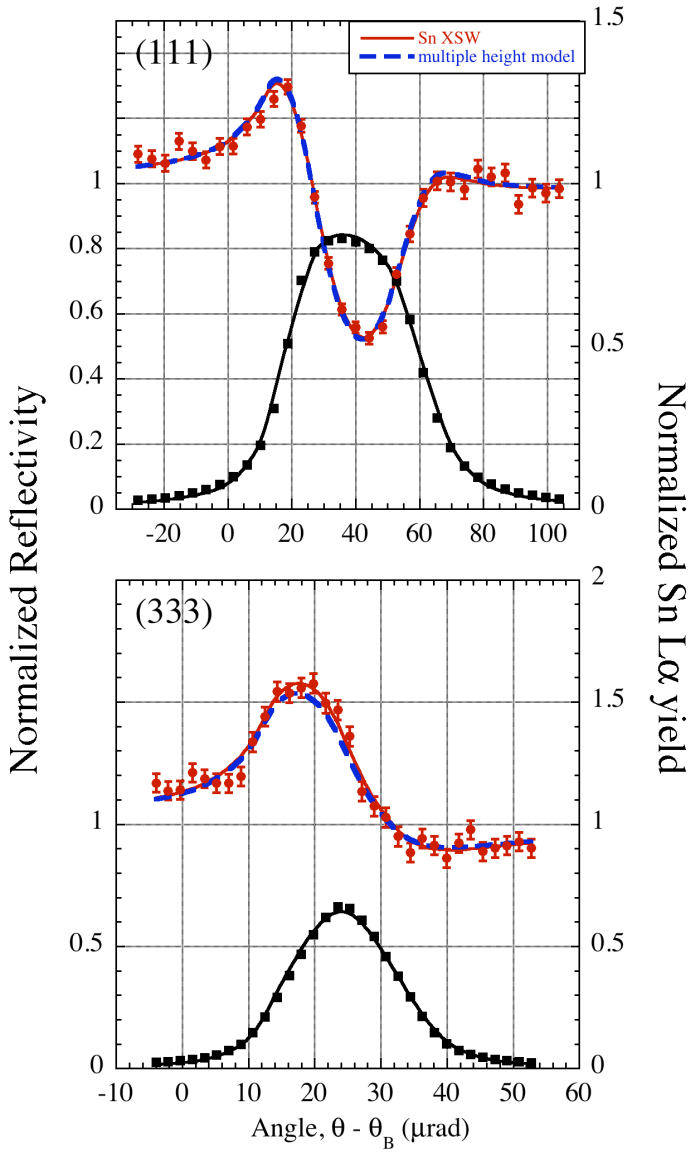

Figure 6.16: A comparison of the measured Sn Lα fluorescence yields for the (111) and (333) XSW measurements with calculated yield curves derived from the proposed multiple height structural model. The model used to predict the Sn fluorescence yield modulation involves a separation of 0.26 Å between two types of Sn adatoms in the √3 unit cell.

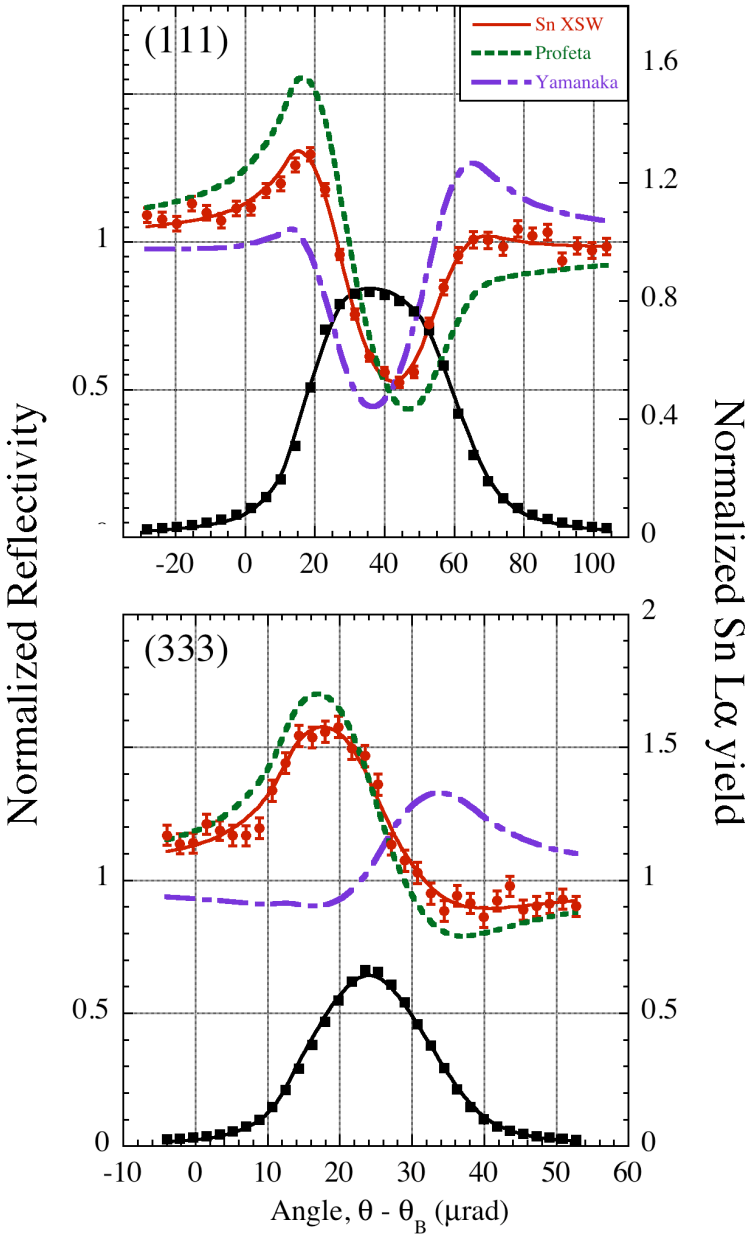

Figure 6.17: Another comparison of the measured Sn Lα fluorescence yields for the (111) and (333) XSW measurements with calculated yield curves derived from the results of Profeta *et al*. (dotted line), Yamanaka *et al*. (dot-dash line).

Yamanaka *et al*. as dashed and "dot-dash" lines, respectively. It is clear from this comparison that our multiple-adsorption height model best matches the measured Sn fluorescence yield from the 0.23 ML Sn/Si(111) surface.

It is also important to consider other possible explanations for the observed vertical Sn asymmetry other than the dynamical fluctuations model. First and foremost, we can consider the effect of the presence of defects in the Sn/Si(111) surface. In the specific case of the low coverage surface, the most obvious defect is the amount of Sn is smaller than the ideal 1/3 ML coverage. This raises the question of whether the asymmetric height distribution observed by XSW is caused by this reduced coverage. For Sn on Si(111), the √3 phase is stable over a wide coverage range (0.16 to 0.33 ML) [85], unlike in the Sn on Ge case. This is because Si adatoms will occupy the T_4 sites that would be filled by Sn adatoms if the coverage was closer to 0.33 ML. Therefore, instead of considering the effect of Sn surface vacancies on the observed Sn distribution, it is more useful to consider the effect of Si adatoms located in T_4 sites. A recent angle-resolved photoemission study examined the effect of Sn coverage on the electronic band structure of the $Si_xSn_{(1-x)}$/Si(111) √3 phase [32]. It found that the electronic structure is constant as a function of coverage in the 0.23-0.33 ML range, signifying the dangling bonds of the intermixed Si adatoms behave similarly to the Sn dangling bonds and there is no significant charge transfer between the two types of atoms. This finding suggests the influence of neighboring Si adatoms on the Sn vertical

distribution is small, as least from an electronic standpoint.

6.6 Summary

It has been experimentally determined that Sn adatoms are arranged in a "one up, two down" configuration, with one-third of the Sn at 2.04 Å above the top of the ideal Si bilayer and two-thirds at 1.78 Å. This Sn distribution is similar to the atomic distribution measured by XSW of the $\sqrt{3}$ phase and (3 x 3) phase of Sn/Ge(111). This similarity supports a dynamical fluctuations model of the Sn/Si(111) surface, in which Sn atoms move in a correlated fashion between two unique adsorption sites. This atomic arrangement presents an underlying (3 x 3) structure, as expected from previous core-level and valence-band photoemission studies and as observed in the isoelectronic 1/3 Sn/Ge(111) system. In a separate surface treatment, a higher initial coverage of Sn was deposited on Si(111). The measured Sn XSW Fourier coefficients were used to generate a model-independent 3D direct-space image, which unambiguously shows Sn migrating below the Si(111) surface and substituting for Si in the bottom of the surface bilayer.

Chapter 7: XSW Measurements of the 1/2 ML V/α-Fe_2O_3(0001) Surface

7.1 Sample Preparation

The sample treatments and XSW measurements for the 1/2 ML V/α-Fe_2O_3(0001) system were conducted in the UHV chamber/diffractometer located at the 5ID-C surface science endstation detailed in Section 5.3.2. The α-Fe_2O_3(0001) samples were purchased from Commercial Crystal Laboratories as a 1.0 mm thick polished wafer. The <0001> orientation of the sample was confirmed using a Laue apparatus and a four-circle x-ray diffractometer located at the Northwestern University X-ray facility. Samples whose crystallographic orientation exhibited a large miscut angle with respect to the sample surface were repolished to achieve a miscut less than 0.1°. After degreasing the hematite surface, the samples were attached to molybdenum sample platens (Thermionics, model # STLCP-1LR) via a set of molybdenum clips. The sample platens support the hematite samples and allow the rear face of the samples to be directly exposed to the manipulator filament for more efficient heating.

The clean α-Fe_2O_3(0001) surface was prepared by annealing the sample at 733 K for 1 hour under a stream of atomic oxygen, which is produced via an Oxford Applied Research Universal Thermal Cracker (model TC50). The cracker consists of a refractory capillary tube connected directly to a small vial of molecular oxygen. The O_2 gas is dissociated as it flows through the cracker tube, which is heated by an electron beam and water cooled to minimize outgassing. When used at its maximum power

rating (60 W), the ratio of atomic oxygen to molecular oxygen the oxygen source produces is 1.5 as measured by a residual gas analyzer. The chamber pressure during the production of atomic oxygen is maintained between 4.0 x 10^{-6} and 6.0 x 10^{-6} Torr during the annealing process and as the sample was allowed to cool down to room temperature. Because the capillary tube is directed toward the sample during the oxygen annealing, the actual oxygen partial pressure close to the sample surface is probably higher than the overall chamber pressure indicated by the ionization gauges. The atomic oxygen treatment produced a clean, well-ordered surface that exhibits a sharp (1x1) LEED pattern, as shown in Figure 7.1. The (1x1) surface is also expected to be free of carbon impurities, since previous XPS measurements on a similarly prepared surface detected no carbon contamination after a shorter period of oxygen annealing (30 min vs. 1 hr).

Once the clean α-Fe_2O_3(0001) surface was achieved, the preparation of the vanadium adlayer and its subsequent oxidation and reduction proceeded in three steps. After each step, the newly prepared surface was characterized using LEED and XSW in order to monitor the effect of each processing step on the atomic-scale structure. The first step involved the evaporation of vanadium onto the clean hematite surface at room temperature. The vanadium (99.9%, Goodfellow) was deposited using a high-temperature Knudsen cell that was set at a temperature of 1820 K, which resulted in a V deposition rate of 0.35 ML/minute. The sample surface was then oriented to be

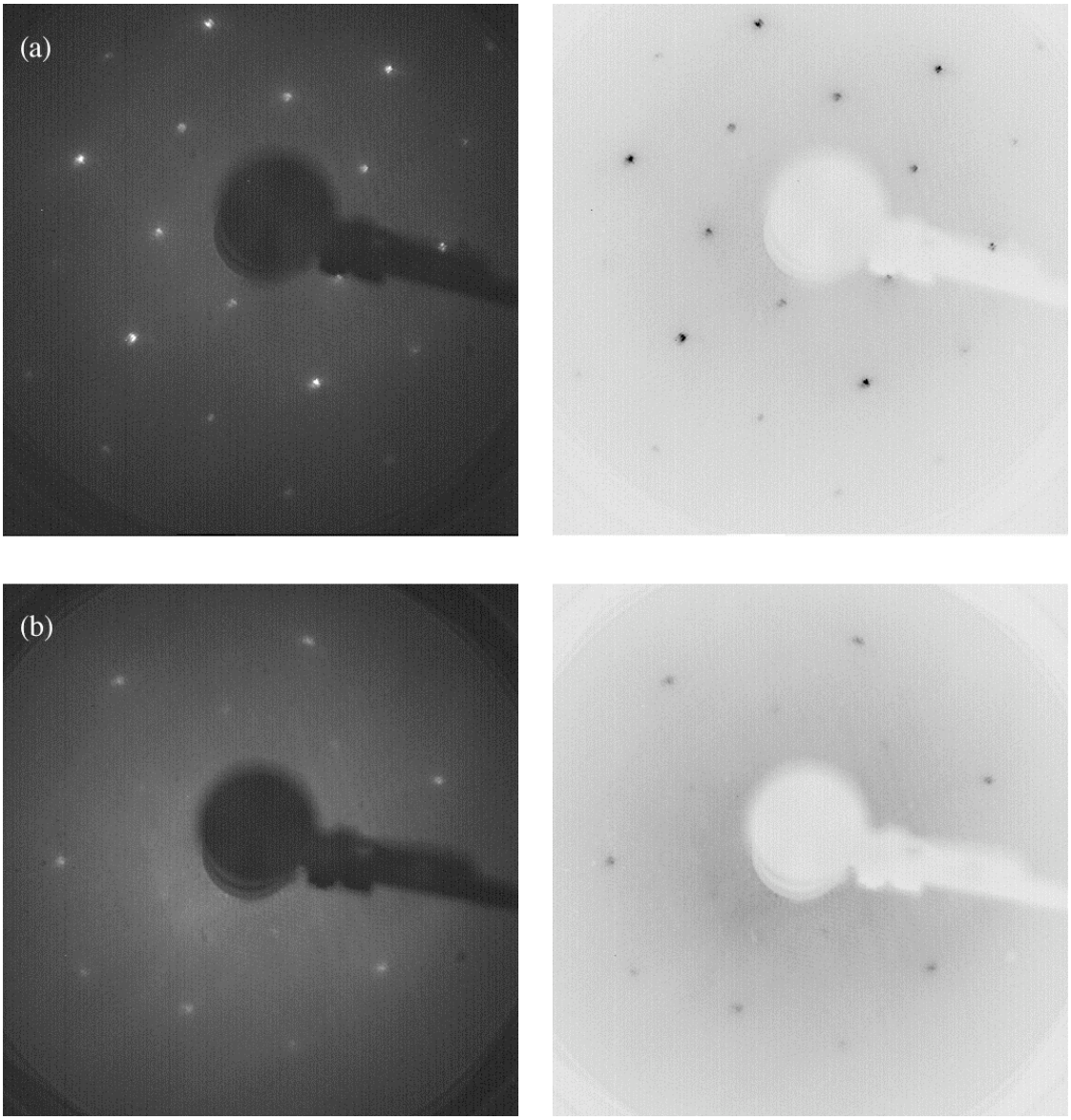

Figure 7.1: LEED images (as captured and inverted) for the clean, oxygen annealed Fe_2O_3(0001)-(1 x 1) surface (a) and the as-deposited 0.51 ML V/Fe_2O_3(0001)-(1 x 1) surface (b). Both LEED images used an incident electron beam energy of E=100.9 eV.

normal to the Knudsen cell and exposed to the vanadium flux by opening the Knudsen cell shutter for a period of 88 seconds, resulting in a vanadium coverage of 0.51 ML on the $Fe_2O_3(0001)$ surface. The total coverage was determined by measuring the vanadium coverage of a separate sample prepared under the same conditions using *ex situ* Rutherford backscattering spectroscopy (RBS). The estimated error in the areal density calculation is about 10% of the calculated value.

The LEED images of the as-deposited surface shown in Figure 7.1 demonstrate the unreconstructed (1x1) symmetry of the clean $Fe_2O_3(0001)$ surface has become obscured by the adsorbed vanadium surface layer. The sharp (1x1) diffraction spots of the clean surface have become noticeably weaker, and appear in front of a diffuse background with no discernible superstructure. In comparison, vanadium has a similar effect on the (1x1) LEED pattern of the clean $Cr_2O_3(0001)$ surface when deposited on the chromia surface [86], while in the investigations of the $V/Al_2O_3(0001)$ surface, there were no reports of LEED observations for the vanadium covered surface [86].

After conducting a set of XSW measurements for the as-deposited surface, the submonolayer vanadium was oxidized by exposing the surface to atomic oxygen. In preparing the vanadium oxide, the atomic oxygen source was operated at the same power settings used for the oxygen cleaning, while the oxygen partial pressure was maintained at 1.0×10^{-5} Torr. The vanadium surface was exposed to the atomic oxygen flow for 85 minutes. The oxygen exposure was conducted at room temperature to avoid

the possible interdiffusion of vanadium into the hematite substrate. Attempts to characterize the oxidized surface using LEED did not result in meaningful structural information due to the extreme charging of the oxide adlayer. Therefore, the experiment continued by conducting the same set of XSW measurements that were collected for the as-deposited surface, so that a direct comparison could be made between the vanadium and vanadium oxide surfaces.

After this second set of XSW data was collected, the vanadium surface was modified a final time by an exposure to atomic hydrogen. Hydrogen was chosen in order to reduce the vanadium oxide surface layer and therefore determine if the recovery of the electronic structure is accompanied by a change in the geometric structure. Atomic hydrogen was generated using the thermal cracker for a total of 60 minutes; during the first 15 minutes of the hydrogen exposure, the thermal cracker power was set to 60 W, while for the final 45 minutes the power was increased to 67 W. The measured chamber pressure due to the influx of atomic hydrogen was 2.0×10^{-5} Torr. After allowing the chamber pressure to recover from the increased pressure, the structure of the reduced vanadium oxide surface was again probed with XSW. However, due to time constraints, it was not possible to obtain the entire set of XSW measurements that was collected for the as-deposited and oxidized surface. Further details on the XSW measurements conducted for each of the three distinct surfaces will be given in the following section.

7.2 X-Ray Standing Wave Measurements

As previously mentioned, a specific set of XSW measurements was collected after each of the three separate surface treatments. For the as-deposited vanadium and the oxidized vanadium surfaces, the Fe_2O_3 (0006), $(10\bar{1}4)$, $(01\bar{1}2)$, and $(11\bar{2}3)$ Bragg reflections were employed to probe the vanadium atomic distribution. However, for the reduced vanadium surface exposed to atomic hydrogen, only the (0006) and $(10\bar{1}4)$ XSW measurements could be obtained in the remaining time allotted for the experiment.

Each XSW measurement proceeded by scanning the Fe_2O_3 single crystal substrate through the desired *hkl* Bragg reflection and simultaneously collecting the diffracted beam intensity and induced X-ray fluorescence spectra at each angular step of the rocking curve. The incident beam energy of 7.00 keV was chosen in order to prevent the excitation of a large Fe Kα fluorescence signal from the hematite substrate and the UHV chamber walls. As mentioned in Chapter 5, a single Si(022) channel-cut was used as the post-monochromator optic in order to maximize the x-ray flux incident on the sample. The increase in intensity was required because small slit apertures (typically 200 μm x 200 μm) were used to define the size of the incident beam, since illuminating small areas of the sample would usually result in narrower rocking curves. Another method that was used to improve the quality of the hematite rocking curve was

the use of an "x-ray eye" that was mounted on the detector arm. The x-ray eye was used to visually inspect the diffracted beam profile, and by adjusting the sample position laterally until the profile of the diffracted beam was as uniform as possible, the peak reflectivity and rocking curve width would typically improve.

A typical example of the x-ray fluorescence spectra collected from the as-deposited V/Fe_2O_3(0001) surface is shown in Figure 7.2(a). Ideally the fluorescence signal of interest (in this case, the V Kα peak at 4949 eV) should be situated away from other fluorescence lines present in the spectrum in order to facilitate the XSW analysis. However, if there are impurities in or around the sample, this situation can be impossible to achieve. In this case, the presence of Ti impurities gives rise to the Ti Kα fluorescence peak with an energy of 4508 eV located to the left of the V Kα fluorescence signal. Therefore, it can be expected that the V Kα peak would obscure the presence of a Ti Kβ fluorescence peak that sits underneath the dominant V Kα fluorescence signal. This is confirmed by examining the x-ray fluorescence spectrum of the clean Fe_2O_3(0001) surface, which is shown in Figure 7.2(b). The spectrum clearly shows the two emission lines characteristic of Ti K fluorescence, with the Ti Kβ yield located only about 20 eV from the position of the V Kα yield peak. Therefore, the contribution from the Ti impurities must be quantified and removed from the integrated intensity of the V Kα fluorescence peak in order to determine the correct modulation in

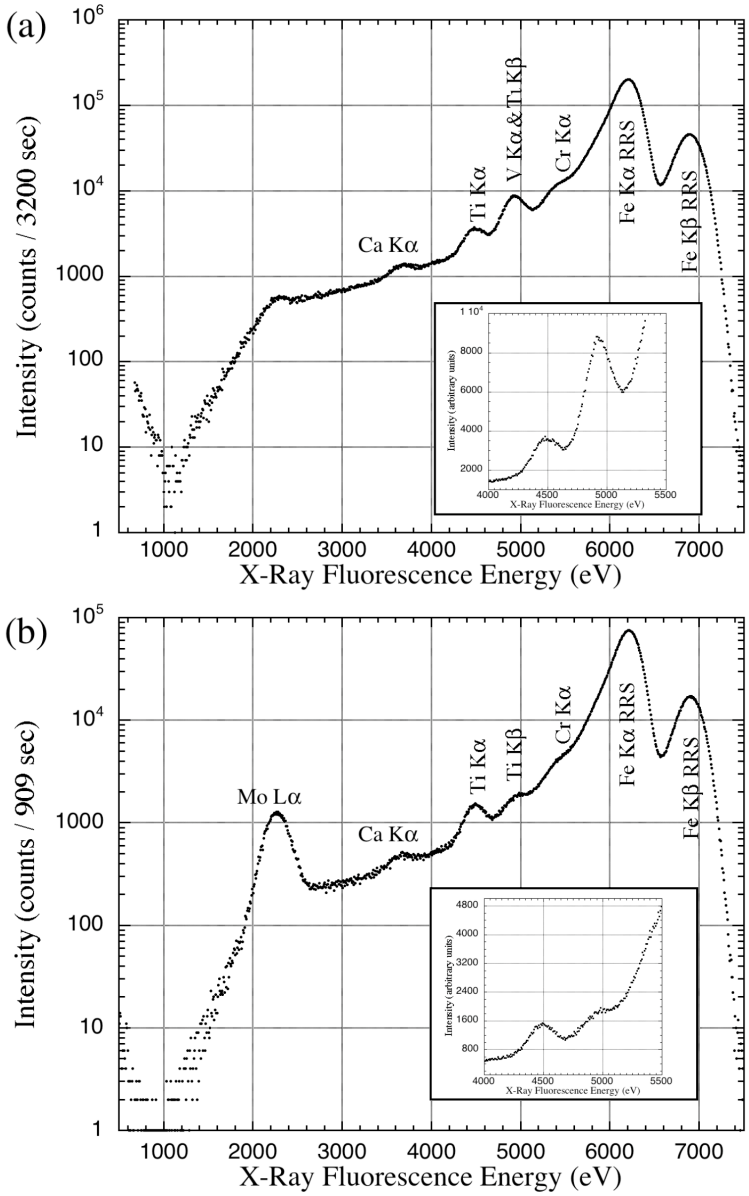

Figure 7.2: Angle-integrated X-Ray fluorescence spectra for (a) the 0.51 ML $V/Fe_2O_3(0001)$ surface and (b) the clean $Fe_2O_3(0001)$ surface. The presence of Mo in the clean Fe_2O_3 spectrum is due to the Mo clip holding the sample in place and does not affect the XSW results. The presence of Ti impurities and its proximity to the vanadium fluorescence signal can be seen in the two spectra. Also shown is the Fe resonant Raman scattering signals (RRS), which appear at an energy of $E_{K\alpha} - (E_\gamma - E_K^{Fe})$.

(*hkl*)	(0006)		(10$\bar{1}$4)		(01$\bar{1}$2)		(11$\bar{2}$3)	
	f_H	P_H	f_H	P_H	f_H	P_H	f_H	P_H
As-deposited	0.19(5)	1.04(3)	0.42(2)	0.30(2)	0.39(2)	0.22(2)	0.42(2)	0.75(2)
Atomic O exposure	0.22(5)	0.91(3)	0.39(3)	0.47(2)	0.27(4)	0.32(2)	0.25(3)	0.71(2)
Atomic H exposure	0.22(5)	1.02(5)	0.41(5)	0.29(2)	–	–	–	–

Table 7.1: Summary of the XSW measurements conducted on the various surface treatments on the 1/2 ML V/Fe_2O_3(0001) surface.

the V Kα fluorescence yield. This is performed by fitting both the Ti Kα and Kβ fluorescence peaks from the clean hematite substrate and noting the area ratio of the integrated intensities of the Ti Kα and Kβ yields; this information can then be used during the fits of the fluorescence spectra of the vanadium covered surface to remove the influence of the underlying Ti Kβ peak on the V Kα yield.

The result of this process is displayed in the plots of the vanadium XSW measurements shown in Figures 7.3–7.6, which show the measured reflectivity and V Kα fluorescence yield, as well as their theoretical fits, for each Bragg reflection collected for the as-deposited, oxidized, and reduced V/Fe_2O_3(0001) surfaces. By fitting the normalized reflectivity and the modulation in the fluorescence yield with dynamical diffraction theory, the coherent position (P_H) and coherent fraction (f_H) for the adsorbed V atomic distribution can be determined. A summary of the XSW parameters for the three surface preparations is shown in Table 7.1. The listed coherent positions are with

respect to the unit cell depicted in Figure 3.1, where a Fe atom is located at the fractional coordinates of (0.0, 0.0, 0.3553), while an O atom is located at the fractional coordinates of (0.3059, 0.0, 0.25). Note the origin of the unit cell does not coincide with any particular Fe or O atom.

7.3 Results and Discussion of the 1/2 ML V/Fe_2O_3(0001) System

7.3.1 General observations regarding XSW results

Unfortunately, as mentioned in Section 7.2, the surface exposed to atomic hydrogen was not characterized with the full complement of Bragg reflections used for the other two surfaces due to time constraints during the beamtime. However, if one examines the two XSW datasets that are available for comparison, the modulation of the V Kα fluorescence when scanning through the (0006) and $(10\bar{1}4)$ rocking curves are qualitatively very similar. More importantly, the values for the coherent fraction and position derived from these measurements are essentially the same. As a result, it is reasonable to suggest that these two XSW measurements are representative of the same vanadium surface structure. This hypothesis is supported by the XPS investigation detailed in Section 3.6, which determined the electronic structure of the as-deposited vanadium adlayer could be recovered after oxidation.

Therefore, there are two separate vanadium atomic distributions that will be discussed: the as-deposited and reduced vanadium surface, and the oxidized vanadium

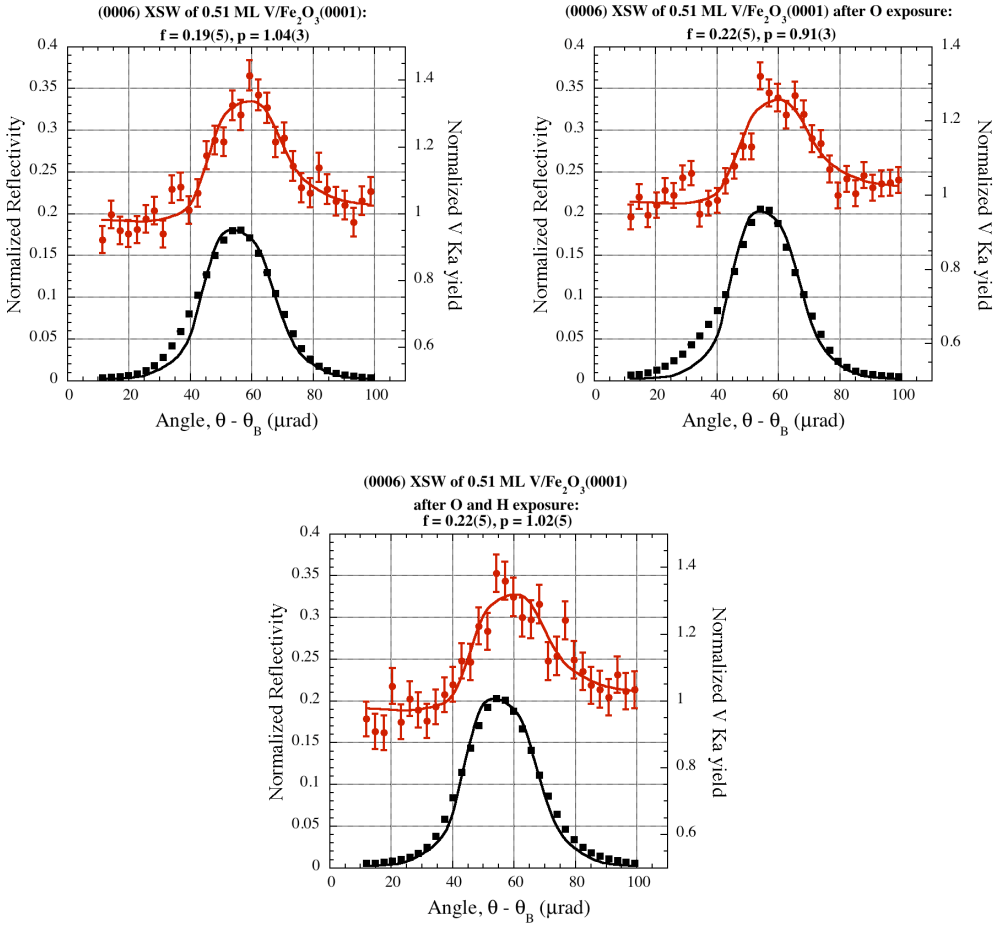

Figure 7.3: Reflectivity (closed squares) and normalized V Kα fluorescence yield (closed circles) experimental data along with theoretical fits (solid lines) for the (0006) XSW measurements on the as-deposited, oxidized, and reduced 0.51 ML $V/Fe_2O_3(0001)$ surfaces.

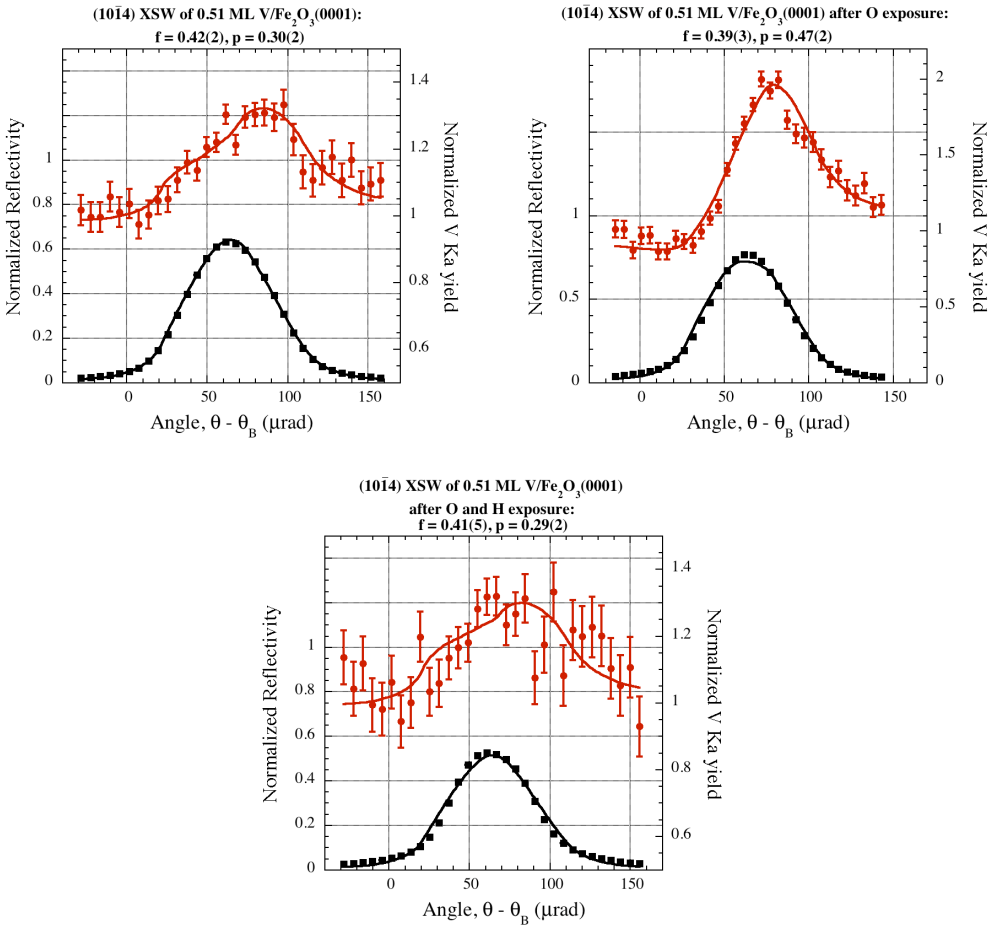

Figure 7.4: Reflectivity (closed squares) and normalized V Kα fluorescence yield (closed circles) experimental data along with theoretical fits (solid lines) for the (10$\bar{1}$4) XSW measurements on the as-deposited, oxidized, and reduced 0.51 ML V/Fe_2O_3(0001) surfaces.

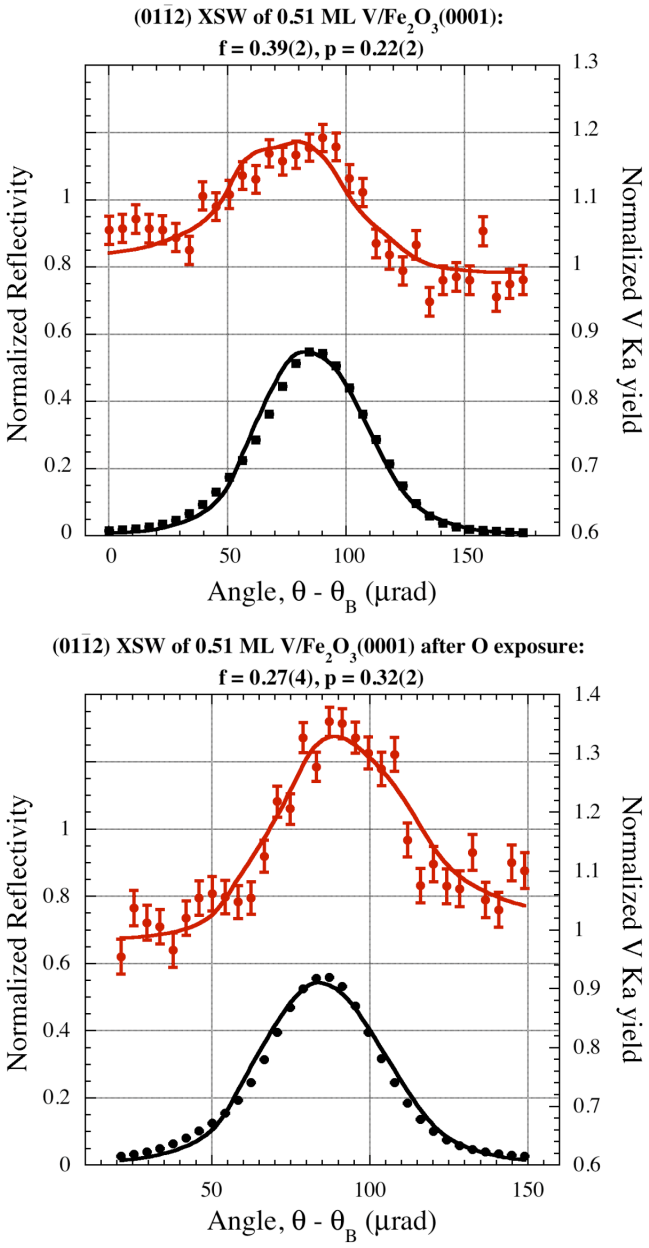

Figure 7.5: Reflectivity (closed squares) and normalized V Kα fluorescence yield (closed circles) experimental data along with theoretical fits (solid lines) for the (01 $\bar{1}$2) XSW measurements on the as-deposited and oxidized 0.51 ML V/Fe_2O_3(0001) surfaces.

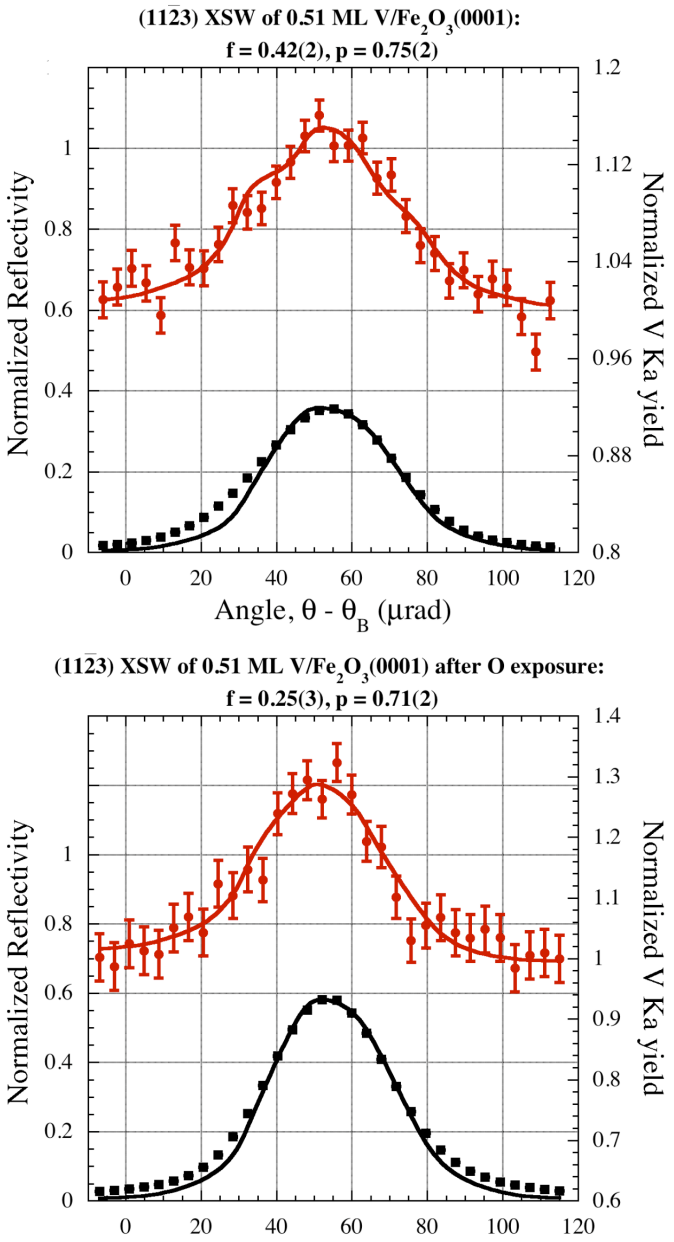

Figure 7.6: Reflectivity (closed squares) and normalized V Kα fluorescence yield (closed circles) experimental data along with theoretical fits (solid lines) for the (11$\bar{2}$3) XSW measurements on the as-deposited and oxidized 0.51 ML V/Fe_2O_3(0001) surfaces.

surface. This distinction can be justified by simply comparing the shape of the modulation of the V Kα fluorescence yields from the two different surface treatments. When focusing solely on the results of the (0006) XSW measurements, it seems as if the change in the V fluorescence yield modulation and the measured coherent fraction from P_{0006} = 1.04(3) for the as-deposited vanadium surface to P_{0006} = 0.91(3) after oxidation is small. This change in the coherent position corresponds to a reduction in the height of the ordered vanadium atoms of 0.30 Å if the vanadium atoms were to occupy a single unique adsorption site. However, when comparing the off-normal XSW measurements obtained for the two surfaces, it is clear that there is a significant change in the fluorescence yield modulation after the surface is oxidized. This marked change in the V Kα yield points to a definitive shift in the measured coherent positions and the lateral adsorption site arrangement as the vanadium is oxidized by the atomic oxygen exposure.

As described in Section 4.4.2, it is possible that if the vanadium atoms are located at a single atomic site, the collected normal and off-normal coherent positions can be combined to triangulate the position of the vanadium atoms. However, the measured coherent positions for the as-deposited surface do not definitively point at a single unique adsorption site; while the off-normal coherent positions of $P_{01\bar{1}2}$= 0.22(2) and $P_{10\bar{1}4}$= 0.30(2) for the as-deposited surface intersect at a location close to a bulk-like oxygen position above the iron bilayer, this intersection point does not coincide

with the coherent position for the (0006) XSW measurement. The same is essentially true for the oxidized surface, with the intersection of the off-normal coherent positions of $P_{01\bar{1}2}$= 0.32(2) and $P_{10\bar{1}4}$= 0.47(2) shifted upward from the bulk-like oxygen position by 0.6 Å. Although this triangulated position is somewhat closer to the normal coherent position of P_{0006} = 0.91(3), the three XSW measurements still do not triangulate to a unique three-dimensional atomic site.

It is possible that the low coherent fractions in the surface normal direction may point to a significant amount of disorder in the vanadium spatial distribution; it is also possible that the vanadium atoms may occupy multiple adsorption sites above the hematite surface, which would partly explain the low coherent fractions observed for the (0006) XSW measurements. However, it is unlikely that the vanadium cations are incorporated within the close-packed plane of oxygen atoms by substituting for a particular oxygen anion. This is because there is a large dissimilarity between the electronic state of the oxygen anions that occupy these sites and the electronic state of the adsorbed vanadium cations. It is difficult to imagine a scenario in which these vanadium cations could be coordinated with neighboring Fe^{2+} or Fe^{3+} cations and form a stable V/Fe_2O_3(0001) surface. However, the vanadium atoms could be located at locations near the bulk-like oxygen atomic sites if one assumes the planes of iron and oxygen atoms are displaced from their bulk-like positions due to the truncation of the bulk atomic geometry by the surface. Such surface relaxations for the clean

Fe_2O_3(0001) surface have been extensively studied by both theoretical and experimental means, as discussed in Section 3.3. It is clear that the vanadium spatial distribution in its metal and oxidized state is quite complex, and further analysis using the XSW direct-space imaging method may provide additional insight into the arrangement of the adsorbed vanadium atoms.

7.3.2 XSW direct space imaging for the 1/2 ML V/Fe_2O_3(0001) system

As described in Section 4.4.3 and demonstrated in the previous chapter, the experimentally determined XSW parameters can be treated as the measured Fourier components of the atomic density distribution of the fluorescent-selected atoms. Therefore, the measured Fourier amplitudes and phases listed in Table 7.1 for the as-deposited and oxidized vanadium surfaces can be combined with equation 4.48 to produce a three-dimensional representation of the vanadium atomic density distribution. Because the atomic density distribution is generated independently of any *a prioiri* structural information, the XSW-determined density distribution becomes useful in situations such as ours, where the XSW measurements do not identify a particular high-symmetry adsorption site, which suggests the vanadium adatoms may take on a more complicated adsorption geometry.

One way to visualize the spatial distribution function is shown in Figure 7.7(a), which represents the intersection of the three-dimensional density distribution with the

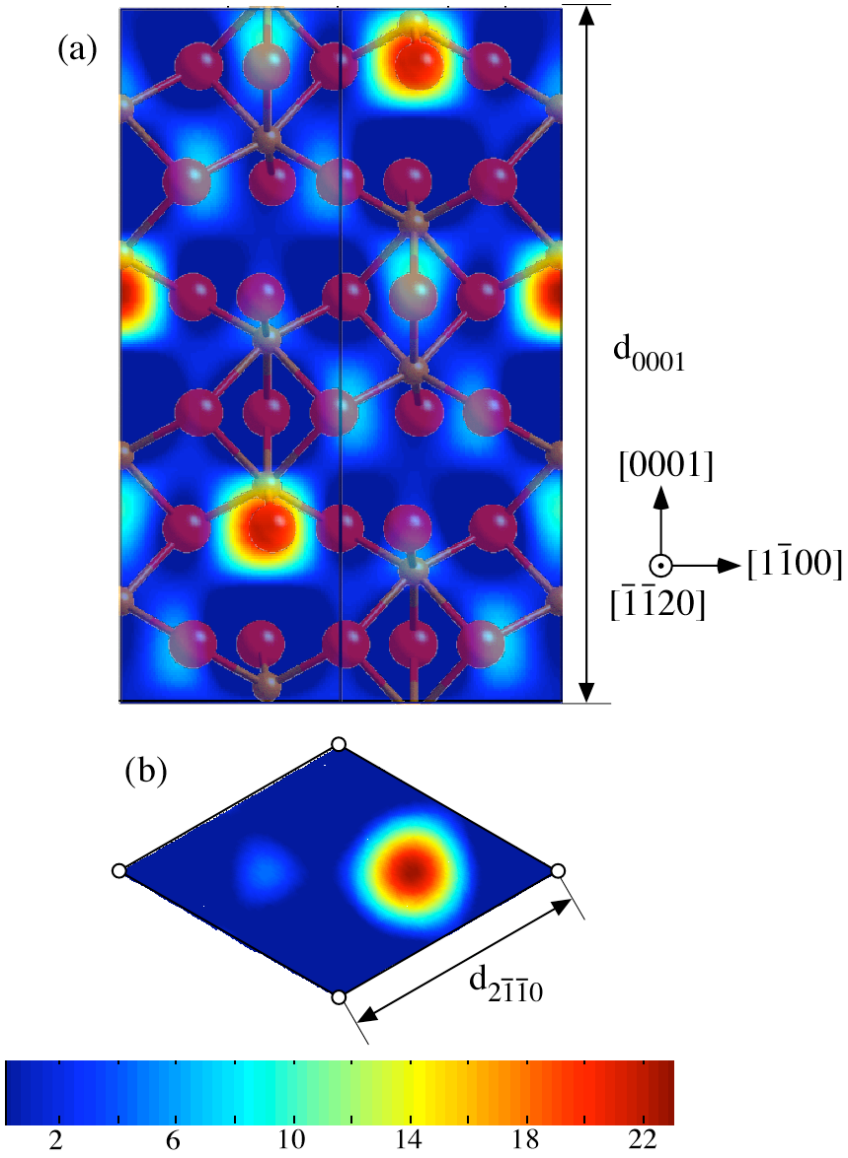

Figure 7.7: 2D cuts through the 3D XSW direct space V atomic density maps for the as-deposited 0.51 ML $V/Fe_2O_3(0001)$ surface. (a) Side view of the V density distribution through the long diagonal of the (1 x 1) surface unit cell. A reference model of the bulk hematite atomic-scale structure is superimposed on the atomic density map. (b) Top view of the (1 x 1) surface unit cell. This slice intersects the density distribution at a distance of 1.10 Å below the top of the hematite hexagonal unit cell.

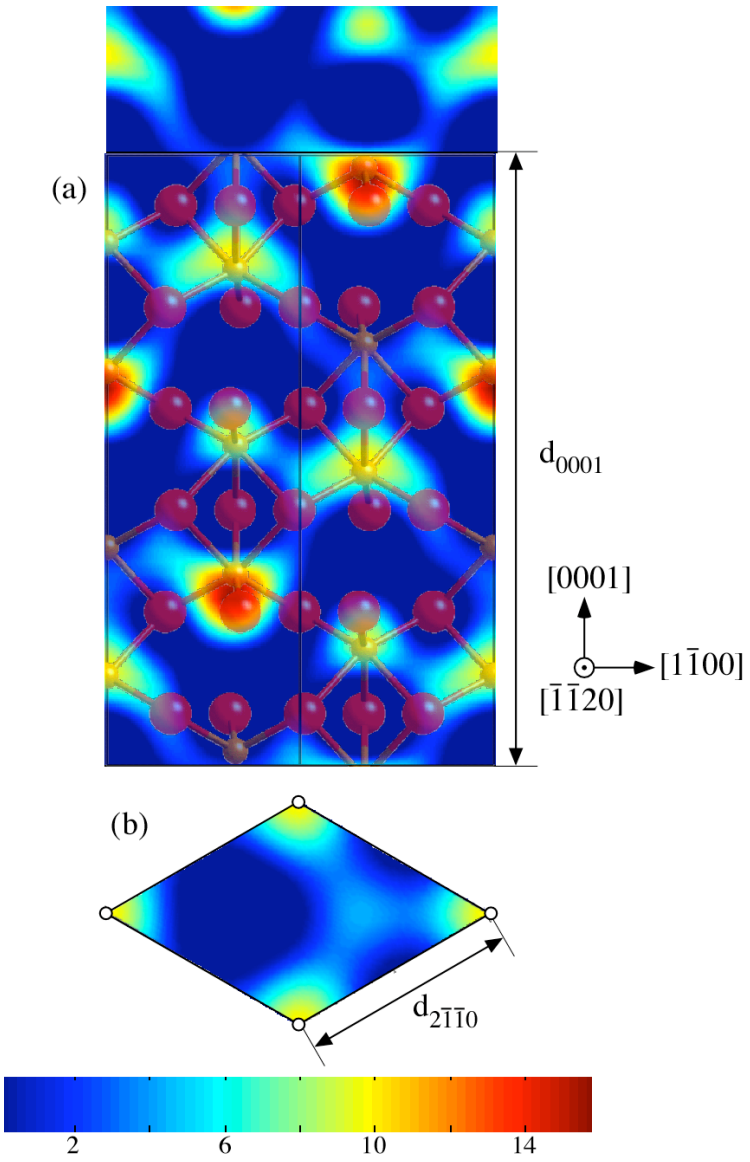

Figure 7.8: 2D cuts through the 3D XSW direct space V atomic density maps for the oxidized 0.51 ML V/Fe_2O_3(0001) surface. (a) Side view of the V density distribution through the long diagonal of the (1 x 1) surface unit cell. The lower section of the density distribution is reproduced and translated to the top part of the cross sectional cut to emphasize the location of the secondary V occupation site. (b) Top view of the (1 x 1) surface unit cell. This slice intersects the density distribution through the center of the secondary density maxima, which appears at a distance of 2.24 Å above the top of the hematite hexagonal unit cell.

$(11\bar{2}0)$ plane of the hexagonal Fe_2O_3 unit cell. Because the density map of both the as-deposited and oxidized surfaces employ the same Bragg reflections to generate the Fourier sum, the spatial resolution of each of the direct-space atomic density plots is the same and is equal to one-half of the smallest d-spacing measured ($d_{11\bar{2}3}$ = 1.10 Å). The bulk Fe and O atomic positions are shown on the density map as a ball-and-stick model overlaid on the direct-space image. It should also be noted that because the Fourier components used to generate the density function are limited to that of the substrate Bragg reflections, the image represents a projection of the distribution function into the primitive unit cell of the hematite crystal. Furthermore, because the Fourier sum must necessarily include only a finite number of terms, the premature truncation of the Fourier sum will be seen in the direct-space image as spurious density maxima. This was confirmed by generating the types of forward simulation density maps outlined in Section 6.3.1.

Figure 7.7(b) also shows another cross-sectional slice that coincides with the vanadium atomic density maximum, which appears at a distance of 1.10 Å from the top of the hematite unit cell. As the two views demonstrate, the adsorbed vanadium appears to occupy a single atomic position that lies within the basal plane of close-packed oxygen atoms, as suggested by the partial triangulation of XSW measurements. While several density maxima appear in the side view, each of the vanadium maxima are symmetrically equivalent to one another and should not be interpreted as the presence

of multiple adsorption sites. While the atomic density maxima do appear near the plane of oxygen anions, it is also located directly below a bulk-like iron atomic site. This lends credence to the possibility that the vanadium adatoms occupy positions similar to that of the iron cations in the $Fe_2O_3(0001)$ selvedge.

This atomic geometry is not surprising, since if vanadium adatoms substituted for Fe cations in octahedral sites, the arrangement of the vanadium adatoms would mimic the corundum structure of the hematite substrate, as would be expected for a surface layer composed of V^{3+} cations. The vanadium +3 oxidation state was observed in the XPS measurements detailed in Chapter 3 [69]. An analogous arrangement has also been predicted for thin vanadium oxide films supported on α-$Al_2O_3(0001)$; using DFT calculations, Brázdová *et al*. proposed a model in which Al atoms in the alumina surface layer are replaced by vanadium [87]. However, the location of the density maximum in the XSW direct-space image suggests that as the vanadium adatoms bond with the oxygen layer underneath, this strong interaction is accompanied by atomic relaxations normal to the $Fe_2O_3(0001)$ surface.

As previously mentioned, it has been predicted that the clean $Fe_2O_3(0001)$ surface can experience such stabilizing atomic relaxations. For example, some theoretical studies of the Fe-terminated surface predict that the interlayer spacing between the topmost iron layer and the next oxygen layer can decrease as much as 41 [40, 41, 43] to 57 percent. In an XPD experiment of the Fe-terminated surface,

Thevuthasan *et al.* measured interlayer relaxations that are consistent with those predicted by theory [46]. The deposition of vanadium on the hematite surface may result in more extensive atomic relaxations, since the high oxygen affinity of vanadium may induce the migration of lattice oxygen near the surface layer the hematite towards the adsorbed vanadium. It has also been demonstrated that the adsorption of vanadium induces a reduction of the hematite substrate, producing a mix of Fe^{2+} and Fe^{3+} cations at the $Fe_2O_3(0001)$ surface [69]. It is reasonable that such changes would only further the extent of any structural deviations of the surface from the bulk Fe_2O_3 arrangement (as compared to the clean $Fe_2O_3(0001)$ atomic geometry). Unfortunately, the XSW technique as described here is unable to provide any information regarding the structure of Fe–O_3–Fe–Fe layers that make up the selvedge, so we are unable to quantify any surface relaxations in the iron or oxygen layers due to the adsorption of vanadium. However, judging from the position of the vanadium density maximum in the direct-space image, it is reasonable to suggest that any resulting surface relaxations experienced by the as-deposited surface would be similar to those predicted for the clean hematite surface.

7.3.3 XSW direct space imaging for the oxidized V/$Fe_2O_3(0001)$ system

Turning now to the oxidized surface, when the analogous direct-space density maps are generated the vanadium atomic distribution exhibits a significant change. As

shown in the side view presented in Figure 7.8(a), the original vanadium density maximum has shifted upward by 0.39 Å, taking on a position close to the bulk-like iron position. The shape of the high-density region has also become more asymmetric and bottom-heavy. More importantly, a second density maximum appears at the edge of the cross-sectional plane near the bulk-like Fe atomic site. This position is symmetrically inequivalent to the site in which the majority of the vanadium is found, suggesting that some of the vanadium atoms shift to an additional position after exposure to atomic oxygen. The shape of this second maximum is asymmetric as well, and it seems to mirror the spatial extent of the primary density maximum. Furthermore, as demonstrated by the top view of Figure 7.8(b), the asymmetry of the secondary density maximum is exhibited not only in the surface normal direction, but also in the surface plane. A possible source of this lateral asymmetry will be explored in further detail. An analogous view of the primary density maxima (not shown) is quite similar in appearance to the sole density maxima of the as-deposited surface.

The observation of a second density maximum suggests that as the atomic oxygen interacts with the vanadium adlayer, some of the oxidized vanadium atoms migrate to a second position. This adsorption site seems to coincide with the bulk-like Fe site located at the corner of the hexagonal hematite unit cell. The minority vanadium occupation site appears at a height of 2.24 Å, while the primary vanadium maximum is located at a depth of 0.72 Å below the top of the hematite unit cell. As the density map

of the secondary density maxima clearly shows, the oxidized vanadium atomic density extends laterally from the high symmetry sites of the hexagonal unit cell and reflects the three-fold symmetry of the hematite surface. Given that the vanadium adatoms occupy these two Fe-like sites after the vanadium is oxidized, it is important to understand the structural details of this multiple site geometry, as well as how this atomic arrangement is related to the electronic structure adopted by the oxidized vanadium [69].

In previous studies of supported vanadium oxides, it has been suggested that after calcinating a synthesized vanadium oxide to remove adsorbed water molecules, the vanadium is oxidized primarily to the +5 oxidation state. The atomic-scale structure of these vanadium oxides have been characterized as isolated VO_4 units when the vanadium loading is low or as polymeric VO_4 chains when the loading is increased. The isolated units include one terminal V=O bond and three V–O–support bonds, but as the vanadium coverage increases, two of the V–O–support bonds are replaced by two bridging V–O–V bonds [49]. These configurations are shown schematically in Figure 7.9.

The structure of the isolated VO_4 unit is similar to the termination that has recently been proposed for certain $Fe_2O_3(0001)$ surfaces [43, 88]. In this surface structure, an oxygen atom bonds about 1.6 Å above a surface Fe atom, which reduces the interaction between the Fe atom and the oxygen layer below. The Fe atom, which

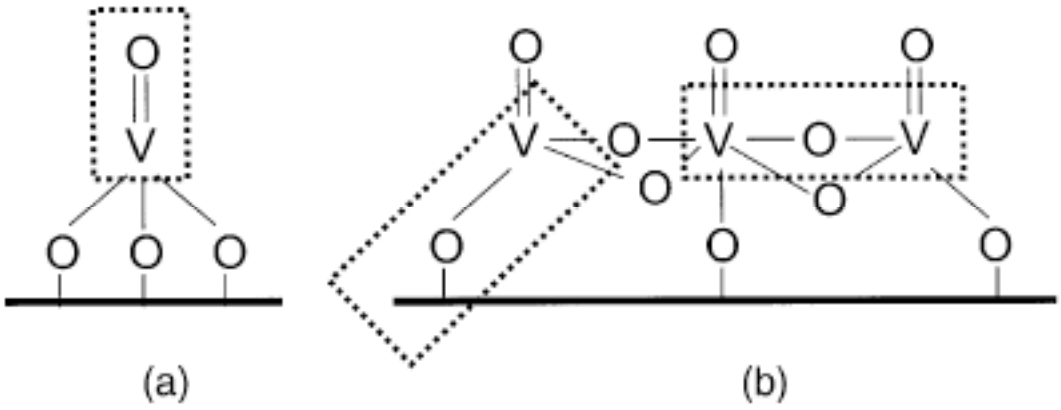

Figure 7.9: (a) Schematic of an isolated VO_4 unit on the surface of a metal oxide support. The terminal V=O bond of the isolated VO_4 unit has been highlighted. (b) Schematic of the interaction of the VO_4 structural units with higher vanadia loading. In addition to the terminal V=O bond, the formation of polymeric VO_4 chains results in the formation of bridging V–O–V bonds and V–O–support bonds. Reprinted from reference [49], Copyright 2005 with permission from Elsevier.

has a formal oxidation state of +5, is tetrahedrally coordinated with the underlying oxygen layer and the sole oxygen atom directly above. This ferryl (Fe=O) termination was predicted to be stable under high oxygen chemical potentials using density functional theory calculations [43], and was directly observed using STM and infrared reflection absorption spectroscopy (IRAS) [88]. Therefore, the structural similarity between the vanadium pentaoxide in the VO_4 state and the ferryl termination of the α-$Fe_2O_3(0001)$ surface would seem to suggest the vanadium adatoms observed in this study have a similar oxygen coordination. Furthermore, it provides a natural explanation for the upward shift experienced by a majority of the adsorbed vanadium.

The presence of the minority vanadium adsorption site may also be understood in terms of these VO_4 structural units and how they interact with each other. Because of the low vanadium coverage involved in this experiment (0.51 ML), it is not surprising that the majority of the adsorbed vanadium would adopt an atomic arrangement similar to that of the isolated VO_4 units. Because the vanadium coverage may not constitute a continuous adlayer on the surface, it is reasonable to believe most of the vanadium will be widely dispersed on the hematite surface, and therefore the VO_4 units will not interact with each other. However, other areas of the surface may have an increased vanadium areal density, and there will be a greater likelihood that the VO_4 units will interact and bond with each other.

As previously mentioned, the interaction of these isolated vanadia units on various oxide surfaces can result in other types of chemical bonding, namely the formation of dimeric and polymeric chains of the VO_4 molecules. With the formation of these polymerized species on the oxide surface, it is possible that the vanadium adatoms may rearrange and take up other atomic positions, such as the minority vanadium occupation site visualized in the XSW direct-space image. Therefore, it may be reasonable to incorporate these polymeric vanadium oxides in any structural models that account for the secondary vanadium position. In addition, because these polymeric vanadia units typically possess bridging V–O–V bonds, the presence of these bridging bonds may be an important component of any proposed surface model.

One such example that includes these two attributes is shown in Figure 7.10, which proposes how the interaction of three neighboring VO_4 units can form three bridging V–O–V bonds. The vanadium adatom common to these three bonds is located in the secondary adsorption site, and possesses the same tetrahedral oxygen coordination as the isolated VO_4 units with the bonding of an on-top oxygen anion. The V–O–V bridging bonds also reflect the spatial breadth of the secondary vanadium density maxima, which is shown in Figure 7.8 as extending towards the primary adsorption site in the same direction as the bridging bonds depicted in Figure 7.10. It must be noted that it has been assumed that the bridging bonds described here are derived from the terminal V=O bond between the oxidized vanadium and the on-top

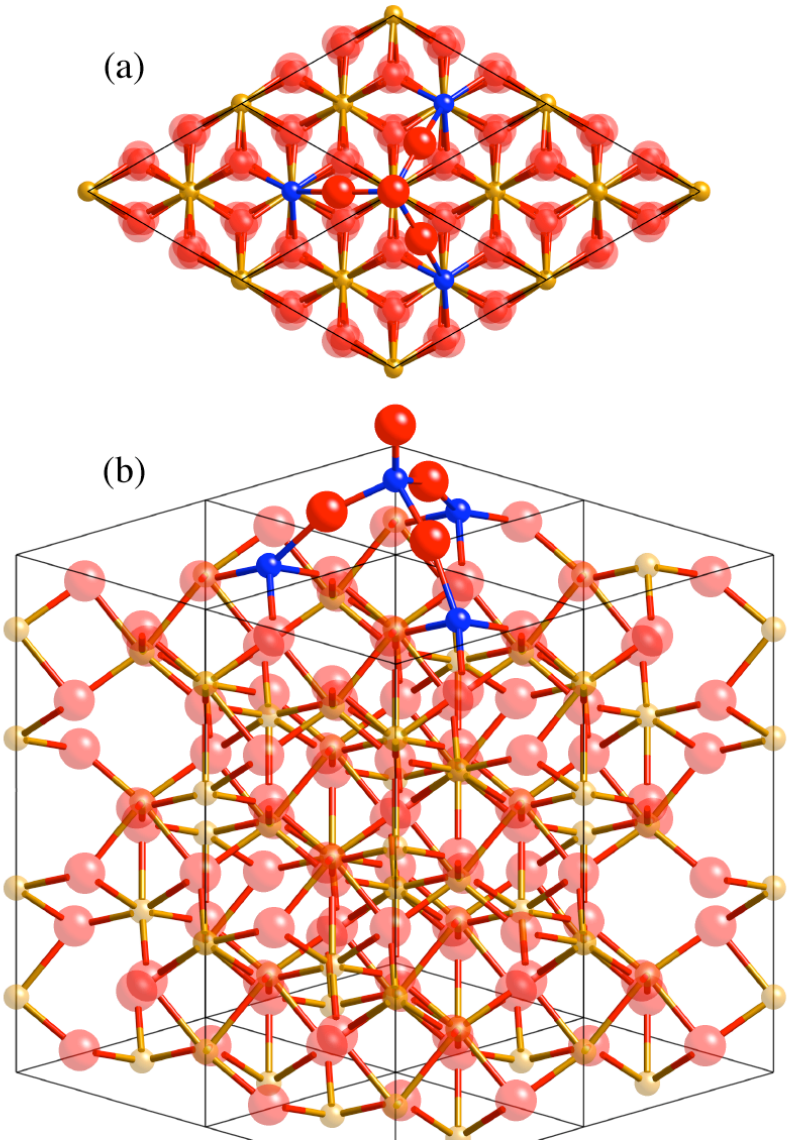

Figure 7.10: Ball-and-stick model of polymerized vanadia VO_4 units with vanadium (blue spheres) located in the primary and secondary occupational sites seen in the XSW direct space image. (a) Top view of surface, which shows how three individual VO_4 units can combine to form a localized layer of oxygen atoms (red spheres) that form another VO_4 structural unit. (b) Tilted view of ball-and-stick model.

oxygen atom. Therefore, the small fraction of VO_4 units that polymerize and adopt this proposed bonding arrangement may have a different electronic configuration than the isolated VO_4 units that make up a majority of the vanadium distribution. For instance, while the previous XPS measurements previously described suggest the oxidized vanadium has a +5 oxidation state, the polymerized vanadia units may deviate from this formal oxidation state.

Another alternative to this scenario a surface model consisting of vanadium adatoms that coexist with Fe atoms in the adlayer, which has a similar structure to the complete bulk-like Fe bilayer. This bilayer of 1/2 vanadium atoms and 1/2 iron atoms is then terminated by a layer of oxygen atoms, which essentially reproduces the bulk-like hematite structure. Another vanadium oxide VO_4 structural unit can then be situated on top of this oxygen terminated surface, thereby populating the minority adsorption site seen in the direct-space image. Because the oxidized vanadium was observed to consist of V^{5+} cations, if the vanadium adatoms are arranged such that they extend the bulk-like crystal structure, their configuration may have a parallel in the distorted octahedral coordination that describes the structure of crystalline V_2O_5. Such VO_6 units have been observed in supported vanadium oxides with very high vanadia loadings [49]. However, because the VO_6 units that comprise this surface model coexist with the octahedrally coordinated Fe^{3+} cations, this surface model is quite complex, and further investigations on the potential stability of such a surface are required.

7.4 Summary

The atomic-scale structure of submonolayer vanadium and vanadium oxides adsorbed on the α-Fe_2O_3(0001) surface has been experimentally determined using the XSW direct-space imaging method. The XSW results clearly indicate there is a reversible change in the vanadium atomic distribution as the vanadium is oxidized and reduced in a cyclic catalytic process involving atomic oxygen and atomic hydrogen. In order to provide further structural details of the as-deposited and oxidized vanadium surfaces, XSW direct-space images were generated of the two distinct surfaces. The XSW direct-space image of the as-deposited surface suggest the V^{3+} cations adopt Fe bulk-like positions on the hematite surface and continue the corundum structure of the hematite substrate. The adsorption of vanadium on the clean Fe_2O_3(0001) surface may also be accompanied by surface relaxations of the iron or oxygen atomic layers. After oxidizing the adsorbed vanadium, direct-space images suggest there is a vertical shift of 0.39 Å in the vanadium spatial distribution as the vanadium cations in their +5 oxidation state become arranged in VO_4 structural units. A secondary vanadium occupational site also is apparent from the direct-space image. While the VO_4 units are typically isolated from one another at low vanadium coverages, the observed minority site may be the result of the VO_4 structural units interacting with each other and forming polymeric chains.

Chapter 8: Summary and Future Work

8.1 Thesis Summary

The primary motivation for the work detailed in this dissertation is the structural characterization of two very different material systems using the XSW technique and the XSW direct-space imaging method. These two surfaces, the 1/3 ML Sn/Si(111)-($\sqrt{3}$ x $\sqrt{3}$)R30° and the 1/2 ML V/Fe_2O_3(0001) system, have very different electronic, structural, and physical properties, yet it is a testament to the flexibility of the XSW technique that we can successfully probe these two disparate surfaces. More specifically, we have demonstrated the usefulness of the model-independent XSW direct-space imaging method, especially in cases where traditional XSW analysis fails to determine a particular adsorption geometry.

In our study of the 1/3 ML Sn/Si(111) $\sqrt{3}$ surface, it was demonstrated that by using the XSW technique to collect a number of Fourier components of the Sn atomic density distribution, we can determine the atomic scale structure of the room temperature Sn adatom distribution. Most of the XSW measurements were collected along the surface normal direction in order to address the question of whether the Sn adatoms are arranged in a single-layer, as suggested by other structural studies, or in a rippled configuration, as predicted by a dynamical fluctuations model. Direct-space atomic density maps generated from the normal and off-normal XSW data confirmed the Sn adatoms are located at T_4 adsorption sites. By applying a reasonable structural model to these (*hhh*) XSW measurements, it was determined that Sn adatoms are

configured in a “one up and two down” geometry, with the two types of Sn separated by 0.26 Å. This lends support to the behavior predicted by the dynamical fluctuations model, which concludes the $\sqrt{3}$ symmetry observed by other structural investigations is actually the effect of thermal fluctuations, which obscures the actual (3 x 3) symmetry of the ground state.

The XSW measurements conducted on another Sn/Si(111) surface preparation were not consistent with a surface structure made up of Sn adatoms located at the T_4 adsorption sites. However, by generating the Sn atomic density distribution from the XSW-determined Fourier components, the direct-space image clearly explained this discrepancy by showing that while most of the Sn adatoms were present at the T_4 sites, some of the Sn had migrated to a second occupational site below the Si substrate. By modifying the previously discussed structural model to account for the subsurface Sn, it was determined that the additional Sn atoms are located 0.37 Å below the top of the Si bulk-like surface and substitute for Si atoms located in the bottom of the surface bilayer.

In the XSW investigation of the 1/2 ML V/Fe_2O_3(0001) surface, the focus was on determining how the surface structure of the adsorbed vanadium is affected by the presence of oxidizing and reducing agents, such as atomic oxygen and atomic hydrogen. Recent XPS measurements have demonstrated how the electronic structures of both the vanadium adlayer and the hematite substrate are modified by the exposure

to atomic oxygen and restored with a subsequent exposure to atomic hydrogen. The results of our XSW measurements have demonstrated how these electronic changes are accompanied by significant changes in the geometry of the vanadium atomic distribution.

By comparing the acquired XSW data for the as-deposited, oxidized, and reduced vanadium surfaces, it becomes obvious that there is a shift in the vanadium adsorption geometry after exposing the vanadium adlayer to oxygen. Furthermore, the structure of the oxidized vanadium distribution then reverts to that of the as-deposited surface after being exposed to atomic hydrogen. By generating XSW real-space density maps using the collected Fourier coefficients, the vanadium atomic density distribution can be directly imaged and used as the basis for proposing a viable structural model for each of the two distinct vanadium surfaces.

As seen in the XSW direct-space images, the atomic arrangement of the as-deposited and reduced surfaces involves vanadium adatoms located in the bulk-like Fe positions. This adsorption geometry also involves measurable atomic relaxations in the direction normal to the $Fe_2O_3(0001)$ surface. The presence of the vanadium adatoms in the Fe bulk-like positions is not unexpected, because the structure of the vanadium adlayer mimics the corundum crystallographic structure of the bulk hematite substrate. This is also consistent with XPS measurements that indicate the as-deposited and reduced vanadium atoms have oxidation states of +3.

The XSW direct-space images of the oxidized vanadium surface show that the as-deposited vanadium atoms are elevated by 0.39 Å after being exposed to atomic oxygen. Furthermore, a secondary adsorption site becomes apparent in the image; this minority vanadium site is also located near a bulk-like Fe position. The image was interpreted as the result of vanadium pentaoxides configured as VO_4 units, in which the oxidized vanadium adatoms are tetrahedrally coordinated to the surrounding oxygen atoms. The low vanadium coverage suggests most of these VO_4 units will be isolated from each other, yet in regions of the sample where the vanadium areal density is higher, the secondary adsorption site shown on the direct-space image can be populated by these VO_4 atomic units. These units can interact and result in bridging oxygen bonds between the two types of vanadium adsorption sites.

8.2 Future Work

One important aspect of the 1/3 ML Sn/Si(111) surface that separates it from the more widely studied 1/3 ML Sn/Ge(111) surface is it is can be considered a surface alloy, as the $\sqrt{3}$ surface is stable over a relatively wide range of Sn coverages. This is because any deviation from the ideal Sn coverage of 1/3 ML is compensated by the presence of Si adatoms that occupy the T_4 adsorption sites and maintain the $\sqrt{3}$ symmetry. While there have been several studies that examined the electronic structure of the Sn/Si(111) surface as a function of the Sn coverage, it would be interesting to

probe how the "rippled" configuration of the Sn adatoms is affected by the intermixing of Sn and Si atoms in the adlayer. This would require collecting several sets of XSW data over a wide range of Sn coverage from 0.15 ML to 0.40 ML.

The XSW direct-space images of the higher-coverage Sn/Si(111) surface clearly demonstrate that there is a secondary Sn occupation site within the bulk Si substrate at Si substitutional sites. However, the question of what is the driving force behind this unexpected migration of Sn adatoms remains. Because we observed only a single instance of this subsurface Sn for a particular surface preparation, it is difficult to definitively point to a specific cause for the appearance of this secondary occupational site. While it is known that differences in sample preparation (such as the annealing temperature) has a profound effect on the density of defects in the surface layer, it is not clear if the presence of Sn substitutional defects below the surface has a similar dependence. What is required is a series of XSW experiments conducted over a wide area in coverage-temperature space, in order to determine the effect of different surface preparations on the population of the subsurface site. Another potentially more exciting experiment would be to use XSW to probe the Sn surface during the annealing process, in order to possibly achieve a time-resolved understanding of the migration of Sn from the surface layer.

In the XSW investigation of the $V/Fe_2O_3(0001)$ system, we were able to directly ascertain the adsorption geometry of the vanadium in its as-deposited, oxidized, and

reduced state. However, the XSW technique is unable to provide any structural information about the surface iron or oxygen ions that are affected by the adsorption of vanadium. Density functional theory calculations are currently underway in order to investigate the stability of the proposed structural models, as well as provide some information regarding the atomic arrangement of the surface iron and oxygen. These calculations will also prove important in furthering our understanding of the oxidation-reduction process that is initiated by the vanadium adatoms. Furthermore, by complementing our XSW data with extended X-ray absorption fine structure (EXAFS) measurements, we can experimentally determine the local atomic geometry surrounding the adsorbed vanadium for comparison with the theoretical results.

Another aspect of the $V/Fe_2O_3(0001)$ system that is not explored by the XSW experiments is the morphology of the vanadium deposits. However, an appropriate comparison may be found in the morphology of submonolayer vanadium on alumina surfaces. Using STM to probe the conformation of vanadium deposited on thin alumina films, Baümer *et al*. observed that the vanadium is incorporated in islands, which span about 20–30 Å in diameter [65]. The height and diameter of these vanadium particles increased with the vanadium coverage, and as the amount of adsorbed vanadium grew over one monolayer, the particles merge into a continuous surface layer. Determining if this simultaneous multilayer growth mode also describes the growth of vanadium on the hematite surface is an opportunity for a local probe such as STM or AFM.

REFERENCES

1. N. Hertel, G. Materlik, and J. Zegenhagen, *X-ray standing wave analysis of bismuth implanted in Si(110)*. Zeitschrift fur Physik B (Condensed Matter), 1985. **58**(3), 199.

2. K. Takayanagi, Y. Tanishiro, S. Takahashi, and M. Takahashi, *Structure analysis of Si(111)-7 x 7 reconstructed surface by transmission electron diffraction*. Surface Science, 1985. **164**(2-3), 367.

3. V.G. Lifshits, A.A. Saranin, and A.V. Zotov, *Surface phases on silicon: preparation, structures, and properties*. 1994, Chichester [England]; New York: J.Wiley. xiv, 448 p.

4. K. Takayanagi and Y. Tanishiro, *Dimer-chain model for the 7 x 7 and the 2 x 8 reconstructed surfaces of Si(111) and Ge(111)*. Physical Review B, 1986. **34**(2), 1034-1040.

5. S. Iwanari and K. Takayanagi, *Surfactant epitaxy of Si on Si(111) surface mediated by a Sn layer I. Reflection electron microscope observation of the growth with and without a Sn layer mediate the step flow*. Journal Of Crystal Growth, 1992. **119**(3-4), 229-240.

6. T. Ichikawa, *Structural study of ultrathin Sn layers deposited onto Ge(111) and Si(111) surfaces by RHEED*. Surface Science, 1984. **140**(1), 37-63.

7. J.M. Carpinelli, H.H. Weitering, M. Bartkowiak, R. Stumpf, and E.W. Plummer, *Surface charge ordering transition: α phase of Sn/Ge(111)*. Physical Review Letters, 1997. **79**(15), 2859-2862.

8. J.M. Carpinelli, H.H. Weitering, E.W. Plummer, and R. Stumpf, *Direct observation of a surface charge density wave*. Nature, 1996. **381**(6581), 398-400.

9. A.V. Melechko, J. Braun, H.H. Weitering, and E.W. Plummer, *Two-dimensional phase transition mediated by extrinsic defects*. Physical Review Letters, 1999. **83**(5), 999-1002.

10. A.V. Melechko, J. Braun, H.H. Weitering, and E.W. Plummer, *Role of defects in two-dimensional phase transitions: An STM study of the Sn/Ge(111) system*. Physical Review B, 2000. **61**(3), 2235-2245.

11. L. Petersen, Ismail, and E.W. Plummer, *Defect-blurred two-dimensional phase transition*. Progress in Surface Science, 2002. **71**(1-4), 1-29.

12. H.H. Weitering, J.M. Carpinelli, A.P. Melechko, J.D. Zhang, M. Bartkowiak, and E.W. Plummer, *Defect-mediated condensation of a charge density wave*. Science, 1999. **285**(5436), 2107-2110.

13. T.E. Kidd, T. Miller, M.Y. Chou, and T.C. Chiang, *Sn/Ge(111) surface charge-density-wave phase transition*. Physical Review Letters, 2000. **85**(17), 3684-3687.

14. J. Avila, Y. Huttel, G. Le Lay, and M.C. Asensio, *Dynamical fluctuation and surface phase transition at the Sn/Ge(111) $\sqrt{3} \times \sqrt{3}R30°$-$\alpha$ interface*. Applied Surface Science, 2000. **162**, 48-55.

15. D. Farias, W. Kaminski, J. Lobo, J. Ortega, E. Hulpke, R. Perez, F. Flores, and E.G. Michel, *Phonon softening, chaotic motion, and order-disorder transition in Sn/Ge(111)*. Physical Review Letters, 2003. **91**(1), 016103.

16. J. Ortega, R. Perez, and F. Flores, *Dynamical fluctuations and the $\sqrt{3} \times \sqrt{3} \Leftrightarrow 3 \times 3$ transition in α-Sn/Ge(111) and Sn/Si(111)*. Journal of Physics-Condensed Matter, 2002. **14**(24), 5979-6004.

17. R. Perez, J. Ortega, and F. Flores, *Surface soft phonon and the $\sqrt{3} \times \sqrt{3} \Leftrightarrow 3 \times 3$ phase transition in Sn/Ge(111) and Sn/Si(111)*. Physical Review Letters, 2001. **86**(21), 4891-4894.

18. K.M. Conway, J.E. Macdonald, C. Norris, E. Vlieg, and J.F. Vanderveen, *The structure of the Si(111)$(\sqrt{3} \times \sqrt{3})R30°$-Sn surface determined using X-ray diffraction*. Surface Science, 1989. **215**(3), 555-565.

19. J.S. Okasinski, C.-Y. Kim, D.A. Walko, and M.J. Bedzyk, *X-ray standing wave imaging of the 1/3 monolayer Sn/Ge(111) surface*. Physical Review B, 2004. **69**(4), 041401-4.

20. J. Avila, A. Mascaraque, E.G. Michel, M.C. Asensio, G. LeLay, J. Ortega, R. Perez, and F. Flores, *Dynamical fluctuations as the origin of a surface phase transition in Sn/Ge(111)*. Physical Review Letters, 1999. **82**(2), 442-445.

21. R.I.G. Uhrberg, H.M. Zhang, and T. Balasubramanian, *Determination of the Sn 4d line shape of the Sn/Ge(111) √3 x √3 and 3 x 3 surfaces*. Physical Review Letters, 2000. **85**(5), 1036-1039.

22. R.I.G. Uhrberg and T. Balasubramanian, *Electronic structure of the √3 x √3- and 3 x 3 periodicities of Sn/Ge(111)*. Physical Review Letters, 1998. **81**(10), 2108-2111.

23. L. Ottaviano, M. Crivellari, L. Lozzi, and S. Santucci, *STM investigation of the α-Sn/Si(111) phase at 120 K*. Surface Science, 2000. **445**(1), L41-L46.

24. H. Morikawa, I. Matsuda, and S. Hasegawa, *STM observation of Si(111)-α-√3 x √3-Sn at low temperature*. Physical Review B, 2002. **65**(20), 201308.

25. T. Yamanaka and S. Ino, *Surface electron standing waves and adatom heights on Si(111)- √3 x √3-(Ga,In,Sn) surfaces*. Physical Review B, 2000. **61**(8), R5074-R5077.

26. G. Profeta, A. Continenza, L. Ottaviano, W. Mannstadt, and A.J. Freeman, *Structural and electronic properties of the Sn/Si(111) √3 x √3R30° surface*. Physical Review B, 2000. **62**(3), 1556-1559.

27. G. Profeta, L. Ottaviano, S. Santucci, and A. Continenza, *Two-dimensional alloying on Si(111) surface: An ab initio study*. Physical Review B, 2002. **66**(8), 081303.

28. R.I.G. Uhrberg, H.M. Zhang, T. Balasubramanian, S.T. Jemander, N. Lin, and G.V. Hansson, *Electronic structure of Sn/Si(111) √3 x √3: Indications of a low-temperature phase*. Physical Review B, 2000. **62**(12), 8082-8086.

29. M.E. Davila, J. Avila, M.C. Asensio, and G. Le Lay, *Giant effect of electron and hole donation on Sn/Ge(111) and Sn/Si(111) surfaces*. Physical Review B, 2004. **70**(24), -.

30. G. Ballabio, G. Profeta, S. de Gironcoli, S. Scandolo, G.E. Santoro, and E. Tosatti, *Disproportionation phenomena on free and strained Sn/Ge(111) and Sn/Si(111) surfaces*. Physical Review Letters, 2002. **89**(12), 126803.

31. A. Charrier, R. Perez, F. Thibaudau, J.M. Debever, J. Ortega, F. Flores, and J.M. Themlin, *Contrasted electronic properties of Sn-adatom-based (√3 x √3)R30° reconstructions on Si(111)*. Physical Review B, 2001. **64**(11), 115407.

32. J. Lobo, A. Tejeda, A. Mugarza, and E.G. Michel, *Electronic structure of Sn/Si(111)-(√3 x √3)R30° as a function of Sn coverage*. Physical Review B, 2003. **68**(23), 235332.

33. R.M. Cornell and U. Schwertmann, *The iron oxides: structure, properties, reactions, occurrences, and uses*. 2nd, completely rev. and extended ed. 2003, Weinheim: Wiley-VCH. xxxix, 664 p.

34. R.L. Kurtz and V.E. Henrich, *Geometric structure of the α-Fe_2O_3(001) surface: a LEED and XPS study*. Surface Science, 1983. **129**(2-3), 345-354.

35. R.J. Lad and V.E. Henrich, *Structure of α-Fe_2O_3 single crystal surfaces following Ar+ ion bombardment and annealing in O_2*. Surface Science, 1988. **193**(1-2), 81-93.

36. M. Pollak, M. Gautier, N. Thromat, S. Gota, W.C. Mackrodt, and V.R. Saunders, *An in-situ study of the surface phase transitions of α-Fe_2O_3 by X-ray absorption spectroscopy at the oxygen K edge*. Nuclear Instruments & Methods

in Physics Research Section B-Beam Interactions with Materials and Atoms, 1995. **97**(1-4), 383-386.

37. N.G. Condon, F.M. Leibsle, A.R. Lennie, P.W. Murray, T.M. Parker, D.J. Vaughan, and G. Thornton, *Scanning tunnelling microscopy studies of α-Fe_2O_3(0001)*. Surface Science, 1998. **397**(1-3), 278-287.

38. N.G. Condon, F.M. Leibsle, A.R. Lennie, P.W. Murray, D.J. Vaughan, and G. Thornton, *Biphase Ordering of Iron-Oxide Surfaces*. Physical Review Letters, 1995. **75**(10), 1961-1964.

39. C.Y. Kim, A.A. Escuadro, M.J. Bedzyk, L. Liu, and P.C. Stair, *X-ray scattering study of the stoichiometric recovery of the α-Fe_2O_3(0001) surface*. Surface Science, 2004. **572**(2-3), 239-246.

40. F. Alvarez-Ramirez, J.M. Martinez-Magadan, J.R.B. Gomes, and F. Illas, *On the geometric structure of the (0001) hematite surface*. Surface Science, 2004. **558**(1-3), 4-14.

41. X.G. Wang, W. Weiss, S.K. Shaikhutdinov, M. Ritter, M. Petersen, F. Wagner, R. Schlogl, and M. Scheffler, *The hematite (α-Fe_2O_3) (0001) surface: Evidence for domains of distinct chemistry*. Physical Review Letters, 1998. **81**(5), 1038-1041.

42. S.K. Shaikhutdinov and W. Weiss, *Oxygen pressure dependence of the α-Fe_2O_3(0001) surface structure*. Surface Science, 1999. **432**(3), L627-L634.

43. W. Bergermayer, H. Schweiger, and E. Wimmer, *Ab initio thermodynamics of oxide surfaces: O_2 on Fe_2O_3(0001)*. Physical Review B, 2004. **69**(19), 195409.

44. S.A. Chambers and S.I. Yi, *Fe termination for α-Fe_2O_3(0001) as grown by oxygen-plasma-assisted molecular beam epitaxy*. Surface Science, 1999. **439**(1-3), L785-L791.

45. A. Rohrbach, J. Hafner, and G. Kresse, *Ab initio study of the (0001) surfaces of hematite and chromia: Influence of strong electronic correlations*. Physical Review B, 2004. **70**(12), 125426.

46. S. Thevuthasan, Y.J. Kim, S.I. Yi, S.A. Chambers, J. Morais, R. Denecke, C.S. Fadley, P. Liu, T. Kendelewicz, and G.E. Brown, *Surface structure of MBE-grown α-Fe_2O_3(0001) by intermediate-energy X-ray photoelectron diffraction*. Surface Science, 1999. **425**(2-3), 276-286.

47. M.D. Pashley, *Electron counting model and its application to island structures on molecular-beam epitaxy grown GaAs(001) and ZnSe(001)*. Physical Review B, 1989. **40**(15), 10481-10487.

48. O. Warschkow, D.E. Ellis, J.H. Hwang, N. Mansourian-Hadavi, and T.O. Mason, *Defects and charge transport near the hematite (0001) surface: An atomistic study of oxygen vacancies*. Journal of the American Ceramic Society, 2002. **85**(1), 213-220.

49. B.M. Weckhuysen and D.E. Keller, *Chemistry, spectroscopy and the role of supported vanadium oxides in heterogeneous catalysis*. Catalysis Today, 2003. **78**(1-4), 25-46.

50. G.C. Bond and S.F. Tahir, *Vanadium-Oxide Monolayer Catalysts - Preparation, Characterization and Catalytic Activity*. Applied Catalysis, 1991. **71**(1), 1-31.

51. S. Surnev, M.G. Ramsey, and F.P. Netzer, *Vanadium oxide surface studies*. Progress in Surface Science, 2003. **73**(4-8), 117-165.

52. V.E. Henrich and P.A. Cox, *The Surface Science of Metal Oxides*. 1994, Cambridge: Cambridge University Press.

53. R. Enjalbert and J. Galy, *A refinement of the structure of V_2O_5*. Acta Crystallographica Section C-Crystal Structure Communications, 1986. **42**, 1467-1469.

54. Z.M. Zhang and V.E. Henrich, *Electronic interactions in the vanadium/TiO_2(110) and vanadia/TiO_2(110) model catalyst systems*. Surface Science, 1992. **277**(3), 263-272.

55. J. Biener, M. Baumer, J. Wang, and R.J. Madix, *Electronic structure and growth of vanadium on TiO_2(110)*. Surface Science, 2000. **450**(1-2), 12-26.

56. M. Sambi, G. Sangiovanni, G. Granozzi, and F. Parmigiani, *Early stages of epitaxial growth of vanadium oxide at the TiO_2(110) surface studied by photoelectron diffraction*. Physical Review B, 1996. **54**(19), 13464-13467.

57. M. Sambi, M. Della Negra, and G. Granozzi, *Growth and structural characterisation of vanadium oxide ultrathin films on TiO_2 (110)*. Thin Solid Films, 2001. **400**(1-2), 26-36.

58. M. Sambi, G. Sangiovanni, G. Granozzi, and F. Parmigiani, *Growth and the structure of epitaxial VO_2 at the TiO_2(110) surface*. Physical Review B, 1997. **55**(12), 7850-7858.

59. J. Biener, M. Baumer, and R.J. Madix, *A synchrotron study of the deposition of vanadia on TiO_2(110)*. Surface Science, 1999. **432**(3), 178-188.

60. M. Sambi, M. Della Negra, and G. Granozzi, *The structure of vanadia ultrathin films grown on TiO_2(110) in an oxygen ambient*. Surface Science, 2000. **470**(1-2), L116-L122.

61. Q. Guo, S. Lee, and D.W. Goodman, *Vanadium oxides thin films grown on rutile TiO_2(110)-(1 x 1) and (1 x 2) surfaces*. Surface Science, 1999. **437**(1-2), 38-48.

62. Q.G. Wang and R.J. Madix, *Partial oxidation of methanol to formaldehyde on a model supported monolayer vanadia catalyst: vanadia on TiO_2(110)*. Surface Science, 2002. **496**(1-2), 51-63.

63. Q.G. Wang and R.J. Madix, *Preparation and reactions of V_2O_5 supported on $TiO_2(110)$*. Surface Science, 2001. **474**(1-3), L213-L216.

64. G.S. Wong, M.R. Concepcion, and J.M. Vohs, *Reactivity of monolayer V_2O_5 films on $TiO_2(110)$ produced via the oxidation of vapor-deposited vanadium*. Surface Science, 2003. **526**(3), 211-218.

65. M. Baümer, J. Biener, and R.J. Madix, *Growth, electronic properties and reactivity of vanadium deposited onto a thin alumina film*. Surface Science, 1999. **432**(3), 189-198.

66. J. Biener, M. Baumer, R.J. Madix, P. Liu, E.J. Nelson, T. Kendelewicz, and G.E. Brown, *A synchrotron study of the growth of vanadium oxide on $Al_2O_3(0001)$*. Surface Science, 1999. **441**(1), 1-9.

67. R.J. Madix, J. Biener, M. Baumer, and A. Dinger, *The growth of vanadium oxide on alumina and titania single crystal surfaces*. Faraday Discussions, 1999(114), 67-84.

68. J. Biener, M. Baumer, R.J. Madix, P. Liu, E. Nelson, T. Kendelewisz, and G. Brown, *Growth and electronic structure of vanadium on α-$Al_2O_3(0001)$*. Surface Science, 2000. **449**(1-3), 50-60.

69. C.Y. Kim, *The electronic structure study of the V/Fe_2O_3 system*. (submitted to Physical Review B).

70. B.W. Batterman, *Effect of Dynamical Diffraction in X-Ray Fluorescence Scattering*. Physical Review, 1964. **133**(3A), A759-A764.

71. B.W. Batterman, *Detection of Foreign Atom Sites by Their X-Ray Fluorescence Scattering*. Physical Review Letters, 1969. **22**(14), 703.

72. P.L. Cowan, J.A. Golovchenko, and M.F. Robbins, *X-Ray Standing Waves at Crystal-Surfaces*. Physical Review Letters, 1980. **44**(25), 1680-1683.

73. J.A. Golovchenko, J.R. Patel, D.R. Kaplan, P.L. Cowan, and M.J. Bedzyk, *Solution to the Surface Registration Problem Using X-Ray Standing Waves*. Physical Review Letters, 1982. **49**(8), 560-563.

74. P.P. Ewald, *Zur Begründung der Kristalloptik - Teil III*. Ann. Physik, 1917. **54**, 519-597.

75. C.G. Darwin, *The theory of X-ray reflection*. Philosophical Magazine, 1914. **27**, 315.

76. M. von Laue, *Röntenstrahl-Interferenzen*. 3rd ed. 1960, Frankfurt: Akademische Verlagsgesellschaft.

77. B.W. Batterman and H. Cole, *Dynamical Diffraction of X Rays by Perfect Crystals*. Reviews of Modern Physics, 1964. **36**(3), 681-717.

78. J. Zegenhagen, *Surface-Structure Determination with X-Ray Standing Waves*. Surface Science Reports, 1993. **18**(7-8), 199-271.

79. H. Wagenfeld, *Normal and Anomalous Photoelectric Absorption of X Rays in Crystals*. Physical Review, 1966. **144**(1), 216-224.

80. M.J. Bedzyk and L.W. Cheng, *X-ray standing wave studies of minerals and mineral surfaces: Principles and applications*. Applications of Synchrotron Radiation in Low-Temperature Geochemistry and Environmental Sciences, 2002. **49**, 221-266.

81. D. Marasco, *X-Ray Investigations of Ferroelectric Thin Films and Related Surface Structures*. 2002, Northwestern University: Evanston.

82. J.S. Okasinski, *Investigations on the (√3 x √3)R30° to (3 x 3) Phase Transitions for the 1/3 ML Sn/Ge(111) and 1/3 ML Pb/Ge(111) Surfaces*. 2003, Northwestern University: Evanston.

83. Y. Qian, *X-Ray Standing Wave Investigations of Group III and V Elements Adsorbed on the Si(001) Surface: Structure, Dynamics, and Kinetics*. 1995, Northwestern University: Evanston.

84. S.T. Jemander, N. Lin, H.M. Zhang, R.I.G. Uhrberg, and G.V. Hansson, *An STM study of the surface defects of the (√3 x √3)-Sn/Si(111) surface*. Surface Science, 2001. **475**(1-3), 181-193.

85. C. Tornevik, M. Göthelid, M. Hammar, U.O. Karlsson, N.G. Nilsson, S.A. Flodström, C. Wigren, and M. Ostling, *Adsorption of Sn on Si(111)7x7: reconstructions in the monolayer regime*. Surface Science, 1994. **314**(2), 179-187.

86. W.D. Xiao, K. Xie, Q.L. Guo, and E.G. Wang, *Interaction of metal with oxide films: V on Cr_2O_3(0001)/Re(0001) and Cr on V_2O_3(0001)/Re(0001)*. Journal of Physics-Condensed Matter, 2002. **14**(25), 6321-6328.

87. V. Brazdova, M.V. Ganduglia-Pirovano, and J. Sauer, *Periodic density functional study on structural and vibrational properties of vanadium oxide aggregates*. Physical Review B, 2004. **69**(16), 165420.

88. C. Lemire, S. Bertarione, A. Zecchina, D. Scarano, A. Chaka, S. Shaikhutdinov, and H.J. Freund, *Ferryl (Fe=O) termination of the hematite α-Fe_2O_3(0001) surface*. Physical Review Letters, 2005. **94**(16), 166101.

Appendix: Software Packages for XSW Analysis

A.1 Recent Developments with SWAN

The primary software tool used to manipulate and analyze data from a XSW experiment is SWAN (Standing Wave ANalysis), which is derived from an older application known as DARE developed by M. Bedzyk and J. Zegenhagen. SWAN has three primary uses during the data collection and analysis process. First, SWAN can calculate some physical parameters such as Bragg angles, structure factors, and ideal Darwin widths for a given crystal under a chosen dynamical diffraction condition. SWAN is also used to manipulate the data files created during the course of an XSW experiment and generate new files containing the reflectivity and fluorescence data of interest. Most importantly, SWAN is able to calculate and convolve the ideal monochromator and sample reflectivity curves and fit the result of this convolution to the experimental rocking curve data. The result of the reflectivity fit is then used to perform a fit of the theoretical fluorescence yield to the experimental fluorescence yield data in order to obtain the resulting coherent position, coherent fraction, and off-Bragg normalized fluorescence yield.

While the basic functionality of SWAN has not changed since its initial development, it is occasionally required to modify its behavior, either to correct calculation errors or to introduce new functionality to streamline the analysis process. There have been several significant changes to the SWAN software since it was first documented in the doctoral dissertation of Likwan Cheng. These modifications, as well

as the process of creating and compiling future versions, will be detailed in the following sections.

The main improvement that SWAN provides over the older DARE data analysis program is the ability to analyze XSW data from any arbitrary crystalline structure with a definable unit cell. However, this added flexibility comes at the cost of increased complexity; namely, because SWAN can perform calculations for any user-defined crystal, it is possible that the chosen origin for a user-defined unit cell will not be symmetric. Unlike in the case of DARE, which calculates the necessary structure factors for a chosen material assuming a symmetric origin (for the typical case of a Si or Ge substrate), SWAN does not impose this constraint. Therefore, it is common for the structure factors for the Hth and –Hth direction (F_H and $F_{\bar{H}}$ respectively) to be unequal. This important difference between SWAN and DARE made it necessary to make some important changes to SWAN in order to calculate the theoretical reflectivity and fluorescence yield correctly.

One necessary change involves how the reduced angular coordinate discussed in Chapter 4 is defined. Recall that this parameter η can be expressed as

$$\eta = \frac{b\Delta\theta\sin(2\theta_b) + 1/2(1-b)\Gamma F_0}{\Gamma\sqrt{|b|}\sqrt{(F_H F_{\bar{H}})}}. \qquad \textbf{(A.1)}$$

In earlier versions of swan, the denominator of this equation was expressed simply (in the source file swan.f) as `real(cd_chi_1)`, where `cd_chi_1` represents the electrical

susceptibility in the Hth direction. While this expression was sufficient for the simpler DARE software package, it is insufficient when F_H and $F_{\bar{H}}$ are not equivalent, as may be the case for an arbitrary crystalline system used in SWAN. Therefore, the definition for η in SWAN was changed to include the term `real(sqrt(cd_chi_1*cd_chi_1_b))` (where `cd_chi_1_b` represents the electrical susceptibility in the –Hth direction) in the denominator in order to better reflect the true expression for the reduced angle parameter. Before this change was implemented, SWAN would occasionally calculate rocking curves with a reversed angle scale depending on how the unit cell origin was chosen. Instructions on how future versions of SWAN should be maintained, compiled, and distributed will be presented in Section A.1.3.

A.1.1 New functionality in SWAN (as of version 2.1.3)

While there have been several "under-the-hood" changes in the SWAN analysis software, there have also been some more obvious additions to SWAN that serve to streamline the analysis process. Furthermore, there are some features available in DARE that were not carried over in previous versions of SWAN; these have been reintroduced in the current version in order to provide more control over the χ^2 fitting routine. These additional capabilities will be detailed in the following sections.

A.1.2 New SWAN functions

"cm" (change monochromator b-factor) and "cs" (change sample b-factor):

As described in Appendix B of the thesis dissertation of Dr. Yonglin Qian, the sample rocking curve may be wider than expected because of thermal strains, crystalline defects, or mechanical vibrations affecting the monochromator. It is possible to account for these imperfections when analyzing rocking curve data by assuming the monochromator has a larger effective b-factor than one would expect for a given optical setup. By adjusting the monochromator b-factor, it is possible to obtain the best-fit for a particular rocking curve than if the monochromator b-factor was fixed at the expected value. In earlier versions of SWAN and DARE, however, adjusting the monochromator asymmetry was somewhat tedious, since the reflectivity fit would have to be repeated anew. Therefore, the "change monochromator" ("cm") and "change sample" ("cs") commands were introduced.

After a rocking curve fit is completed (using the "r0" command), the monochromator b-factor can be changed without reentering the sample and monochromator parameters. Entering the "cm" command will prompt the user to choose a new monochromator b-factor. Once the new b-factor is given, SWAN will calculate the relevant structure factors and reflectivity for the revised b-factor, print out the relevant monochromator parameters, and prompt the user if the χ^2 fit should proceed with the new b-factor. The user can then continue with the new rocking curve

fit and review the results. A similar command ("cs") can be used to change the sample b-factor if the user wishes to examine the effect of changes in the sample asymmetry on the eventual rocking curve fit. In either case, these two commands allow reflectivity data to be repeatedly analyzed without re-reading the data files or re-entering the experimental parameters, saving time and keystrokes.

"fp" (fumili parameters) and "rf" (run fumili):

Fitting experimental rocking curve data typically requires only that the user input the sample and monochromator parameters, as well as certain parameters unique to the experiment (incident x-ray energy, angular or energy range of the rocking curve scan, etc.). However, the user may wish to also control the parameters of the χ^2 fitting routine if the results of the fit are not satisfactory. For example, there are instances in which the fit may weigh the "tails" of the rocking curve (i.e. the regions of the rocking curve further from the Bragg condition) at the expense of the central region where the reflectivity is higher. This is generally not a desirable situation, but it can be overcome by manually adjusting the χ^2 fit parameters, such as specifying the initial guesses for the fitting parameters or by fixing the fit parameters to a particular value. This can be done using the "fp" or "fumili parameters" command. This option allows the user to have direct control of the fitting parameters used by the general χ^2 routine (which is contained in the Fortran subroutine fumili.f).

The “fp” and “rf” commands can be used after a rocking curve or fluorescence yield curve has been initially fit in order to repeat the fit with a new set of fit parameters. The command “fh” (fumili help) can be used to display the fit parameters for a given fit. The following on-line help will then be displayed:

```
Fumili Parameters:
 for r0 rocking-curve fit:

1: Angular Scale gain
2: Angular Scale offset
3: Reflectivity Scale gain
4: Reflectivity Scale offset

 for f1 fluorescence fit:

1: Off-Bragg Counts (gain)
2: Offset Counts
3: Coherent Fraction
4: Coherent Position
```

As the help screen shows, the “fp” command may be more useful for refining reflectivity fits rather than fluorescence yield fits, since two of the four florescence yield fit parameters can be modified without using the “fp” command. After typing “fp”, SWAN will then prompt the user on how the fitting parameters should be changed. The syntax for this command is to enter three numbers separated by commas; the first number will be the label of the fit parameter that will be modified, the second number will be the initial guess for the chosen parameter, and the last number will be the step size to be used in the fitting of the selected parameter. (For example, to fix the

reflectivity scale gain at a value of 1.3, the syntax would be `4,1.3,0.0`.) Multiple fit parameters can be modified in this way, and once all the desired changes have been entered, the user should enter `0,0,0`. The "rf" command can then be used to start the χ^2 fit routine once the user confirms the SWAN parameters set using the "rp" command are satisfactory, and the results of the fit with the revised fit parameters can then be reviewed.

A.1.3 Modifying, compiling, and distributing SWAN

The process of implementing changes to SWAN is similar to the development process for much of the Fortran software used in the Bedzyk group. Because most of our data analysis software is written in the Fortran language, developing a usable application that can be used on the current Macintosh platform requires either a native Fortran compiler or a way to convert Fortran source code into C source code. A C or C++ development tool can then handle the translated C source code. In our case, we have chosen the second approach, because it allows us to use some plotting routines that have been developed in C++, as well as use the popular development environment known as CodeWarrior for Mac OS. By using CodeWarrior, we can include convenient features in our applications such as standard Macintosh dialog boxes and alerts. CodeWarrior is used in concert with MacF2C (*http://alumnus.caltech.edu/~igormt/Mac_F2C.html*), which is a freely available

Fortran-to-C translator that runs under Mac OS 9 (or the Classic environment in Mac OS X). In our finding, the most stable combination of CodeWarrior and Mac F2C is CodeWarrior Pro release 5 and Mac F2C v1.4.2 (as of August 2004). While there are more recent versions of these programs available, using the older versions tends to result in fewer translation and compilation errors when developing new applications

The first step in producing an updated version of SWAN (or any other Fortran-derived application) is to modify the source code. This is usually much easier using the original Fortran source rather than the translated C code generated by Mac F2C. Once the initial changes to the source Fortran code have been made, the next step is to use the "Translate…" command in Mac F2C to convert the newly changed Fortran file into a new C source file. During the translation process, F2C presents a status window that shows the current Fortran routine being translated and informs the user if there are any errors in the Fortran code that affect the translation.

If the translation is successful, at least one new file is created. One source file that will always be created will be the translated C source code, which will have the name *filename.C* (assuming the source Fortran code is named *filename.f*). Another file that will also be produced is *filename.P*, which is a prototype file that describes the calling sequence of a function. In order to use the results of the f2c translation with the CodeWarrior compiler, a CodeWarrior project file (i.e. *swan.prj* or *swan.μ*) keeps track

of all the translated files, F2C libraries, and CodeWarrior libraries that are needed to successfully compile a working program.

A.2 Global Analysis of XSW Data using IGOR PRO

For a given atomic distribution for which the ordered adatoms occupy only a single position and the geometrical factor a_H is unity, the adsorbate location with respect to the underlying lattice can be determined by combining the results of normal and off-normal XSW measurements to triangulate the position of the ordered site. However, in atomic configurations in which there may be multiple adsorption sites, determining the atomic distribution can be more complex. For example, in the case of the 1/3 ML Sn/Si(111) surface described in Chapter 6, the various XSW measurements did not triangulate to a single adsorption height above the Si(111) surface. Therefore, a reasonable surface model was developed to account for the possibility of multiple site adsorption. In order to determine the best-fit structural parameters and refine our model, a systematic method was needed to fit this model to all of the {*hhh*} XSW results. Because each set of XSW parameters (i.e. coherent fraction and coherent position) is an independent measurement of the atomic-scale structure, it would be desirable if we could fit all the XSW measurements simultaneously in order to realize the benefit of a larger number of data points. To achieve this global analysis, we used

IGOR PRO, a popular graphing and data analysis software package, and the additional functionality provided by the "Global Fit" procedure file.

As described in the IGOR PRO documentation, the Global Fit procedure provides all the necessary functions to combine the individual data sets into a single data set in order to fit the multiple experiments as a single one. Of course, it is also able to connect the appropriate fitting parameters with the correct data points. More importantly, it allows the fitting parameters to be defined as either global or local parameters. Global parameters are those that will be fit with the same value for all the data sets, while local parameters can have unique values for each individual data set. In our particular case, it is assumed that each {hhh} XSW measurement is probing the same Sn/Si(111) surface (i.e. the surface structure is not changing significantly over the course of several XSW measurements). Therefore, the structural parameters contained in our surface model will be designated as global parameters. However, a local parameter will be used to account for each set of XSW data, which are separate Fourier components of the Sn atomic distribution.

Of course, much of this functionality would be of limited use if IGOR PRO were limited to fitting only the built-in mathematical functions to experimental data. Fortunately, IGOR PRO allows users to define their own functions, enabling us to encapsulate our surface model (as described in Equation 6.1) into a form that IGOR PRO and the Global Fit procedures can handle. In Equation 6.1 there are four fit

parameters to describe the Sn atomic distribution. In the IGOR PRO fitting function "xswParaFit", there can be as many as seven global fit parameters, since it is possible to allow the Sn occupation ratio at different adsorption heights to vary. Furthermore, because each XSW dataset has two independent results (the coherent fraction and coherent position), we can use a linear fit to analyze the XSW results. In our case, the slopes and intercepts of the individual lines that are fit to the XSW data are calculated as a linear combination of the two XSW parameters.

Now that the underlying fit function has been defined, the experimental XSW data and the appropriate initial guesses for the fit parameters have to be loaded into IGOR PRO. Depending on the nature of the fit, some fit parameters may be constrained to ensure they remain within set limits or held constant during the fit. Fortunately, the Global Fit procedure provides a simple graphical user interface to perform all these functions. The Global Analysis control panel, depicted in Figure A.1, allows the user to choose the function that will be fit, choose the number of fit parameters and define them as either global or local parameters, select the data sets to be analyzed, and enter the initial guesses for the various global and local parameters. There is also the option to apply constraints to the fit parameters or weight the experimental data by the error in the XSW measurements.

When using the Global Analysis control panel, the first step is to select the

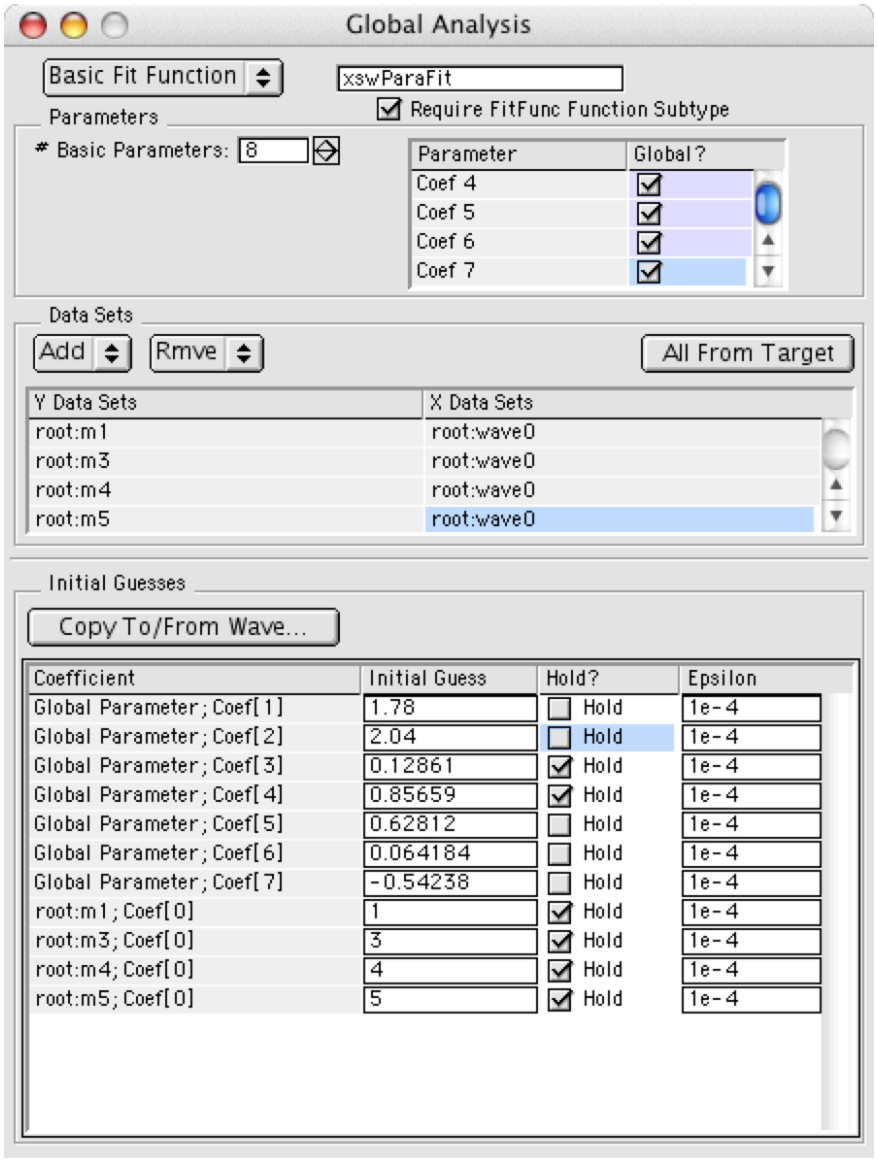

Figure A.1: The Global Analysis control panel of the Global Fit IGOR PRO procedure. The fitting function, data sets, and initial parameters are specified in this panel.

appropriate fit function. A pull-down menu displays the available fitting functions, which include both the built-in functions and any user-defined functions. The parameter information can be then set in the "Parameters" section of the Global Analysis control panel. In the case of our surface model, there are a possible total of eight fit parameters. Seven of these eight parameters represent the structural details of the Sn distribution (such as adatom height, Sn occupation, fraction of Sn substituting for Si atoms, etc.) and are therefore treated as global parameters. The other parameter (defined as `w[0]` in the xswParaFit function) does not directly relate to the Sn/Si surface structure, but rather is used to track which {hhh} Fourier component is involved in the global fit. Therefore, this parameter is designated as a local one and will be fixed at an integer value (m = 1, 3, 4, and 5) during the fit process.

The Data Sets portion of the control panel allow any number of data sets to be entered for global analysis. The data sets can be either entered via the "Add" pull-down menu in the Data Sets section or from an existing graph of the data to be analyzed. When using the pull-down menu, the user should specify both the Y Data Set and the X Data Set, if the appropriate X data exists. If there is no specific X data that corresponds with the Y Data to be fit, the "_Calculated_" Data Set should be selected as the matching X Data Set. The data sets to be analyzed can also be loaded from an open graph using the "All from Target" button. In our case, the individual XSW results are defined as a series of Igor Pro waves, which are tabulated in Figure A.2. There are a

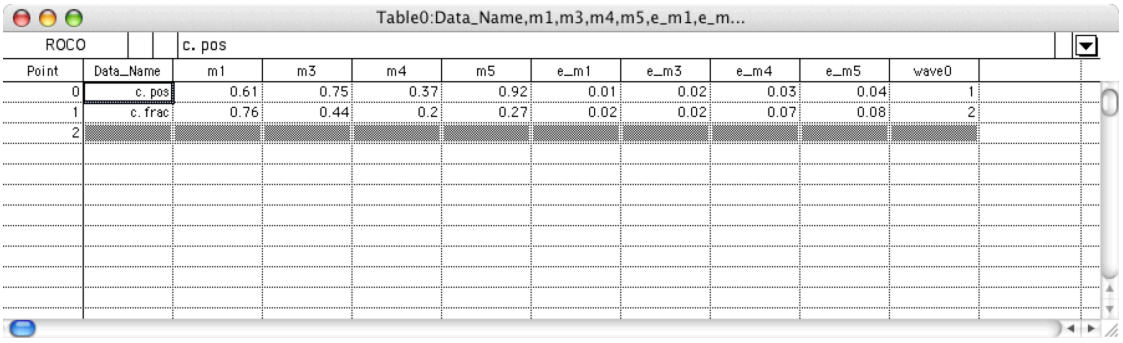

Point	Data_Name	m1	m3	m4	m5	e_m1	e_m3	e_m4	e_m5	wave0
0	c. pos	0.61	0.75	0.37	0.92	0.01	0.02	0.03	0.04	1
1	c. frac	0.76	0.44	0.2	0.27	0.02	0.02	0.07	0.08	2
2										

Figure A.2: The table created in IGOR PRO that contains the eight waves used in the Sn/Si(111) global fit. The first four waves contain the coherent fractions and positions for the four sets of (*hhh*) XSW results, while the next four waves contain the uncertainties for the XSW results.

total of eight waves used in the global analysis routine; four of the waves contain the XSW results for the four {hhh} reflections used in the Sn/Si experiment, while the other four contain the standard error for the sets of coherent fractions and coherent positions. The XSW results are also shown in Figure A.3, which shows the coherent position on the left-hand side of the plot and the coherent fraction on the right-hand side. The abscissa of the plot is an arbitrary scale that is used so that the XSW data can be graphically displayed and fit to the "xswParaFit" equation. (The individual XSW data sets are offset for clarity.) This plot can be used as the target when loading the XSW data into the Global Analysis procedure.

The final step in preparing the fit is entering the initial guesses for the various fit parameters. This is done using the "Initial Guesses" section of the Global Analysis control panel. This subpanel contains a list of all the parameters defined in the fitting function and allows the user to specify an initial guess for the χ^2 fit, whether the parameter should be held constant during the analysis, and specify a custom epsilon value for each fit coefficient. (Epsilon values are used to calculate partial derivatives with respect to the fit parameters, which in turn are used to determine the direction in which the χ^2 fitting routine proceeds.) In the case of our Sn/Si surface model, the Global Analysis control panel appears as shown in Figure A.1 after specifying the "xswParaFit" fit function and loading the four XSW data sets. The figure shows that seven of the eight parameters are global parameters, and therefore accept only one

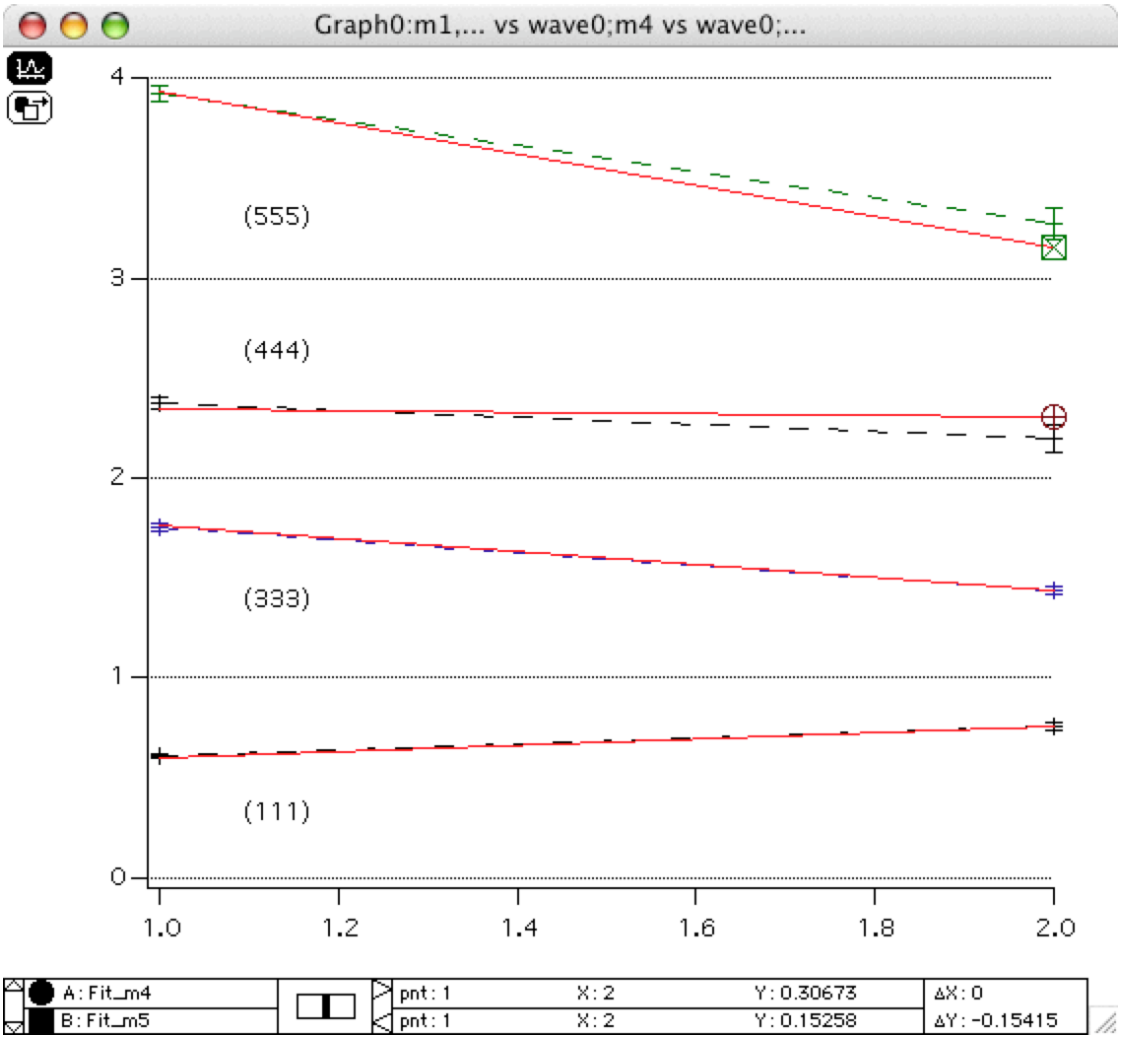

Figure A.3: Graph generated by IGOR PRO that represents the global fit of the specified structural model to the XSW data. The dashed line connects the experimentally-determined values for the coherent fraction and coherent position, and the uncertainty in these values are shown as error bars. The solid red line connects the best-fit values for the XSW parameters.

value for each global parameter. One of the fit coefficients is a local parameter, however, and therefore requires four values for each of the four XSW data sets specified. As mentioned previously, the four parameters keep track of the different {hhh} XSW-determined Fourier components and are held at their value during the fit process.

Some optional fit attributes can be set at the bottom of the control panel. The most useful of these options are the "Apply Constraints" and the "Weighting…" parameters. These allow for the fine-tuning of the χ^2 fit routine by letting the user force some or all of the fit coefficients to remain within set limits, or select a separate set of error waves that will be used to weight the XSW data sets. In order to produce a meaningful goodness-of-fit parameter, the error for the XSW results are saved as separate waves and used as the weighting waves ("e_m#", where "#" refers to the data set to which the error applies). The correct error waves must be selected and matched with the appropriate XSW data set in the "Weighting…" dialog.

Once all these initial parameters and options are selected, the fit process can begin using the "Fit!" button on the Global Analysis panel. After the fitting routine is finished, information about the fit results is displayed in the command window, such as the best-fit values of the fit coefficients, the χ^2 value of the completed fit, and the calculated standard deviation of the fit parameters. The fit results can also be displayed graphically to allow for a visual comparison between the experimental data and the

best-fit parameters, as shown in Figure A.3. Of course, once the fit is completed, any of the initial fit options and parameters can be modified and the fit repeated.

A.2.1 IGOR PRO function for XSW global fit

The custom fitting function used with the IGOR PRO Global Fit procedure to fit the multiple sets of XSW data is listed below.

```
Function xswParaFit(w,xx) : FitFunc

Wave w
Variable xx
Variable real_ah, imag_ah, coh_f, coh_p, occT, occS, DWF
Variable /C Fm_rect, Fm_pol

        //CurveFitDialog/ These comments were created by
        the Curve Fitting dialog. Altering them will
        //CurveFitDialog/ make the function less
        convenient to work with in the Curve Fitting
        dialog.
        //CurveFitDialog/ Equation:
        //CurveFitDialog/ f(xx) = a+b*xx
        //CurveFitDialog/ End of Equation
        //CurveFitDialog/ Independent Variables 1
        //CurveFitDialog/ xx
        //CurveFitDialog/ Coefficients 8
        //CurveFitDialog/ w[0] = m
        //CurveFitDialog/ w[1] = H_a  (1/3)
        //CurveFitDialog/ w[2] = H_b  (2/3)
        //CurveFitDialog/ w[3] = DWF
        //CurveFitDialog/ w[4] = C
        //CurveFitDialog/ w[5] = occT ( at T4 site)
                                //CurveFitDialog/ w[5] =
        occS (not at t4 site)
        //CurveFitDialog/ w[6] = h_subF
        //CurveFitDialog/
```

```
        occS = w[6]
        occT = w[5]

real_ah = occT*cos(2*Pi*w[0]*w[1]/kd_111)+(1-occT-
        occS)*cos(2*Pi*w[0]*w[2]/kd_111)
real_ah += occS*cos(2*Pi*w[0]*w[7]/kd_111)
imag_ah = occT*sin(2*Pi*w[0]*w[1]/kd_111)+(1-occT-
        occS)*sin(2*Pi*w[0]*w[2]/kd_111)
        imag_ah += occS*sin(2*Pi*w[0]*w[7]/kd_111)
        DWF = exp(-2*(Pi*w[3]/(kd_111/w[0]))^2)
        Fm_rect = DWF*w[4]*cmplx(real_ah, imag_ah)
        Fm_pol = r2polar(Fm_rect)
        coh_f = real(Fm_pol)
        coh_p = imag(Fm_pol)/(2*pi)
        if  (coh_p < 0.0)
            coh_p +=1
        endif
        return (2*coh_p-coh_f)+(coh_f-coh_p)*xx
        End
```

A.3 Atomic Coordinates for the Bulk α-Fe_2O_3 Crystal Structure

The fe2o3.ctl file used in conjunction with SWAN in order to analyze the XSW data for the 1/2 ML V/α-Fe_2O_3(0001) surfaces is listed on the following page.

```
Fe2O3
   5.038   5.038   13.772   90.00   90.00   120.00
   300.
   0.0     0.0     0.0
   2    1    1
Atoms in basis # 1
  fe    26  1.00
   12
   0.333 0.667 0.022
   0.000 0.000 0.145
   0.667 0.333 0.189
   0.333 0.667 0.311
   0.000 0.000 0.355
   0.667 0.333 0.478
   0.333 0.667 0.522
   0.000 0.000 0.645
   0.667 0.333 0.689
   0.333 0.667 0.811
   0.000 0.000 0.855
   0.667 0.333 0.978
Atoms in basis # 2
  o     08  1.00
   18
   0.667 0.027 0.083
   0.361 0.333 0.083
   0.973 0.637 0.083
   0.000 0.306 0.250
   0.306 0.000 0.250
   0.694 0.694 0.250
   0.333 0.361 0.417
   0.027 0.667 0.417
   0.639 0.973 0.417
   0.361 0.027 0.583
   0.973 0.333 0.585
   0.667 0.639 0.583
   0.694 0.000 0.750
   0.306 0.306 0.750
   0.000 0.694 0.750
   0.027 0.361 0.917
   0.639 0.667 0.917
   0.333 0.973 0.917
```

A.4 Calculated XSW Data for the Fe Atomic Density Map

The following table contains the calculated Fourier amplitude and phase that was used to generate the Fe atomic density map shown in Figure 4.4. This simulated XSW data was calculated according to the atomic coordinates shown in the .ctl file contained in Section A.3.

(*hkl*) reflection	(0006)	$(10\bar{1}4)$	$(01\bar{1}2)$	$(11\bar{2}3)$
f_H	0.675	0.880	0.245	0
P_H	0	0.5	0.5	n/a

Table A.1: The calculated values for coherent fraction f_H and coherent position P_H for the bulk Fe atomic distribution in the hematite unit cell. The coordinates for this calculation are contained in the .ctl file shown in Section A.3.